State engineering in one-dimensional quantum gases

Okinawa Institute of Science and Technology
Graduate University

Thesis submitted for the degree

Doctor of Philosophy

State engineering in one-dimensional quantum gases

by

Irina Reshodko

Supervisor: **Thomas Busch**

January, 2019

Declaration of Original and Sole Authorship

I, Irina Reshodko, declare that this thesis entitled *State engineering in one-dimensional quantum gases* and the data presented in it are original and my own work.

I confirm that:

- No part of this work has previously been submitted for a degree at this or any other university.
- References to the work of others have been clearly acknowledged. Quotations from the work of others have been clearly indicated, and attributed to them.
- In cases where others have contributed to part of this work, such contribution has been clearly acknowledged and distinguished from my own work.
- Parts of this work have been published in Physical Review A **96** 023606 (2017) as "Robust boson dispenser: Quantum state preparation in interacting many-particle systems", Few-Body Systems **59** 48 (2018) as "Entanglement in Spatial Adiabatic Processes for Interacting Atoms" and New Journal of Physics (2018) as "Topological states in the Kronig-Penney model with arbitrary scattering potentials".

Date: January, 2019
Signature:

Abstract

State engineering in one-dimensional quantum gases

The development of quantum technologies requires the understanding, controlling and engineering of quantum states of interacting systems, a challenge currently driven by experimental progress. In this work I study, both analytically and numerically, two specific models of one-dimensional ultracold atomic systems to determine their states and accessible dynamical behaviour. The first part of the work deals with the creation of a bosonic atom dispenser, a tool which would allow to deterministically separate any number of atoms from an interacting ultracold gas or create a many-particle NOON state. By engineering an effectively three-level system, I show that a robust adiabatic process exists that connects the initial and target Fock states. Moreover, I demonstrate its potential to be experimentally implemented using radio-frequency traps.

In the second part, I derive an analytical single-particle solution for the arbitrary finite Kronig–Penney model. In this model the atoms are trapped in an infinite square well which contains an arbitrary number of arbitrarily positioned point-like barriers of arbitrary heights. I also demonstrate that using certain parameters in the model as extra (virtual) dimensions one can observe the emergence of higher-dimensional physics in this one-dimensional system. In particular, I show the appearance of edge states and the emergence of a Hofstadter butterfly-like momentum spectrum in various configurations of the model. Finally, using the single-particle solutions, I study many-body correlations in a gas of either infinitely repulsive bosons or non-interacting fermions.

Acknowledgment

I sincerely thank Thomas Busch and Albert Benseny for their guidance, helpful discussions and proofreading of my manuscripts. I also thank the Quantum Systems Unit members for their support and feedback on this thesis. I am very grateful to Judit Romhányi for her help with the calculation of the Chern numbers and valuable discussions.

Figures 2.2-2.5 in chapter 2 are provided by Albert Benseny and are reproduced with permission.

Dedicated to Sudo Sahyens with appreciation for
his support and fruitful discussions.

Contents

Introduction

Zero Kelvin was first defined classically as a temperature when the molecules of an ideal gas stop moving, but understanding of what this limit actually represents came later, with the advent of quantum mechanics in the beginning of 20th century. The limit turned out to be unreachable due to the Heisenberg uncertainty principle. However, the region of the temperature scale near zero Kelvin promised exciting new physics of ultra-cold matter.

In the early 1920s Bose introduced a new way of deriving Planck's law for the energy spectrum of black-body radiation [2], and in 1925 Einstein used his results, which were valid for photons, to study the behaviour of a dilute gas of indistinguishable non-interacting particles near absolute zero [3]. He predicted that after being cooled to a threshold temperature, a gas of non-interacting bosonic particles exhibits quantum mechanical behaviour on a macroscopic scale, defining a new state of matter - the Bose-Einstein Condensate (BEC). However, long before reaching the Bose–Einstein condensation temperature, normal matter would undergo a more conventional transition to a liquid or a solid state. Only in extrememly diluted gases it is posible to avoid such an undesirable transition. Experimental challenges such as cooling of a gas to sufficiently low temperatures and its confinement delayed experimental realisation of Bose-Einstein condensation in gases for 70 years. Advanced cooling techniques, such as Doppler [4], evaporative [5], and sideband cooling [6], and trapping methods, such as magneto-optical [7] and purely optical [8, 9] trapping, had to be developed first, and in 1995 Ketterle, Cornell and Wieman [10, 11] succeeded in producing a BEC in dilute atomic gases. They were awarded with the Nobel Prize in Physics in 2001 for this achievement. New experimental techniques became available later [12, 13], allowing for great flexibility and detailed control in BEC experiments. Ultracold gases became a widespread model to study quantum mechanical effects in clean and controllable situations.

The connection of superfluidity, a phenomenon where a fluid flows without viscosity, and Bose–Einstein condensation of delocalised particle pairs was already suspected in 1938 by London [14] and further developed by Landau and Tisza [15, 16]. The discovery of superfluidity in liquid Helium by Kapitza, Allen and Misener in 1938 [17, 18] can be considered as first evidence for the BEC. Landau's criteria of superfluidity was first confirmed in a BEC by Raman *et al.* in 1999 [19].

Theoretical description of many-body quantum systems, cooled down to ultra-cold regimes, is a big challenge because of the inherent difficulty of solving the many-body Schrödinger equation. In general, a mean-field approach has to be applied in order to simplify the problem, but some models, especially in lower dimensions, can still be stud-

ied exactly. Despite their apparent simplicity, low-dimensional systems offer complex physics usually attributed to higher dimensions, such as non-trivial topological [20, 21] and thermodynamical [22–24] properties.

In this work I treat one-dimensional ultracold atomic models both analytically and numerically to investigate interesting states of one-dimensional system with multiple traps and develop theoretical tools of engineering of such states. The structure of this thesis is as follows.

In chapter 1 I introduce the field of one-dimensional quantum gases, and talk about integrability and integrable systems in section 1.4. In chapter 2, section 2.2 I review one of the quantum state engineering techniques, the spatial adiabatic passage, and in section 2.4 I present a new protocol which allows to separate an arbitrary number of particles from a gas of interacting bosons (the boson dispenser). I also propose a possible experimental realisation of this protocol using radio frequency traps and show its robustness (section 2.5). I investigate the entropy dynamics during the particle separation protocol in section 2.6.

In chapter 3 I introduce the Bethe ansatz technique and examine the example of the Lieb–Liniger model in a box in detail in section 3.2. In sections 3.3 and 3.4, I show the violation of the Yang–Baxter equations in the case of two particles and multiple barriers. I then introduce and solve the arbitrary finite Kronig–Penney model for a single particle in section 3.5.

I discuss topological phenomena in one- and two-dimensional systems in sections 4.1 and 4.2, and apply the obtained solution to investigate the existence of the edge states in the single-particle and Tonks–Girardeau limit of many-body AFKP model and the appearance of the Hofstadter butterfly-like momentum spectrum in section 4.3. Finally, in chapter 5 I review numerical methods which were used in my work and conclude in chapter 6.

Chapter 1

One-dimensional Bose gases

1.1 Introduction

Many-body systems in dimensions lower than three often exhibit drastically different behaviour in comparison to higher dimensions. In one dimension both macroscopic processes, such as phase transitions [25, 26] and thermalisation [22, 27], and microscopic properties, such as interaction between particles, are vastly different from the the 3D and 2D counterparts. Unlike most higher dimensional cases, some one-dimensional models can be solved exactly. Such integrable systems have enjoyed both great attention due to their immense usefullness in understanding basic low-dimensional physics [28] and, in some sense, dismissal due to their simplicity. System which are simple enough to be integrable are perceived as too boring for anything exciting to happen within them since they cannot even thermalize [29, 30], and there is seemingly no room for anything topologically non-trivial. However, a closer look reveals that integrable systems can still exhibit non-trivial thermodynamical [22–24, 27, 31] and topological behaviour [20, 21, 32, 33]. For example, it was shown that integrable 1D systems exhibit a special type of thermalisation behaviour called prethermalisation which can be described by a generalised Gibbs ensemble, but they cannot achieve normal equilibrium [24].

The models of many-body systems in one dimension may seem to be of purely theoretical interest, but they became very attractive from an experimental point of view after a theoretical study conducted by M. Olshanii in 1998, which showed that one-dimensional interaction strengths can be manipulated by changing the external potential shape. In this study Olshanii derived a mathematical expression for the effective scattering length of transversally confined atoms which are free to move along one axis [34], given by

$$a_{1\mathrm{D}} = -\frac{a_\perp^2}{2a}\left(1 - C\frac{a}{a_\perp}\right). \tag{1.1}$$

Here a is the original 3D s-wave scattering length, $a_\perp = \sqrt{\frac{2\hbar^2}{m\omega_\perp}}$ is the ground state size of the harmonic oscillator potential in the transverse direction, $\omega_\perp$ is the frequency of the harmonic transverse trapping potential, m is the particle mass and $C = 1.4603...$ is a constant.

One can immediately see the dependence of the 1D scattering length on $a_\perp$, which

in turn inversely depends on $\sqrt{\omega_\perp}$. The inverse dependence of a_{1D} on a is even more surprising, leading to weaker 1D interactions for stronger 3D interactions. The result in 1.1 is very important because it allows flexible tuning of the interaction strength $g_{1D} = -\frac{2\hbar^2}{ma_{1D}}$ in 1D systems by tuning the transverse confinement $\omega_\perp$.

The interaction strength g_{1D} increases with decreasing effective 1D scattering length, which in turn decreases when the transverse confinement frequency is increased, so it is possible to approach the Tonks–Girardeau limit $g \to \infty$ by squeezing the transverse confinement. Direct observations of a Bose gas in the TG limit was done by Paredes *et al.* in 2004 [35] and Kinoshita *et al.* in 2005 [36]. Experimental studies of one dimensional systems have been very active for about fifteen years now, realising both non-trivial external potential shapes [37–39] and various interaction regimes [40–45].

There are several models which can describe ultra-cold Bose gases in one dimension. In this section I will review some of them.

1.2 One-dimensional gases in a continuum space

Let us consider a Bose gas in a potential $V_{\text{ext}}(\vec{r})$ with very strong confinement in the Y and Z directions. This confinement leads to an energy spectrum, where excitation energies in Y and Z directions are larger than the chemical potential. Thus we can approximate the YZ ground state by a stationary solution and focus on the wave-function dynamics in the X direction $\psi(x_1, ..., x_N)$.

The most general many-body one-dimensional Hamiltonian with identical particles interacting through $V_{\text{int}}(x_i - x_j)$ is

$$\hat{H} = \sum_{i=1}^{N} \left[-\frac{\hbar^2}{2m} \frac{\partial^2}{\partial x_i^2} + V_{\text{ext}}(\hat{x}_i) \right] + \sum_{i<j=1}^{N} V_{\text{int}}(\hat{x}_i - \hat{x}_j). \tag{1.2}$$

This Hamiltonian can in general not be solved exactly, so various approximations have to be used.

An approximation assuming the absence of the external potential $V_{\text{ext}} = 0$ and the presence of the contact interaction $V_{\text{int}}(x) = g\delta(x)$ (the **Lieb–Liniger model**) was introduced and solved by Lieb and Liniger in 1963 [46]. If $g = 0$, it becomes a system of non-interacting bosons, while for $g \to \infty$, it becomes a hard-core or Tonks–Girardeau gas. This model will be discussed in great detail in chapter 3 as a case study of the Bethe ansatz method.

The **Calogero model** [47] assumes the external potential to be harmonic, $V_{\text{ext}}(x) = \frac{1}{2}m\omega^2 x^2$, or absent, $V_{\text{ext}} = 0$, and the interaction potential to be of the form of $V_{\text{int}}(x_i, x_j) = \frac{g}{(x_i - x_j)^2}$. The Hamiltonian of the Calogero model is

$$\hat{H} = \sum_{i=1}^{N} \left(-\frac{\hbar^2}{2m} \frac{\partial^2}{\partial {x_i}^2} + V_{\text{ext}}(x_i) \right) + \sum_{i<j=1}^{N} \frac{g}{(x_i - x_j)^2}. \tag{1.3}$$

The interaction term, $\sum_{i<j=1}^{N} \frac{g}{(x_i - x_j)^2}$, has a singularity at $x_i = x_j$. At $g = 0$ it represents a gas with no interaction between the particles, unless $x_i = x_j$. This implies

that the interaction potential in this case is $\delta(x_i - x_j)$ with infinite interaction strength (Tonks–Girardeau limit).

Besides inverse squared and point-like interactions there are other types of interaction potentials which have relevant physical applications. For example, an interaction term of the form $V_{\text{int}}(x) = \frac{1}{|x|^3}$ approximates a system of polarized dipoles in one dimension, such as dipolar bosonic molecules [48]. The integral of the inverse cubic potential converges in 1D, thus resulting in essentially short-range physics.

Another example is the unscreened Coulomb potential $V_{\text{int}}(x) = \frac{1}{|x|}$, which describes systems with charged particles, such as in ion traps [49].

Various shapes of the external potential, such as shallow periodic [50] or disordered [51, 52] potentials, are also important models in solid-state physics. One special case is the Tonks–Girardeau limit of interactions, which can be solved analytically in many trap geometries by using the Bose–Fermi mapping [53].

1.3 One-dimensional gases in lattice models

In addition to continuum models, there are models which describe bosons in a discrete periodic limit.

Let us consider a deep periodic external potential, for example $V_{\text{ext}}(x) = V_0 \cos(\frac{2\pi x}{a})$. For low energies this configuration can be regarded as a discrete lattice with a lattice parameter a and amplitude V_0.

Creation and annihilation of a particle in such an environment can be simplified to creation and annihilation of a particle at the lattice sites. The corresponding creation and annihilation operators are denoted as $\hat{b}_j^\dagger$ and $\hat{b}_j$.

If there are n_j particles at the site j and $|n_j\rangle$ is the corresponding state, then $\hat{b}_j|n_j\rangle = \sqrt{n_j}|n_j - 1\rangle$ and $\hat{b}_j^\dagger|n_j\rangle = \sqrt{n_j + 1}|n_j + 1\rangle$.
The eigenstate wave function of a particle in one isolated node is called a Wannier orbital, while the eigenstates of one particle delocalised over the whole lattice (all nodes are included in the calculations) are called Bloch orbitals for this external potential. In other words, Bloch orbitals are the exact delocalised representation of the particles in a lattice, and Wannier orbitals are the approximated localised representation. The Wannier approximation becomes more accurate with increasing lattice depth, and in this so-called tight-binding regime we can write the creation and annihilation operators in the basis of Wannier orbitals $w_0(x)$ which belong to the lowest Bloch band (ground state) for $V_{\text{ext}} = V_0 \cos(\frac{2\pi x}{a})$. The Hamiltonian of the system can then be written as [47]

$$\hat{H} = \sum_{j,k=1}^{L} \left[-t_{jk} \hat{b}_j^\dagger \hat{b}_k + \sum_{l,m=1}^{L} V_{jl,km}^{int} \hat{b}_j^\dagger \hat{b}_l^\dagger \hat{b}_k \hat{b}_m \right]. \tag{1.4}$$

Here

$$t_{jk} = -\int w_0^*(x - ja) \hat{H}_0(x) w_0(x - ka) dx \tag{1.5}$$

is the kinetic energy term which corresponds to the particle tunnelling, and

$$V_{jl,km}^{\text{int}} = \int w_0^*(x - ja) w_0^*(x' - la) V_{\text{int}}(x - x') w_0(x' - ka) w_0(x - ma) \tag{1.6}$$

is the potential energy term which corresponds to the scattering of two interacting particles, and $\hat{H}_0 = -\frac{\hbar^2}{2m}\partial_x^2 + V_{\text{ext}}(x)$.
This Hamiltonian can also not be solved exactly unless an approximation is applied. There are many theoretical models for different regimes, and in the following I will discuss some of them.

The **Bose–Hubbard model** approximates the Hamiltonian (1.4) by assuming that the interaction range is small compared to the lattice parameter, so we can neglect nearest-neighbour interaction terms [54] while including the on-site interaction term with strength U

$$\hat{H}_{\text{BH}} = \sum_{i=1}^{L} \left[-t(\hat{b}_i^\dagger \hat{b}_{i+1} + \hat{b}_{i+1}^\dagger \hat{b}_i) + \frac{U}{2} \hat{b}_i^\dagger \hat{b}_i^\dagger \hat{b}_i \hat{b}_i \right] \tag{1.7}$$

The Bose–Hubbard model is not exactly solvable for finite values of $\frac{U}{t}$, but in the limit $\frac{U}{t} \to \infty$ it becomes a lattice analogue of the Tonks–Girardeau gas.

One of the most remarkable predictions of the Bose–Hubbard model is the existence of a phase transition from a superfluid (where particles can move freely across the lattice) to an insulating state (where particles are essentially pinned to one lattice site), known as the Mott insulator phase [55, 56]. With the number of particles kept constant, the ratio U/t between the on-site interaction and the nearest-neighbour tunneling strength controls the transition, with the Mott insulator phase taking over at $U/t \gtrsim 1$. This phase transition was observed experimentally in [57–59].

The **Extended Bose-Hubbard model** also describes a deep lattice, with the particles localised around one node. In contrast to the Bose–Hubbard model, it includes diagonal and nearest-neighbour terms [47], and the Hamiltonian becomes

$$\hat{H}_{\text{EBH}} = \sum_{i=1}^{L} \left[-t(\hat{b}_i^\dagger \hat{b}_{i+1} + \hat{b}_{i+1}^\dagger \hat{b}_i) + \frac{U}{2} \hat{b}_i^\dagger \hat{b}_i^\dagger \hat{b}_i \hat{b}_i \right] + \sum_{i=1}^{L} V \hat{n}_i \hat{n}_{i+1}, \tag{1.8}$$

where $\hat{n}_i = \hat{b}_i^\dagger \hat{b}_i$ is the site occupation operator and V is the nearest-neighbour interaction strength. This model approximates particles with long-range interaction trapped in a deep lattice, such as dipoles or Rydberg atoms [60]. The EBH model predicts the existence of yet another phase where superfluidity coexists with the long-range crystalline order more characterstic to solids [61–63]. This novel phase is called the supersolid phase, and recently its existence was supported experimentally [64, 65].

The **t-V model**, also called the quantum lattice gas model [66], can be used if the interactions are long-range (e.g. dipolar ultra-cold atoms) and the on-site interaction strength U is very large (so one can assume it to be infinitely large). In this case a state with two particles in one site will be energetically unfavourable, and therefore the on-site interaction term can be neglected. However, the nearest-neighbour interaction term, $V\hat{n}_i\hat{n}_{i+1}$, cannot be neglected and the Hamiltonian becomes

$$\hat{H}_{t-V} = \sum_{i=1}^{L} \left[-t(\hat{b}_i^\dagger \hat{b}_{i+1} + \hat{b}_{i+1}^\dagger \hat{b}_i) + V \hat{n}_i \hat{n}_{i+1} \right]. \tag{1.9}$$

This model is equivalent to an anisotropic spin-$\frac{1}{2}$ model [66] and can be solved using the Bethe ansatz.

1.4 Integrable systems

Some of the models of quantum systems can be solved exactly, but a priori there is no easy way to determine if a system is integrable. The notion of complete integrability is different for classical and quantum physics. There is a clear definition of complete integrability for classical systems, while for quantum systems there is no useful necessary and sufficient condition of integrability [28, 67].

In what follows I will briefly discuss the notion of complete integrability in classical physics and compare it to the quantum physics case, while discussing the latter in more detail.

Let us consider a classical system described by the Hamiltonian H and the constants of motion $\vec{L} = (L_1, ..., L_K)$. The necessary and sufficient condition of integrability of such a system is

$$\begin{cases} \{L_i, H\} = 0 \\ \{L_i, L_j\} = 0 \end{cases} \quad i, j = 1...K, \tag{1.10}$$

where $\{A, B\}$ denotes the Poisson brackets [28].

The analogous definition of integrability for quantum systems, derived from the classical one by substituting the Poisson brackets with commutators, although technically valid, does not hint on how to actually obtain the solution [28, 68], so it makes more sense to talk about more constructive conditions of quantum integrability.

To simplify the description, let us restrict ourselves to one-dimensional quantum systems of N identical particles, which interact with the repulsive potential $V(r)$. We assume this interaction potential to be short-ranged (the interaction between the particles vanishes sufficiently quickly with the distance between the particles) and symmetrical. An examples of such a potential is the point interaction potential $\delta(r)$. Also, we assume the total number of the particles N, ordered such that $x_1 < x_2 < ... < x_N$ and the energy E and total asymptotic momentum P to be conserved. The wave function for all other orderings of the particles are given by the quantum statistics (Bose or Fermi). The Hamiltonian of the system is

$$\hat{H} = -\frac{\hbar^2}{2m} \sum_{j=1}^{N} \frac{\partial^2}{\partial x_j^2} + \sum_{1=j<k}^{N} V(x_k - x_j). \tag{1.11}$$

There are $N - 1$ kinds of scattering processes possible in this system: two-body scattering, three-body scattering and so on. For short-range interaction potentials in 1D the conservation of total asymptotic momentum implies that two-body scattering can only swap the momenta of the scattering particles and add a phase to the wave function. If $N = 2$, where no three-body scattering is possible, the asymptotic wave function is thus

$$\Psi(x_1, x_2) \to e^{i(k_1 x_1 + k_1 x_2)} - e^{-i\theta(k_1 - k_2) + i(k_2 x_1 + k_1 x_2)}. \tag{1.12}$$

For $N > 2$ the asymptotic wave function has to incorporate all other higher order scattering events and therefore takes the form

$$\Psi(x) \to \sum_{\varpi} A(\varpi) e^{i(k_{\varpi_1} x_1 + ... + k_{\varpi_N} x_N)} + S[P, E] \tag{1.13}$$

Here $A(\varpi)$ are the scattering amplitudes, ϖ is a permutation of the quasi-momenta k_j and $S[P,E]$ is the higher order scattering term with total momentum P and energy E fixed. The scattering amplitudes corresponding to two permutations, which differ from each other by two exchanged indices, are related by the two-body phase shift, $\frac{A_\varpi}{A_{\varpi'}} = e^{i\theta(k-k')}$.
The sum constitutes the **Bethe ansatz wave function**, and the higher order scattering term $S[P,E]$ can be treated as a diffraction term. Models where the diffraction term is absent are called nondiffractive and can be solved by the asymptotic Bethe ansatz. In the case of contact interactions the asymptotic region is everywhere except for the point where the particles coincide, and therefore such a solution becomes exact. This is the original version of the Bethe ansatz, and I will discuss it in Chapter 3. This fact implies that the models, where all scattering events can be viewed as a sequence of two-body scattering, can be solved exactly in the asymptotic region. This does not imply, however, that only nondiffractive models can be solved this way, but the property of nondiffraction is clear and easy to define and can be used as a test of integrability for quantum systems. The advantage of this approach lies also in the fact that it is constructive, providing a clue of how to solve the problem rather than just stating the existence of an analytical solution.

The Lieb–Liniger model [46] describes a system of N free bosons with contact interaction, and has the Hamiltonian

$$\hat{H} = -\frac{\hbar^2}{2m}\sum_{i=1}^{N}\frac{\partial^2}{\partial x_i^2} + g\sum_{i<j=1}^{N}\delta(x_i - x_j), \tag{1.14}$$

where $\delta(x)$ is the Dirac delta function, and g is the interaction strength. In the 2-particles case the Hamiltonian can be explicitly written as

$$\hat{H} = -\frac{\hbar^2}{2m}\frac{\partial^2}{\partial x_1^2} - \frac{\hbar^2}{2m}\frac{\partial^2}{\partial x_2^2} + g\delta(x_1 - x_2). \tag{1.15}$$

If $g < 0$ (attractive interaction), then bound states will be created in free space (molecules will be formed), and the solution will look more complicated. I will therefore consider only repulsive interaction ($g > 0$).

One interesting limit of the Lieb–Liniger model is one-dimensional Bose gas in **Tonks–Girardeau** gas with infinitely strong interactions, $g \to \infty$. This model is exactly solvable by mapping it to a system of spinless fermions [53], which reveals the equivalence of the density function of strongly interacting bosons and non-interacting spinless fermions [69]. Due to strong repulsion the wave function must vanish where the coordinates of the particles coincide ($x_i = x_j$), which imitates the Pauli exclusion principle. The total fermionic wavefuction can then be constructed from the single-particle wave-functions as the Slater determinant. If we define the sign function as usual and define the function $S(x_1, x_2, ..., x_N) = \prod_{i<j=1}^{N} \mathrm{sign}(x_i - x_j)$, we can rewrite the bosonic wave function from the fermionic one as [70]

$$\Psi_B(x_1, x_2, ..., x_N) = S(x_1, x_2, ..., x_N)\Psi_F(x_1, x_2, ..., x_N). \tag{1.16}$$

Here $\Psi_F(x_1, x_2, ..., x_N)$ is a many-body wave function of an ideal gas of spinless fermions, and Ψ_B obeys Bose statistics

$$\Psi_B(..., x_i, ..., x_j, ...) = \Psi_B(..., x_j, ..., x_i, ...). \tag{1.17}$$

In the absence of an external potential ($V(x) = 0$) on a ring of circumference L with periodic boundary conditions the ground state is [53]

$$\Psi_B^0(x_1, x_2, ..., x_N) \propto \prod_{i<j} \sin \frac{\pi}{L} |x_i - x_j|. \tag{1.18}$$

The corresponding energy is $E_0 = \frac{\hbar^2(\pi\rho_0)^2}{6\pi m}$, where $\rho_0 = \frac{N}{L}$ is a mean particle density.

The behaviour of the Tonks–Girardeau gas in various potentials, such as harmonic [71] and double-well potentials [72] has been studied as well.

The Bose–Fermi mapping approach was generalised for excited states and for any value of interaction strength of the Lieb–Liniger model [73], as well as for time evolution studies. Using the exact solution, in 2005 Minguzzi and Gangardt investigated the time evolution of the harmonically trapped TG-gas with arbitrary time dependence of the trapping frequency. In the case of the confinement being switched off, they observed fermionisation of the momentum distribution, while in the case of a change of the trapping frequency the momentum distribution exhibited oscillations between fermion-like and boson-like structure [74]. The dynamical properties of the TG-gas have attracted a lot of attention since then [75–77].

In 2002 Das, Girardeau and Wright proved that the TG regime can be achieved for finite temperatures, allowing for experimental realisation [78]. The groups of Bloch and Weiss were the first to achieve the Tonks–Girardeau limit for rubidium atoms in an 2D optical lattice [35] and in a 1D horizontal crossed dipole trap [36], respectively, in 2004.

An inverse approach of mapping a system of strongly interacting quasi-1D fermions to weakly interacting one-dimensional bosonic system was employed by Granger and Blume in 2004 [79].

Chapter 2

Spatial adiabatic passage

2.1 Introduction and motivation

For many applications in the field of quantum engineering, such as matter wave interferometry, quantum metrology and quantum computing, it is crucial to be able to control the spatial degrees of freedom of the atoms [80–86]. In case of particle transport, the usual approach consists of trying to control the direct tunneling of particles between adjacent traps by manipulating the potential barriers between them. The fidelity of this approach depends strongly on the method and the timing of the potential barrier manipulations, and usually results in a well-known Rabi-like oscillations between the two coupled traps.

An alternative approach, **spatial adiabatic passage** (SAP), follows a specially engineered eigenstate of the system to transfer a particle between two distant traps. This ability to follow the eigenstate relies on the adiabatic theorem which states that in the absense of level crossings the system will remain an eigenstate if it is driven slowly enough as not to introduce any excitations [87, 88]. Unlike direct tunneling, high-fidelity particle transfer using SAP processes is robust for a large range of system parameters [89], and is thus a good quantum engineering tool for the aforementioned applications. Various shortcuts which speed up adiabatic processes can be used to rectify the major drawback of SAP, its time requirement [90–93].

Since its first appearance in the work by Eckert *et al.* [89], the SAP protocol has been extensively studied [94–96] and extended to quantum dots [97], waveguides [98], multiple dimensions [99] and particles [1, 100, 101]. Many new application were explored, such as hole transport [85], vibrational state filtering [102] and particle separation [103].

2.2 The spatial adiabatic passage

The essense of the single-particle spatial adiabatic passage can be more easily understood if we consider a model with three harmonic traps in 1D (see Fig. 2.1) [89]

$$V(x) = \frac{1}{2} m\omega^2 \min\left[(x + d_{12})^2, x^2, (x - d_{23})^2\right]. \tag{2.1}$$

In this external potential d_{12} and d_{23} are the distances between the centers of the left and middle traps and the middle and right traps, m is the particle mass and ω is the

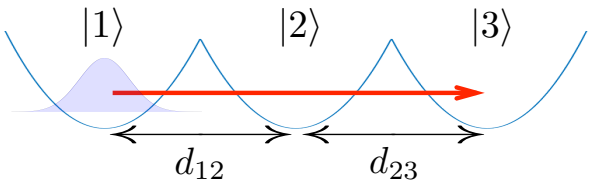

Figure 2.1: Schematic of a SAP setup using a triple harmonic trap system. The ground states of the left, middle and the right traps are given by $|1\rangle$, $|2\rangle$, and $|3\rangle$, respectively. The distances d_{12} and d_{23} between the traps can be changed independently to achieve a high fidelity transfer of a particle from the left trap to the right one.

frequency of the harmonic traps, identical for all three traps to ensure tunnelling resonance. From here on I use natural units with energies measured in $E_\mathrm{u} = \hbar\omega$, which is proportional to the ground state energy of the harmonic oscillator, and lengths measured in $L_\mathrm{u} = \sqrt{\hbar/(m\omega)}$, which corresponds to the ground state size of the harmonic oscillator. We assume that the particle is initially in the ground state of the left trap. Assuming adiabatic time evolution, we can describe this system using only the ground states of the traps, $|1\rangle, |2\rangle$ and $|3\rangle$. Such a system is effectively three-level, and can be desribed by the Hamiltonian

$$\hat{H}(t) = \hbar \begin{pmatrix} 0 & \Omega_{12}(t) & 0 \\ \Omega_{12}(t) & 0 & \Omega_{23}(t) \\ 0 & \Omega_{23}(t) & 0 \end{pmatrix}, \tag{2.2}$$

where the Ω_{ij} are the coupling frequencies between the states $|i\rangle$ and $|j\rangle$. The coupling frequencies depend on the distance between the traps d_{ij} for $i, j = 1, 2, 3$. One of the eigenstates of this Hamiltonian with zero eigenvalue, the so-called *dark state*, involves only the left and the right traps

$$|D(\theta)\rangle = \cos\theta|1\rangle - \sin\theta|3\rangle, \quad \tan\theta = \frac{\Omega_{12}}{\Omega_{23}}. \tag{2.3}$$

If we follow the ground state by adiabatically changing the distances between the traps in such a way that the mixing angle θ changes from 0 to $\pi/2$, a particle initially trapped in the left trap will be transferred to the right trap. In terms of the tunneling rates, $\theta = 0$ corresponds to the ratio of the tunneling rates $\frac{\Omega_{12}}{\Omega_{23}}$ being very small. This can be achieved if the distance between the left and the middle traps is much larger than the distance between the middle and the right traps. The mixing angle $\theta = \pi/2$ corresponds to the reversed ratio $\frac{\Omega_{23}}{\Omega_{12}}$ being very small, meaning that $d_{23} \gg d_{12}$. The way the traps have to be brought closer and then separated is rather counter-intuitive because the empty right and the middle traps approach each other before the left trap starts moving. This process for the three-level approximation is shown in Fig. 2.2 (a), with the top dot-dashed blue line corresponding to the center of the right trap and the bottom red dashed line tracing the center of the left trap. First the right trap adiabatically approaches the middle trap while the left trap is still far away, then the left trap starts moving closer to the middle, passing the point when both traps are equidistant from the middle ($\theta = \pi/4$). Finally, the right trap moves back towards its

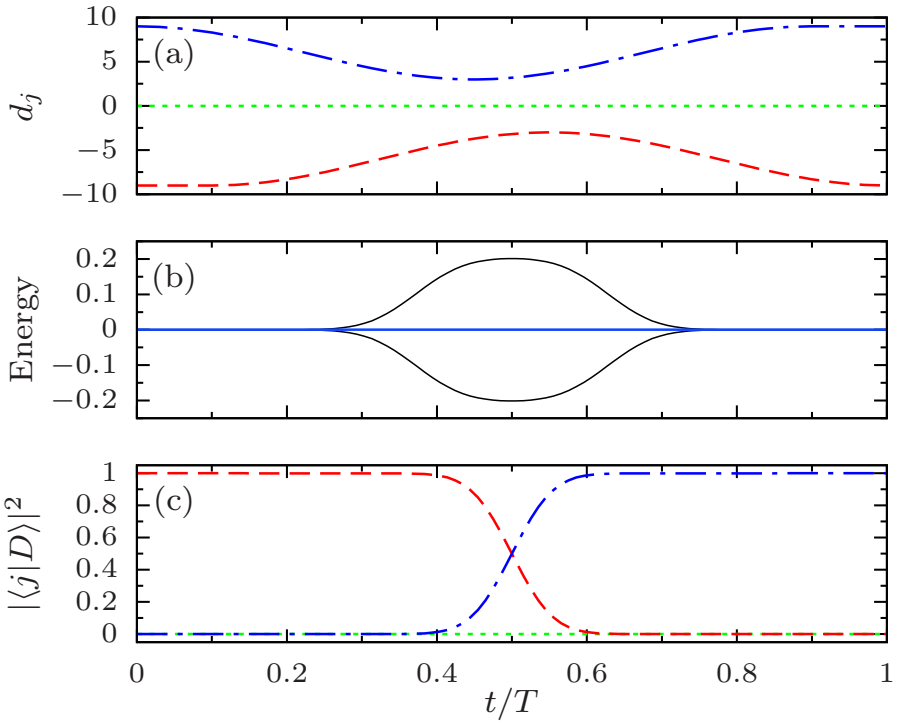

Figure 2.2: (a) Positions of the three harmonic well minima for the SAP protocol [1] (dashed red: d_1, dotted green: d_2, dot-dashed blue: d_3). The initial (and final) distance between wells is $d_{\max} = 9$, ensuring to tunneling occurs between the middle and the outward traps on the timescales of the process. The minimum distance is $d_{\min} = 3$ and the time delay between the two approaches is $T/10$, where T is the total time of the process. (b) Energy eigenvalues of the single-particle Hamiltonian (2.2), with the one corresponding to $|D\rangle$ displayed in blue. (c) Coefficients of $|D\rangle$ in the $\{|j\rangle\}$ basis (dashed red: $|1\rangle$, dotted green: $|2\rangle$, dot-dashed blue: $|3\rangle$).

initial position while the left trap is still relatively close to the middle. The middle trap stays stationary throughout the whole process.

The eigenenergies of the Hamiltonian 2.2 at each step of the SAP process are shown in Fig. 2.2 (b), with the dark state energy highlighted as thick blue line. Initially all eigenstates start as degenerate, split in the middle of the process due to non-zero coupling, and finally revert back to degeneracy.

Fig. 2.2 (c) demonstrates the occupation dynamics during the SAP process for the left (dashed red), middle (dotted green) and right (dot-dashed blue) traps. It is easy to see that initially the atom is entirely in the ground state of the left trap. The left and the right traps then gradually swap population while the occupation of the middle trap stays negligible.

The SAP process does not depend on the exact shape of the movement, but instead depends only on the relative coupling strengths between the traps, making it robust to experimental uncertainties. There are no peer-reviewed accounts of experiments demostrating SAP with massive particles to date, but high fidelity transfer of light using SAP has been achieved in wave guides [104], which is analogous to the single-particle SAP. This analogy can be explained by considering a system where monochromatic

light propagates in three thin coplanar waveguides with only the fundamental mode considered [104]. In this case the direction of propagation plays a role of the temporal component in the Schrödinger equation, and the movement of the traps is replaced with the change of the coupling between adjacent waveguides.

2.3 Transfer of two interacting particles

In the non-interacting case, the SAP protocol can be readily generalized to arbitrary number of particles, but the presence of finite interactions adds significant complications due to the loss of tunnelling resonances [1]. Below I will discuss the SAP protocol for transfer of two particles that was investigated in [1], as it is essential to understand a more general case with arbitrary number of particles.

In case of two particles the continuum space Hamiltonian is

$$\hat{H} = -\frac{1}{2}\frac{\partial^2}{\partial x_1^2} - \frac{1}{2}\frac{\partial^2}{\partial x_2^2} + V(x_1) + V(x_2) + g\delta(x_1 - x_2). \tag{2.4}$$

The interaction strength g can be calculated from the energy spectrum of two particles in a harmonic trap [105]

$$g = -\frac{2\sqrt{2}\Gamma(1 - E_g/2)}{\Gamma((1 - E_g)/2)}, \tag{2.5}$$

where $\Gamma(E)$ is the gamma function. From this we can define interaction energy U_{int} as

$$U_{\text{int}} = E_g - 2E_0, \tag{2.6}$$

Where E_0 is the single-particle ground state energy and E_g is the two-particle ground state energy of the harmonic trap.

We are interested in the transfer of both particles from the left trap into the right trap, meaning that initially both particles are in the ground state of the left trap $|\psi_{\text{init}}\rangle = |2\ 0\ 0\rangle$, and in the target state both particles are in the ground state of the right trap $|\psi_{\text{t}}\rangle = |0\ 0\ 2\rangle$. By numerically simulating the two-particle SAP process for different interaction strengths g and plotting the fidelity of the two-particle process against g [1], one finds the existence of a range of intermediate interaction strengths where the fidelity remains high (see Fig. 2.3). The non-interacting case $g = 0$ predictably results in high fidelity transport due to independent tunneling of the two particles, and the Tonks–Girardeau limit case $g = \infty$ can be mapped onto a system of non-interacting fermions, resulting in essentially single particle tunnelling and giving similarly high fidelity.

In order to understand what is happening in the high fidelity plateau, we need to look closer at how the band structure of the energy spectrum of the Hamiltonian evolves during the SAP process [1] (see Figs. 2.4 and 2.5).

The states where the particles are separated into different traps have an energy around $E_g = 1$ and are contained in the lowest energy band shown in Figs. 2.4 (a-b) and 2.5 (a-b). The energy boundaries of the next band depend on the interaction strength, and this band contains the states where both particles are in the same trap. The two-particle dark state, similar to the one discussed in Eq. (2.3), is also within

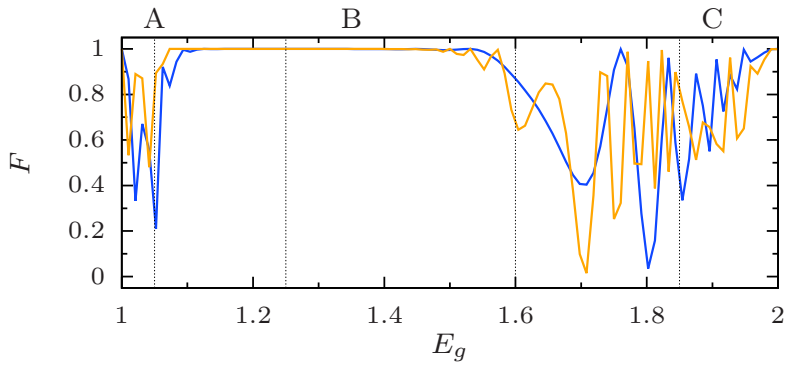

Figure 2.3: Final population in state $|0\ 0\ 2\rangle$ as a function of E_g after the two-particle SAP protocol is carried out over a total time $T = 4000$ (blue) or $T = 12000$ (orange). Dotted vertical lines indicate energies for which the spectrum is shown in Figs. 2.4 and 2.5 [1].

this band, and is shown in blue in plots (c-d) of both figures. Higher bands contain higher excited states of the particles.

The dynamics of the Fock state composition of the dark state are shown in Figs. 2.4 and 2.5 (e-f). It is easy to see that within the high fidelity plateau the dark state bands ($E_g \approx 1.25$ and $E_g \approx 1.6$) remain isolated from other bands, and the dynamics of the Fock states are simpler and closer to the single particle behaviour than for the states from the low-fidelity regions. For these values it is therefore possible to adiabatically follow the dark state using the SAP protocol, resulting in high-fidelity transport of both particles [1]. For values of interaction energies outside of the plateau the dark state has many crossings and is hard to follow adiabatically, resulting in low fidelity transfer.

Due to the effective single-particle behaviour of the repulsively bound pair in the intermediate regime [106], all single particle protocols can be used, particularly one can engineer a two particle NOONstate by tuning θ from 0 to $\frac{\pi}{4}$. The final state of the system after the $\frac{\pi}{4}$-SAP is $\frac{1}{\sqrt{2}}(|2\ 0\ 0\rangle - |0\ 0\ 2\rangle)$, with $|2\ 0\ 0\rangle$ and $|0\ 0\ 2\rangle$ denoting states with two particles in the left and in the right trap respectively. Such NOONstates are maximally entangled, and are considered an important resourse in quantum engineering and metrology [101, 107], as they allow for phase measurements that can reach the fundamental Heisenberg limit [108].

2.4 Particle separation

The existence of the dark state in SAP systems ensures that there is a way of high-fidelity transfer of a particle between spatially separated traps. Another question one might ask is if the SAP process can be generalized to degenerate states other than spatially localized ones. One posibility is to develop a SAP-like protocol to transfer multiple particles between different Fock states, essentially realizing coherent deterministic high-fidelity splitting or merger of clouds of interacting bosons. In the following

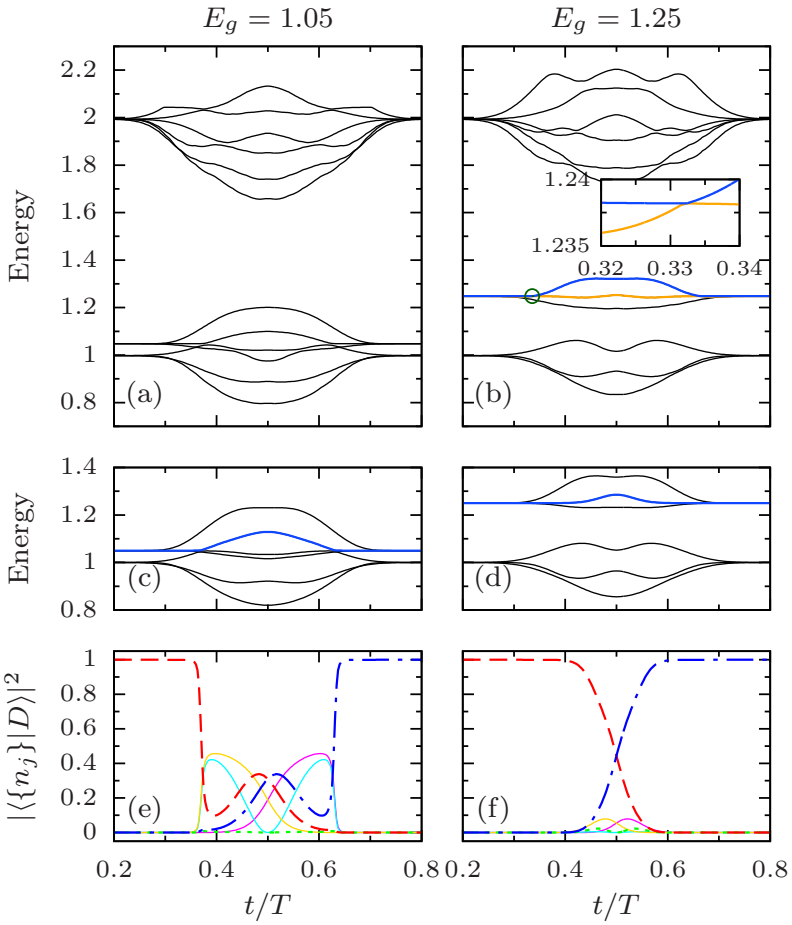

Figure 2.4: (a,b) Lowest 12 instanteneous eigenvalues of $\hat{H}$ in Eq. (2.4) for the SAP scheme with two weakly interacting particles and the trap moving sequence of Fig. 2.2(a) for (a) $E_g = 1.05$ and (b) $E_g = 1.25$. In (b) the energy of the dark state (asymptotically $|2\ 0\ 0\rangle$ and $|0\ 0\ 2\rangle$) and the state with which it couples the most are marked in blue and orange, respectively. The inset shows a zoom-in of the marked crossing between these two states (marked with a circle). (c,d) Instanteneous eigenvalues of the Bose–Hubbard Hamiltonian for the same parameters as (a,b), with the energy of the dark state drawn in blue. (e,f) Coefficients in the Fock basis of the dark states in (c,d) (dashed red corresponds to $|0\ 0\ 2\rangle$, dotted green to $|0\ 2\ 0\rangle$, dot-dashed blue to $|0\ 0\ 2\rangle$, and the solid lines to states where the two atoms are in different traps) [1].

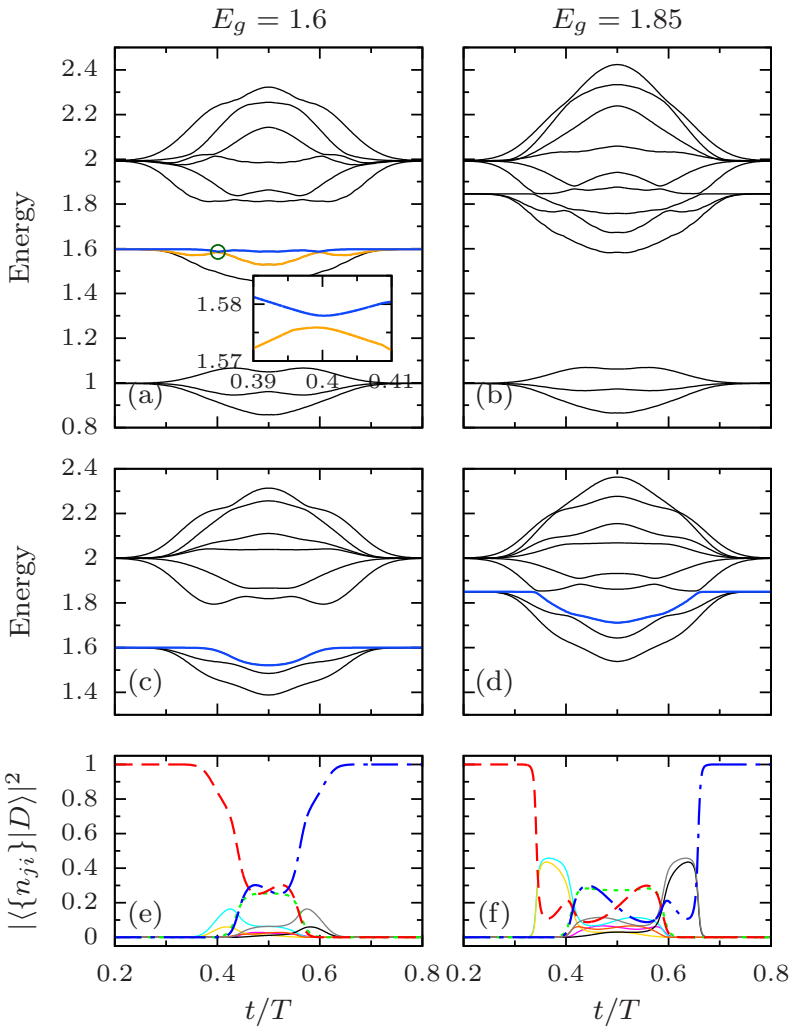

Figure 2.5: (a,b) Lowest 12 instanteneous eigenvalues of $\hat{H}$ in Eq. (2.4) for the SAP scheme with two strongly interacting particles and the trap moving sequence of Fig. 2.2(a) for (a) $E_g = 1.6$ and (b) $E_g = 1.85$. In (a) the energy of the dark state (asymptotically $|2\ 0\ 0\rangle$ and $|0\ 0\ 2\rangle$) and the state with which it couples the most are marked in blue and orange, respectively. The inset shows a zoom-in of the marked crossing between these two states (marked with a circle). (c,d) Instanteneous eigenvalues of the Fermi–Hubbard Hamiltonian for the same parameters as (a,b), with the energy of the dark state drawn in blue. (e,f) Coefficients of the dark state in (c,d) the Fock basis (color coding is the same as in Figs. 2.4(e,f)) [1].

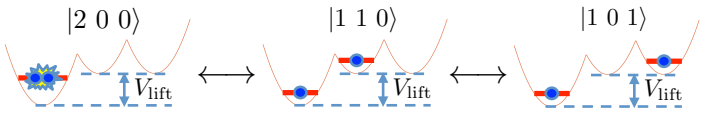

Figure 2.6: Schematic of the three-level model for particle separation. Simultaneous lift of the right and the middle harmonic traps by $V_{\text{lift}} = U_{\text{int}}$ makes the three states depicted resonant.

I will discuss a process based on SAP which is not a straightforward generalization of a single particle protocol, but which allows to split an initial many-particle state in a controlled manner.

2.4.1 Two-particle case

First I will demonstrate the process of separation of two particles initially trapped in the left trap into the left and the right traps. The initial and the target states are thus

$$|\psi_{\text{i}}\rangle = |2\ 0\ 0\rangle \ \rightarrow \ |\psi_{\text{t}}\rangle = |1\ 0\ 1\rangle. \tag{2.7}$$

If we consider the unmodified SAP as in section 2.3, the initial and the final states are in two different energy bands due to non-zero interaction. It is therefore necessary to engineer the system in such a way as to compensate for the absence of the interaction energy in the target state and match the energies of the two states. We can achieve this by lifting the middle and the right traps by $V_{\text{lift}} = U_{\text{int}}$. In case of attractive interaction the traps have to be lowered instead. This manipulation ensures the resonance condition of the states $|2\ 0\ 0\rangle$, $|1\ 0\ 1\rangle$, and $|1\ 1\ 0\rangle$ and energetically separates them from the rest of the energy spectrum. This isolation makes the system effectively three-level, with a Hamiltonian analogous to Eq. (2.2) (see Fig. 2.6). Consequently, there exist a dark-like state which involves only the initial and the target states. The usual SAP positioning sequence then leads to the separation of the two particles. In order to confirm that this separation scheme works, below I will present the results of simulations of the system in the continuum case. I simulate the time evolution of the initial state with two particles being in the ground state of the left trap $\psi_{\text{i}} = |2\ 0\ 0\rangle$ into the final state $\psi_{\text{f}} = |1\ 0\ 1\rangle$ obeying the full Hamiltonian Eq. (2.4) and calculate the fidelity $F = |\langle\psi_{\text{f}}|\psi_{\text{t}}\rangle|^2$ of the process. This fidelity is shown in Fig. 2.7(b) for $U_{\text{int}} \in \left[-\frac{1}{2}, 1\right]$ as a solid blue line.

Even though in the weakly-interacting regime the fidelity drops to zero due to the presence of several degeneracies, high fidelities can be seen for a large range of repulsive and attractive interactions. In the Tonks–Girardeau limit of infinitely repulsive interaction ($U_{\text{int}} = 1$) the success of the separation is easy to explain by regarding the bosons as non-interacting fermions [71]. The system then forms a harmonically trapped *Fermi sea* at zero temperature, and by lifting the middle and the right traps by $V_{\text{lift}} = 1$ we only allow the particle at the edge of the Fermi sea to tunnel. Therefore, we expect a high fidelity of the particle separation in this case.

On the other hand, the drop of fidelity in the weakly interacting case can be ex-

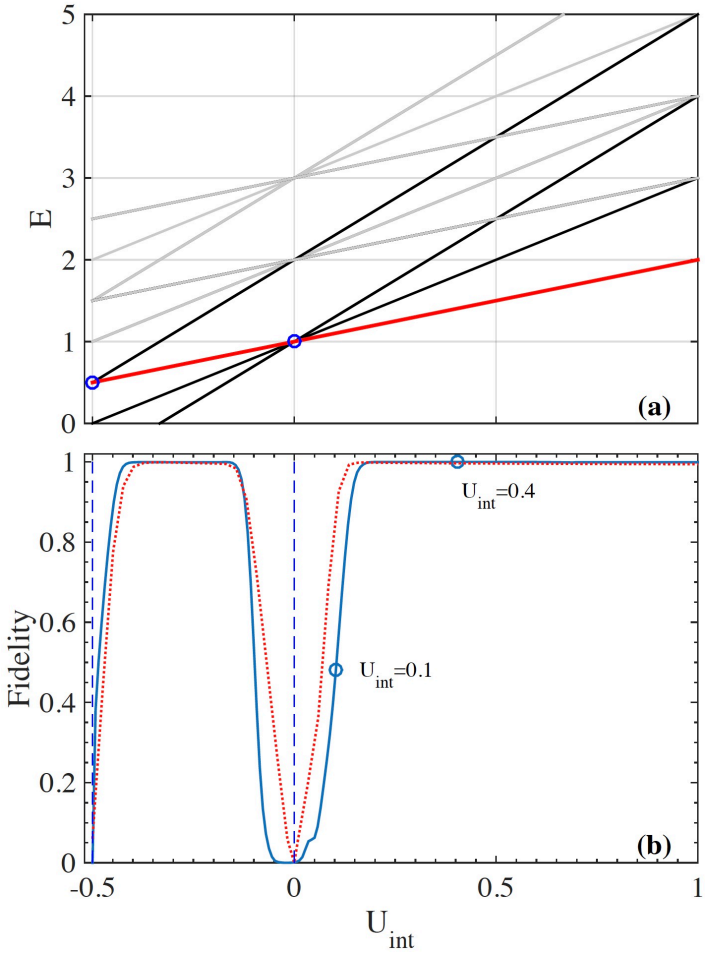

Figure 2.7: **(a)** Energy spectrum of the two-particle Fock states in the triple well system with only the lowest two energy levels in each trap considered and $V_{\text{lift}} = U_{\text{int}}$. The three degenerate states $|2\ 0\ 0\rangle, |1\ 1\ 0\rangle$ and $|1\ 0\ 1\rangle$ are in the band colored in red and additional degeneracies can be seen to appear at $U_{\text{int}} = 0$ and $U_{\text{int}} = -1/2$. **(b)** Fidelities of the particle separation process as a function of the interaction energy, obtained using the full Hamiltonian time evolution (solid blue line) and BH model (dashed red line). Degeneracies in the spectrum appear at points marked as vertical dashed blue lines. The energies E and U_{int} are given in units of $\hbar\omega$.

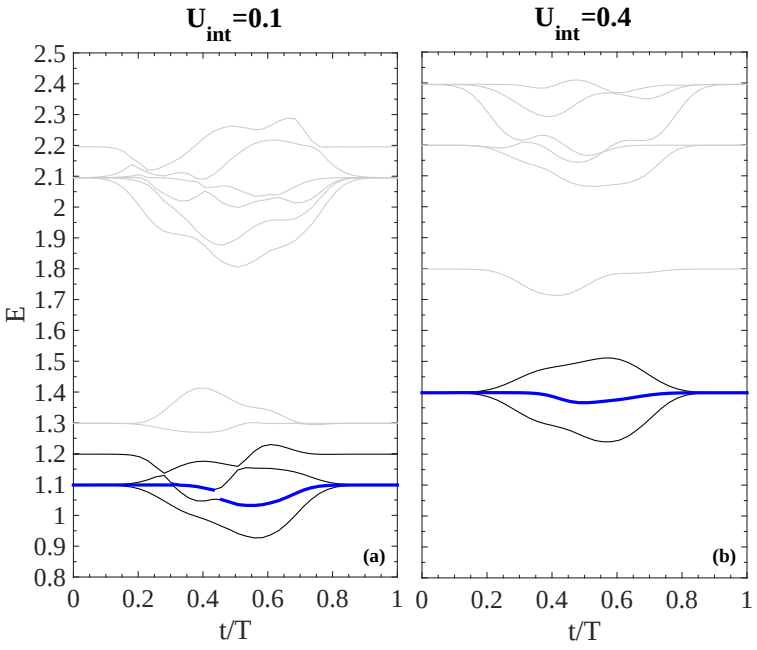

Figure 2.8: Evolution of the energy spectrum during the particle separation process for (a) $U_{\text{int}} = 0.1\hbar\omega$ and (b) $U_{\text{int}} = 0.4\hbar\omega$. The dark-like state is highlighted in blue. E is given in units of $\hbar\omega$. Total time of the process $T = 1500\frac{1}{\omega}$.

plained by looking at the energy spectrum of the separation process (Fig. 2.8) for two different values of U_{int} shown as points in Fig. 2.7(b). In the weakly interacting case ($U_{\text{int}} = 0.1$) the SAP triplet in the lowest band containing the dark state overlaps with the higher lying band, leading to multiple level crossing and difficulties in following the dark state. For stronger interactions ($U_{\text{int}} = 0.4$), the lowest band becomes isolated again, leading to high fidelity particle separation. Another region of low fidelity is visible around $U_{\text{int}} = -\frac{1}{2}$ and will be discussed in section 2.4.2.

In the next sections I will extend the separation protocol to the many particle case. However, since the numerical complexity of diagonalization and integration of the Schrödinger equation using the full Hamiltonian scale exponentially with the number of particles, I introduce a Bose–Hubbard (BH) treatment of this system. I will first compare the two-particle results obtained above with the BH model and then use the BH model to simulate the three-particle case.

2.4.2 Bose–Hubbard treatment

Let us consider a system with three harmonic traps with their ground state energies shifted by V_1, V_2 and V_3, counted from left to right. Each trap is assumed to have m_{L} vibrational states, leading to $3m_{\text{L}}$ available vibrational states in the system. Next we distribute N interacting bosons among the traps and their vibrational states and assume that if a pair of particles is located within the same trap, they interact with energy U_{int}. The number of Fock states in this system can be calculated as the number of ordered $3m_{\text{L}}$-tuples of non-negative integers summing to N, and is equal to $Q =$

$\binom{N+3m_{\mathrm{L}}-1}{3m_{\mathrm{L}}-1}$. We associate each state with a matrix $\{n_{ji}\}$, where n_{ji} is the number of particles in the j-th energy level of the i-th trap

$$|\{n_{ji}\}\rangle = \left| \begin{matrix} n_{01} & n_{02} & n_{03} \\ \cdots & \vdots\ n_{ji}\ \vdots & \cdots \\ n_{(m_{\mathrm{L}}-1)1} & n_{(m_{\mathrm{L}}-1)2} & n_{(m_{\mathrm{L}}-1)3} \end{matrix} \right\rangle. \tag{2.8}$$

The sum over all elements of the matrix gives the total number of particles $\sum_{i=1}^{3}\sum_{j=0}^{m_{\mathrm{L}}-1} n_{ji} = N$. To simplify the notation, I will denote the states with only the lowest vibrational levels of the traps occupied as

$$|\{n_{0i}\}\rangle = |n_{01}\ n_{02}\ n_{03}\rangle. \tag{2.9}$$

The Q-level Bose–Hubbard Hamiltonian of this system can then be written as

$$\begin{aligned} \hat{H}_{\mathrm{BH}} = &\sum_{j=0}^{m_{\mathrm{L}}-1}\left(j+\frac{1}{2}\right)\hat{N}_j^{\mathrm{level}} + \sum_{i=1}^{3} V_i \hat{N}_i^{\mathrm{trap}} \\ &+ \frac{U_{\mathrm{int}}}{2}\sum_{i=1}^{3}\hat{N}_i^{\mathrm{trap}}\left(\hat{N}_i^{\mathrm{trap}}-1\right) + H_{\mathrm{tunnel}}. \end{aligned} \tag{2.10}$$

Here a_{ij} is the bosonic annihilation operator in the j-th level of trap number i, and $\hat{n}_{ji} = \hat{a}_{ji}^{\dagger}\hat{a}_{ji}$ is the associated particle number operator. We can obtain the total number of particles in the i-th trap as

$$\hat{N}_i^{\mathrm{trap}} = \sum_{j=0}^{m_{\mathrm{L}}-1}\hat{n}_{ji}, \tag{2.11}$$

with corresponding eigenvalues N_i^{trap}. The total number of particles in the j-th vibrational state is

$$\hat{N}_j^{\mathrm{level}} = \sum_{i=1}^{3}\hat{n}_{ji}. \tag{2.12}$$

with eigenvalues N_j^{level}.

Eq. (2.10) has four terms. The first two term, $\sum_{j=0}^{m_{\mathrm{L}}-1}\left(j+\frac{1}{2}\right)\hat{N}_j^{\mathrm{level}} + \sum_{i=1}^{3} V_i\hat{N}_i^{\mathrm{trap}}$, correspond to the single particle energies in each trap and vibrational state. The third term, $\frac{U_{\mathrm{int}}}{2}\sum_{i=1}^{3}\hat{N}_i^{\mathrm{trap}}\left(\hat{N}_i^{\mathrm{trap}}-1\right)$, describes the interparticles interactions. The last term H_{tunnel} accounts for all tunneling events. Calculating the coupling strengths between all possible states of the system is a computationally difficult task, so I use an approximation where the tunneling events are expressed in terms of n-particle co-tunneling terms, which are expressed in terms of two-particle tunneling. The details of these calculations are presented in the methods section 5.2.

When the traps are widely separated such that no tunneling is occuring on the time scales of interest, the last term of the Hamiltian $\hat{H}_{\mathrm{BH}}$ can be ignored. The first three terms have the Fock states $|\{n_{ji}\}\rangle$ as their eigenstates. The corresponding eigenenergies $E_{\mathrm{total}}(\{n_{ji}\})$ then depend only on the interaction U_{int} and the shift of the potential

energy V_i. If we consider the states with only the lowest vibrational states occupied $|n_{01}\ n_{02}\ n_{03}\rangle$, we can further simplify the expression for E_{total} as

$$E_{\text{total}}(\{n_{0i}\}) = \frac{N}{2} + \sum_{i=1}^{3} V_i n_{0i} + \frac{U_{\text{int}}}{2} \sum_{i=1}^{3} n_{0i}(n_{0i} - 1). \tag{2.13}$$

The resonance condition between two Fock states, $|\{n_{ji}\}\rangle$ and $|\{n'_{ji}\}\rangle$, can be written as

$$E_{\text{total}}(\{n_{ji}\}) = E_{\text{total}}(\{n'_{ji}\}), \tag{2.14}$$

and it can be used to find the necessary potential energy shifts to engineer the SAP triplet of resonant states ($|2\ 0\ 0\rangle$, $|1\ 1\ 0\rangle$, and $|1\ 0\ 1\rangle$) for the particle separation protocol

$$V_1 = 0; \quad V_{\text{lift}} = V_2 = V_3 = U_{\text{int}}. \tag{2.15}$$

The predicted fidelities of the separation process using this discreet model can be seen in Fig. 2.7(b) as dashed red line and are very similar to the ones obtained using the full Hamiltonian. Both methods have high fidelity plateaus and drop to zero around $U_{\text{int}} = 0$ and $-\frac{1}{2}$. These drops can be explained by examining the spectrum of the two-particle Fock states, shown in Fig. 2.7(a), of the BH model with only the lowest two Bloch bands ($m_{\text{L}} = 2$) considered. The red line shows the energy of the degenerate SAP triplet and the black lines highlight energies of other relevant Fock states. The SAP triplet band crosses other Fock states exactly at $U_{\text{int}} = 0$ and $U_{\text{int}} = -1/2$, explaining the drops in fidelity around these values. For example, at $U_{\text{int}} = -1/2$, the SAP triplet crosses the band containing states where one particle is in the ground state of the middle or the right trap and the other is in the first excited state of the same trap.

Having demonstrated that the proposed BH-like model captures the main features of the full model, I will use it in the following to simulate particle separation processes for larger numbers of particles.

2.4.3 N-particle case

In this section I will show that it is possible to separate exactly M particles out of a cloud of N particles trapped in the left trap. Although the preparation of a state of exactly N particles in the ground state of a trap is a challenging problem, a recent experiment has shown the possibilty of doing this for a wide range of particle numbers [109]. There are two ways of separating M particle out of N in a three traps setting: to have exactly M particle remain in the left trap or to have excatly M particles transferred into the right trap. I will first consider the former case, followed by the latter, and explain the differences between the two cases.

For the first case of M particles remaining in the left trap the initial and the target states are given by

$$|\psi_{\text{i}}\rangle = |N\ 0\ 0\rangle \ \rightarrow\ |\psi_{\text{t}}\rangle = |M\ 0\ (N-M)\rangle. \tag{2.16}$$

The degeneracy conditions in Eqs.(2.13)–(2.14) give the formula for the trap lift

$$V_1 = 0; \quad V_{\text{lift}} = V_2 = V_3 = MU_{\text{int}}. \tag{2.17}$$

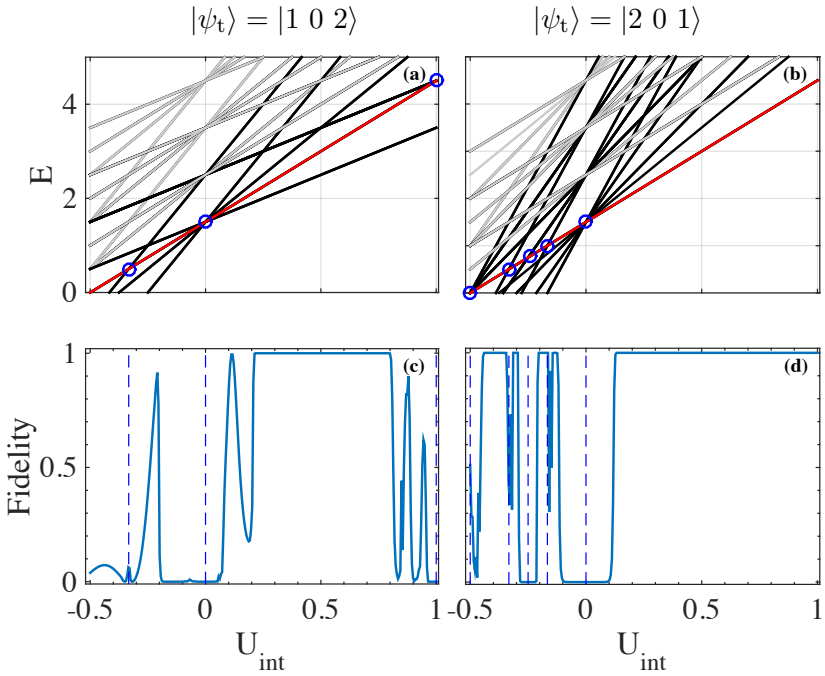

Figure 2.9: (a) Energy spectrum of three-particle Fock states in the BH model for $m_L = 2$ for the target state $|1\ 0\ 2\rangle$ (and $V_{\text{lift}} = U_{\text{int}}$). The energy of the SAP triplet is highlighted in red. (c) Corresponding particle separation fidelities. (b,d) are the same as (a,c) but for $|2\ 0\ 1\rangle$ (and $V_{\text{lift}} = 2U_{\text{int}}$). The circles in the top row and vertical dashed lines in the bottom row indicate the positions where level crossings between the SAP triplet and other bands exist. The energies E and U_{int} are given in units of $\hbar\omega$.

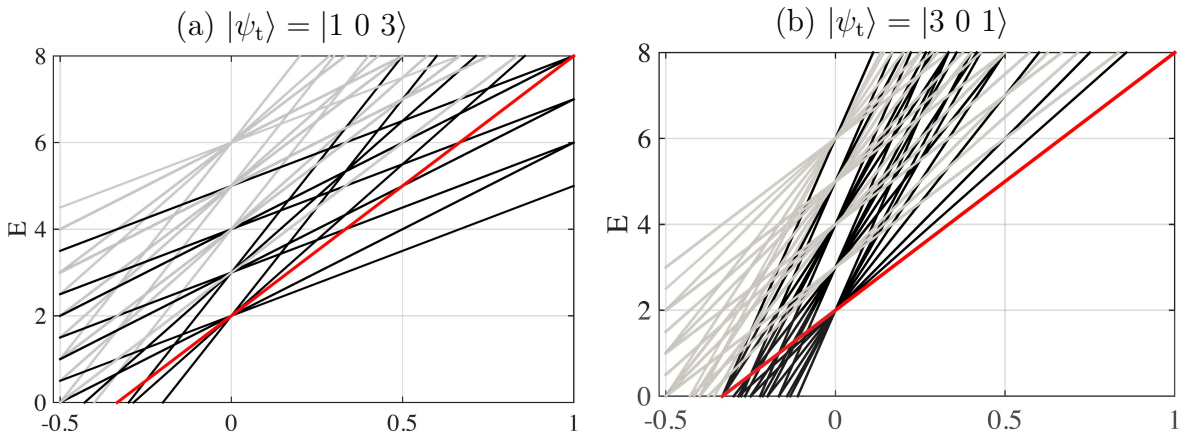

Figure 2.10: Fock energies versus two-particle interaction energy for the separation of one particle from a cloud of four. (a) Separation of one particle into the left trap $|\psi_t\rangle = |1\ 0\ 3\rangle$. (b) Separation of one particle into the right trap $|\psi_t\rangle = |3\ 0\ 1\rangle$.

An important note is that the value of the lift does not depend on the initial number of particles N. This means that it is not necessary to know the initial number of particles in order to keep exactly M particles in the left trap after the separation process. This fact makes it much easier to prepare the initial state in experiments.

To prove that the protocol results in a high-fidelity separation of the particles, let us first consider the case of $N = 3$ for which we want to leave one particle in the left trap. The target state is then $|\psi_t\rangle = |1\ 0\ 2\rangle$, and only two vibrational states are necessary to consider in the Fock state energy claculation in the Bose–Hubbard model described before. The Fock state energies are shown in Fig. 2.9(a). It is apparent from the figure that degeneracies appear at $U_{\text{int}} = \{-\frac{1}{3}, 0, 1\}$, which lead to fidelity drops around these interaction energy values, see Fig. 2.9(c). As we increase the number of particles, the energy spectrum will contain more and more bands, leading to more degeneracies (see Fig. 2.10). This leads to fragmentation of the region of high fidelity separation for $|N\ 0\ 0\rangle \to |1\ 0\ (N-1)\rangle$.

Let us now consider a process where we separate M particles into the right trap

$$|\psi_i\rangle = |N\ 0\ 0\rangle \ \to \ |\psi_t\rangle = |(N-M)\ 0\ M\rangle. \tag{2.18}$$

From the Eqs.(2.13)–(2.14) we know that the traps have to be lifted according to

$$V_1 = 0; \quad V_{\text{lift}} = V_2 = V_3 = (N-M)U_{\text{int}}. \tag{2.19}$$

The number of separated particles $N - M$ matters in this case, meaning that we have to know their initial number N as well as M. This additional requirement does indeed make the protocol more demanding, but if we only want to separate one particle ($M = 1$), the lift ensures that the SAP triplet is isolated from other Fock states for any N in the repulsive regime. While for attractive interactions there are multiple level crossings visible in Fig. 2.9(b), the energy of the SAP triplet is the lowest for any repulsive value of U_{int}. This isolation of the SAP triplet results in a broad plateau of high fidelity particle separation. If we increase the number of particles N further while

keeping $M = 1$, the spectrum becomes denser (see Fig. 2.10(b)), but the SAP band remains the lowest over the whole repulsive range.

During the SAP process the traps have to be brought close to each other, and thus the tunneling term cannot be ignored anymore. The changes in coupling strength between the traps in the SAP process lead to non-zero band widths, which will result in additional level crossings and shrinking of the high fidelity plateau around the degeneracies. In principle, the bands can be kept arbitrarily narrow by controlling the minimum approach distance between the traps, but the total time of the process will have to increase to allow for co-tunneling to happen.

Above I have shown that it is possible to separate an exact number of particles from a cloud of ultracold interacting bosons by ensuring the degeneracy of the initial $|N\ 0\ 0\rangle$, the intermediate $|(N-M)\ M\ 0\rangle$ and the target $|(N-M)\ 0\ M\rangle$ states. These three states form a SAP triplet, and there are regions of interaction strengths where the dark-like state connects the intitial and the target states without aditional level crossings. In such a region the SAP triplet remains isolated from the rest of the spectrum, allowing the dark state to be followed and resulting in high fidelity splitting of the cloud. However, the number of level crossings depends on $N - M$, leading to rapid fragmentation of the high fidelity regions. Since the speed of the process and its tolerance to imperfections in execution depends on the number of particles and their interaction strengths, it is important to study the process in an experimentally realistic system.

2.5 Radio frequency traps

While harmonic potential are very easy to work with in theoretical setting, in an experimental setting with multiple traps the harmonic approximation usually breaks down due to overlap between two individual traps. Below I will therefore examine the theory of the realistic radio-frequency (RF) trapping, propose the particle separation protocol using three RF traps and analyse its fidelity. The reason why I chose RF traps lies in their flexibility and the narrowness of the RF resonances, making it easy to have multiple traps which can be moved independently of each other [110–112]. The principle of RF trapping lies in engineering of a spatially-dependent separation of the magnetic sublevels of an atom using inhomogeneous magnetic field, and then creating the effective potential extrema at desired coordinates using RF pulses of appropriate frequency.

Let us consider an atom with two hyperfine sublevels ($m_F = \pm\frac{1}{2}$) in an inhomogeneous magnetic field, $B(x) = bx$ and a linearly polarized RF field, $\vec{B}_{\mathrm{rf}} \cos(\omega t)$. The atom will experience an external potential with a minimum at position x_0 corresponding to the resonance condition $\mu g_F m_F b x_0 = \hbar\omega$ [113], where $\mu \approx 9.27 \times 10^{-24}$ A/m^2 is the Bohr magneton and g_F is the atomic g-factor. We can create multi-trap potentials using multiple RFs[113] and a triple-well setup can be realised using six different frequencies [111] (see Fig. 2.11). The resulting potential then is essentially given by a piece-wise function contributing the effects of each radio frequency within its vicinity. The external potential experienced by the atom is then described by [111, 113]

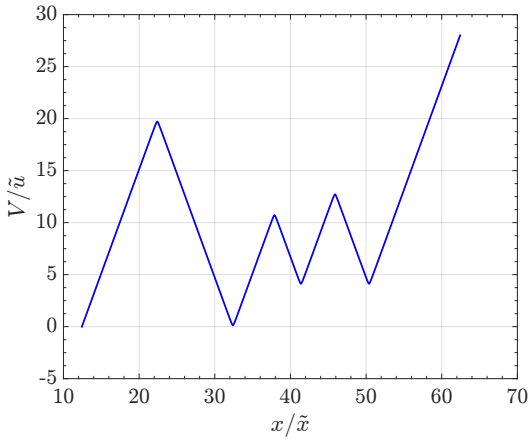

Figure 2.11: Triple-well RF potential generated using six different frequencies and the parameters given in the text. The position of the left trap is fixed at $x_1 = 20\ \tilde{x}$ and the corresponding RF is $\omega_2^0 = \mu g_F b x_1/\hbar \approx 596$ kHz. The maximum distance between the middle and the left or the right trap is $d = 9\ \tilde{x}$ and the corresponding minimum distance is $d_{\min} = 6\ \tilde{x}$. The difference between frequencies at time $t = 0$ is $\Delta\omega = \mu g_F b d/(2\hbar) \approx 134$ kHz and the frequency for the left trap edge is $\omega_1^0 = \omega_2^0 - 2\Delta\omega \approx 328$ kHz. All the other frequencies are $\omega_i^0 = \omega_2^0 + (i-2)\Delta\omega,\ i = 3, \ldots, 6$.

$$V_+(x) = (-1)^{n(x)} \left[E_+(x) - \frac{\hbar\omega_{n(x)}}{2} \right] - \sum_{k=1}^{n(x)-1} (-1)^k \hbar\omega_k, \tag{2.20}$$

where

$$E_+(x) = \frac{1}{2}\sqrt{\hbar^2\Omega^2 + (\mu g_F b x - \hbar\omega_{n(x)} + 2L_{n(x)}(x))^2}, \tag{2.21}$$

and

$$L_n(x) = \sum_{j\neq n} \frac{\hbar^2\Omega^2}{4[\mu g_F b x - \hbar\omega_j]} \tag{2.22}$$

is the combined Stark shift of all frequencies. The number of the frequency $n(x)$ is chosen such that $\mu g_F b x - \hbar\omega_{n(x)}$ is minimized for all x, i.e., $n(x)$ is the label of the most relevant (closest) frequency at each point. The distance between the traps as well as their ground state energies (which depend linearly on the trap lift) can be controlled by changing the ω_i, which can be done with great precision [114].

In our simulations we use experimentally realistic parameters as follows: the magnetic field gradient is $b = -213$ G/cm, the atomic g-factor is $g_F = -\frac{1}{2}$, the Rabi frequency is $\Omega = 2\pi \times 0.5$ kHz and the mass of a ^{87}Rb atom is $m_{\mathrm{Rb}} = 1.44 \times 10^{-25}$kg. For convenience I scale all lengths by $\tilde{x} = (4\hbar^2/\mu g_F b m_{\mathrm{Rb}})^{\frac{1}{3}} \approx 3.18 \times 10^{-7}$ m, time by $\tilde{t} = (16\hbar m_{\mathrm{Rb}}/(\mu g_F b)^2)^{\frac{1}{3}} \approx 1.34 \times 10^{-4}$ s, and energy by $\tilde{u} = m_{\mathrm{Rb}}\tilde{x}^2/\tilde{t}^2 \approx 7.85 \times 10^{-31}$ J. In these units, the Tonks–Girardeau regime is achieved at $U_{\mathrm{int}}^{\mathrm{TG}} \approx 1.64\tilde{u}$ (calculated numerically).

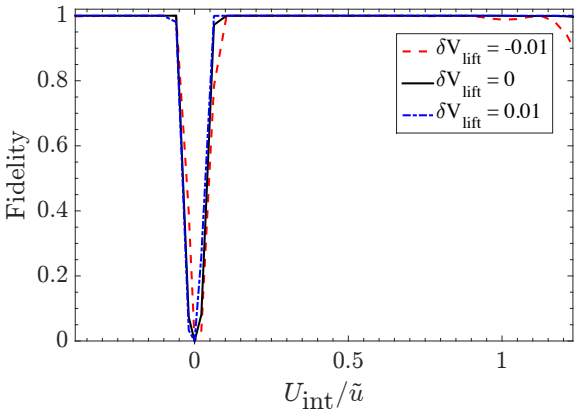

Figure 2.12: Fidelity of the particle separation protocol in the RF traps with perfect and perturbed maximum lift values. The fidelity results for very strong interactions up to the Tonks–Girardeau regime $U_{\mathrm{int}}^{\mathrm{TG}} \approx 1.64\tilde{u}$ suffer from numerical instabilities and are not shown on the plot.

2.5.1 Particle separation

To implement the particle separation protocol in the RF traps, I use the following time-dependencies of the RFs

$$\omega_1(t) = \omega_1^0 - \frac{V_{\mathrm{lift}}}{\hbar} \tag{2.23a}$$
$$\omega_2(t) = \omega_2^0 \tag{2.23b}$$
$$\omega_3(t) = \omega_3^0 + \frac{1}{2} f_1(t) + \frac{V_{\mathrm{lift}}}{\hbar} \tag{2.23c}$$
$$\omega_4(t) = \omega_4^0 + f_1(t) \tag{2.23d}$$
$$\omega_5(t) = \omega_5^0 + \frac{1}{2}(f_1(t) + f_2(t)) \tag{2.23e}$$
$$\omega_6(t) = \omega_6^0 + f_2(t), \tag{2.23f}$$

where V_{lift} is the maximum lift value and

$$f_1(t) = -\frac{\mu\, g_F\, b\, d_{\mathrm{min}}}{\hbar} f(t, 0), \tag{2.24a}$$
$$f_2(t) = -\frac{\mu\, g_F\, b\, d_{\mathrm{min}}}{\hbar} \left[f(t, 0) + f(t, \delta t) \right], \tag{2.24b}$$
$$f(t, \delta) = \begin{cases} \sin^2\left(\frac{2\pi(t-\delta)}{T}\right) & 0 \leq t - \delta < \frac{T}{2}, \\ 0 & \text{otherwise.} \end{cases} \tag{2.24c}$$

Here δt is the trap movement delay, d_{min} is the minimum distance between the middle and the left or the right traps and T is the total time of the process.

Unlike in the previous section where the middle and the right traps were lifted to ensure the resonance condition was met, in the RF case I lower the leftmost trap by V_{lift}, which is equivalent. Only radio frequencies ω_1 and ω_3 are affected by the shift in this case (see Eq. (2.23)).

The separation process starts with two atoms prepared in the ground state of the left trap with total energy E_g. The energy shift value is $V_{\text{lift}} = U_{\text{int}} = E_g - E_0$, where E_0 is the ground state energy of two non-interacting atoms in the left trap. Both E_g and E_0 are calculated numerically by direct diagonalization of the Hamiltonian. The solid black line in Fig. 2.12 shows the resulting fidelities of the particle separation process, and indicates that high fidelity can be achieved for the whole range of repulsive interactions in this setting once U_{int} is large enough. Unfortunately, for very large interaction strength g the numerical simulations suffer from numerical errors, and is not shown in the Fig. 2.12.

In order to verify the robustness of the protocol we need to account for possible experimental uncertainties in the interaction energy measurement. In Fig. 2.12 we present the particle separation fidelities obtained for a protocol with small errors in the energy shift. Both negative and positive perturbations δV_{lift} are considered, and the effective energy shift value used in the simulation is calculated as $V_{\text{eff}} = V_{\text{lift}} + \delta V_{\text{lift}}$. It is apparent that the proposed RF implementation of the separation protocol is robust against small errors in the interaction energy measurements as well as against an imperfect execution of the lowering of the left trap. This, together with the knowledge that the original SAP protocol is robust against potential shaking and tilt[89], makes process discussed here experimentally viable.

It is important to note that the model we use to describe the RF traps is valid only when the traps are sufficiently far away from each other [113], otherwise the potential in the model loses continuity and no longer describes the physical reality. I have taken this limitation into account in the simulations by ensuring that the closest approach of two frequencies leads to a discontinuity smaller than 0.01 $\tilde{u}$, which has a negligible effect on the dynamics. Furthermore, althought the lowering of the left trap also affects the middle trap, this effect is very small (on the order of 0.002 $\tilde{u}$) and therefore does not significantly affect the process fidelity.

2.5.2 Scaling with the number of particles

Finally, let us discuss the limitations and scaling of the particle separation protocol. If the initial number of particles N is increased, the energy spectrum becomes more fragmented, making it harder to follow the SAP triplet.

To quantify this observation I define the size of the maximum energy gap, ΔE, between the SAP triplet and the neighboring bands as a function of the initial and final number of particles in the left trap over the whole range of repulsive interactions. I also determine the value of the interaction strength corresponding to this maximal energy gap, $U_{\text{int}}^{\text{opt}}$, and the distance between the two points at which the SAP triplet crosses other bands, ΔU_{int}. This value can be interpreted as a tolerance value for hitting the right interaction energy $U_{\text{int}}^{\text{opt}}$ for the best separation fidelity. These values are schematically shown in Fig. 2.13.

Since at the point $U_{\text{int}}^{\text{opt}}$ the process works best, it gives a good insight into its limitations: 1) ΔE quantifies how hard it is to follow the SAP state and 2) ΔU_{int} indicates how fragmented the region, in which a high fidelity process can be expected,

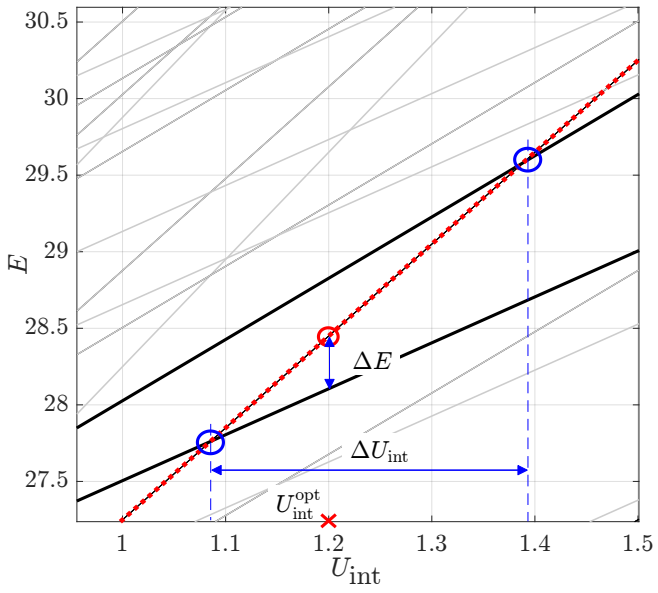

Figure 2.13: Schematic indicating the definitions of ΔE, ΔU_{int}, and $U_{\text{int}}^{\text{opt}}$ in the Fock space energy spectrum. The dotted red line corresponds to the energy of the SAP triplet, and the black and gray lines show the energies of the other Fock states in the system. The blue circles indicate the points of intersection of the SAP triplet energy band with the closest, neighbouring energy bands.

has become

$$\Delta E = \max_{U_{\text{int}}>0} \min_{f\in F} \left| E_{f_*}(U_{\text{int}}) - E_f(U_{\text{int}}) \right|, \tag{2.25a}$$

$$U_{\text{int}}^{\text{opt}} = \arg\max_{U_{\text{int}}>0} \min_{f\in F} \left| E_{f_*}(U_{\text{int}}) - E_f(U_{\text{int}}) \right|, \tag{2.25b}$$

$$\Delta U_{\text{int}} = \max_{j\in P}(U_{\text{int}}^{j+1} - U_{\text{int}}^{j}), \tag{2.25c}$$

where F contains all relevant Fock states, $E_{f_*}(U_{\text{int}})$ is the energy of the SAP triplet and P is the set of all indices of the ordered points of intersection $\{U_{\text{int}}^{j}\}$. These values are also schematically illustrated in Fig. 2.13.

The results of my calculations show that the value of ΔE does not depend on the initial number of particles N, but only on the numbers of particles that are to be moved out of the trap, $N-M$. This can be intuitively explained by considering the structure of the energy spectrum (see Fig. 2.9). The energy of each Fock state depends linearly on the interaction energy, intersecting $U_{\text{int}} = 0$ at points that corresponds to different combinations of excited states. The slope then depends on the number of particles in the right and the middle traps and it is easy to see that the $N-M=1$ energy band has the smallest slope, the $N-M=2$ has the second smallest slope, etc. If we increase

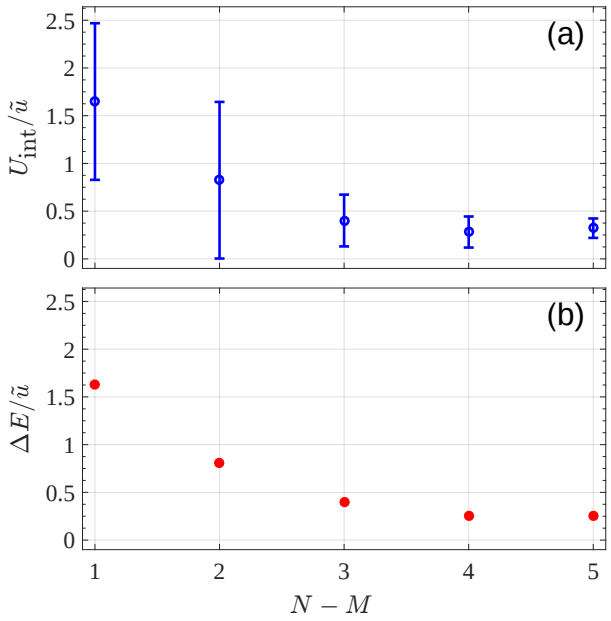

Figure 2.14: (a) Optimal interaction energy value $U_{\mathrm{int}}^{\mathrm{opt}}$ with its margin ΔU_{int} as an error bar and (b) energy gap ΔE. The Fock energy calculation are performed for RF traps using the Bose–Hubbard model for the three lowest energy bands.

$N-M$, we also need to include more excited states in the model to account for all intersections, but the overall structure does not depend on N. Unfortunately, ΔU_{int} rapidly decreases with increasing $N-M$ and in Fig. 2.14 I show this dependency. Only a few particles can be realistically separated in this manner, but this number is, in principle, independent of the initial number of particles. Thus, for any N, by using, for example, Feshbach resonances [115–117], one can tune the interaction energy to the optimal value $U_{\mathrm{int}}^{\mathrm{opt}}$ within the tolerance ΔU_{int} to separate small number of particles from the cloud of size N. In real experiment, however, the number N will be limited by the trap depth and heating of the cloud.

2.6 Entropy during the particle separation process

Many non-classical properties of many-body quantum systems are due to correlations between the particles [118]. In particular, in quantum computing entangled many-particle states are essential for the quantum speed-up promised by the theory [119], but preparation of such entangled states remains hard [120, 121]. The SAP processes decribed above are quantum engineering tools which allow us to prepare many-body entangled states deterministically with high fidelity assuming we can obtain a clean ground state of the leftmost trap, which became more realisitic in recent years [122–125]. It is therefore interesting to study how does the entanglement evolve in time within these protocols.

In the following section I will study the dynamics of the two-particle entanglement in the three SAP processes outlined in this chapter: two-particle transport, NOON-state preparation and particle separation [95]. As all these protocols are based on controlled transitions between three degenerate states, the entropy is not conserved, and therefore entanglement can be created in a controlled fashion. I will show that the entanglement in these SAP processes can be explained by contributions from two different origins, the interaction and the distribution of the particles between the traps.

2.6.1 von Neumann entropy as a measurement of entanglement

The von Neumann entropy of a quantum system is defined as

$$S(\rho) \equiv -\mathrm{tr}(\rho \log_2 \rho), \tag{2.26}$$

where ρ is the density matrix of the state. If density matrix ρ has eigenvalues λ_x, then the von Neumann entropy can be rewritten as

$$S(\rho) \equiv \sum_x \lambda_x \log_2 \lambda_x. \tag{2.27}$$

This formulation of the entropy can be interpreted as a measure of the state's impurity (how mixed it is). Thus, for pure states the von Neumann entropy is zero.

With a small modification the von Neumann entropy can be used as a measure of entanglement in a bipartite system

$$S(\rho_{\mathrm{rspdm}}) \equiv -\mathrm{tr}(\rho_{\mathrm{rspdm}} \log_2 \rho_{\mathrm{rspdm}}), \tag{2.28}$$

where ρ_{rspdm} is the *reduced single particle density matrix* (RSPDM) defined as

$$\rho_{\mathrm{rspdm}}(x, x', t) = \int_{-\infty}^{\infty} \Psi^*(x, x_2, t)\Psi(x', x_2, t)\mathrm{d}x_2, \tag{2.29}$$

and where $\Psi(x_1, x_2, t)$ is the two-particle wavefunction. Since all SAP processes we consider start from a well-defined pure state and the time evolution is unitary, the total two-particle state remains pure at all times t, and all entropy of the RSPDM has to come from the entanglement between the particles. This fact makes the von Neumann entropy of the RSPDM a good measure of two-particle entanglement[126–130] for pure states even in the case of indistinguishable particles[131]. Mixed states, however, require different approaches for entanglement measures[132–135].

2.6.2 Transport

The first case I study is SAP transport for a pair of particles, discussed in section 2.3, and below I will recap the main points of this process.

Starting from the state with both particles in the left trap, I numerically simulate the SAP sequence of the trap movements. I then calculate the fidelity of the process with the occupation of the desired state $|0\ 0\ 2\rangle$. These fidelities are shown in Fig.

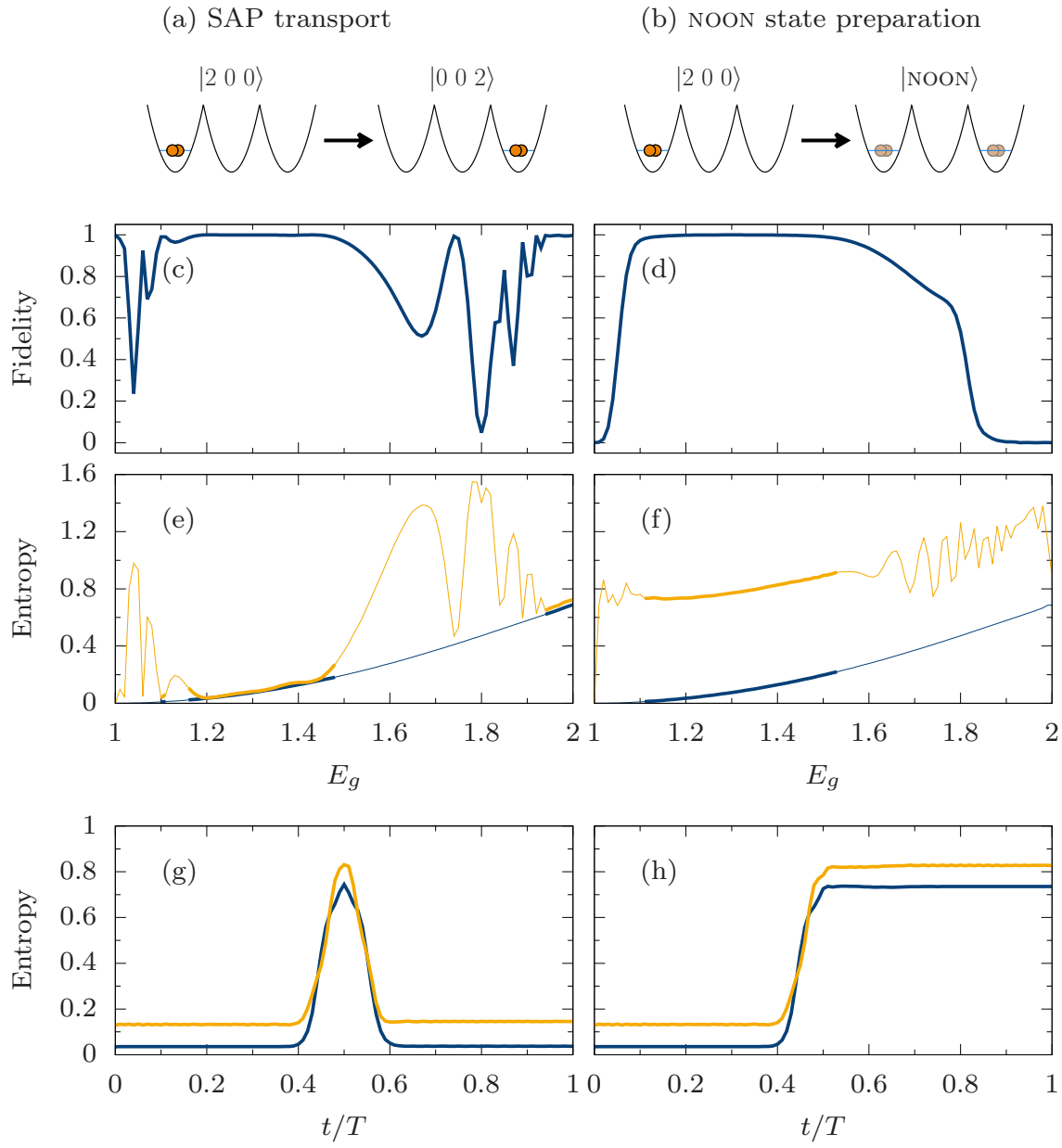

Figure 2.15: (a) Sketch of the SAP transport process. (b) Sketch of the NOON state generation process. (c-d) Fidelity of the transport/NOON generation as a function of the interaction energy E_g. (e-f) von Neumann entropy at the start (blue) and end (orange) of the transport/NOON generation process as a function of E_g. Thicker data points represent parameter values where the fidelity is above 98%. (g-h) Time evolution of the von Neumann entropy during transport/NOON generation for $E_g = 1.2$ (blue) and $E_g = 1.4$ (orange).

2.15(c) as a function of the interaction energy. The dark state only exists if the SAP triplet is sufficiently isolated from the rest of the spectrum [1], which leads to lower fidelities of the transport process for the interaction energies outside of the range $1.1 \leq E_g \leq 1.5$. The non-interacting case and the Tonks–Girardeau limit are the exceptions. In the non-interacting case the transport of the two atoms becomes independent, and in the Tonks–Girardeau limit, due to Bose-Fermi mapping theorem, the SAP process can be decomposed into two independent single particle processes, one for each of the particles.

The values of the von Neumann entropy of the initial and final states over the full range of interaction energy are shown in Fig. 2.15(e). Since we are interested in entropy (and hence entanglement) gains of the successfull process, we will only consider the range of interaction energies which results in high fidelity SAP processes. These values of the entropy for interaction energies in this range are shown in Fig. 2.15 (e) as a thicker curve. Unsurprisingly, the entropy of initial state increases with interaction strength [129], and in case of high-fidelity transport, the entropy is the same for the initial and the final states. This fact is easily understood considering that the two states $|2\ 0\ 0\rangle$ and $|0\ 0\ 2\rangle$ are mirror images of each other.

Now let us look at the dynamics of the entropy during the SAP transport process (see Fig. 2.15(g)). We can see an increase and decrease of entropy around the time when all traps are strongly coupled, and the systems is in the superposition of the two degenerate states $|2\ 0\ 0\rangle$ and $|0\ 0\ 2\rangle$.

The maximal increase is exactly $\ln 2$ corresponding to a fully antisymmetric superposition with the mixing angle $\pi/4$, an instantaneous NOON state. If the subsequent separation of the traps proceeds in a fully symmetric fashion, the NOON state would persist until the end of the process. This is the next case we study.

2.6.3 NOON state preparation

The fidelity of the process of creation of a NOON state is shown in Fig. 2.15(d) for the whole range of repulsive interactions. As follows from Figs. 2.15(c) and (d), the NOON state process results in high fidelity in the similar range of interactons which leave the SAP triplet isolated [1], but not in either the non-interacting case or the Tonks–Girardeau limit. The reason for this is that no entanglement between the two particles can be generated due to their dynamics being fully independent.

Unlike transport, the final state is now a superposition between the states $|2\ 0\ 0\rangle$ and $|0\ 0\ 2\rangle$, and the final entropy increases in comparison to the entropy of the initial state (see Fig. 2.15(f) and (h)), resulting in entanglement gain. This increase does not depend on the interaction strength, and only depends on the distribution of the particles between the different traps. The density matrix of the final state corresponds to the antisymmetric superposition of the states $|2\ 0\ 0\rangle$ and $|0\ 0\ 2\rangle$, and the entropy of the distribution among the traps thus can be calculated as $S_{\text{dist}} = -2\left(\frac{1}{2}\ln\frac{1}{2}\right) \simeq 0.69$.

2.6.4 Particle separation

Finally, I will study the particle separation SAP process discussed in section 2.4 [103]. As shown in section 2.4 and Fig. 2.16(b), the SAP triplet of the three Fock states

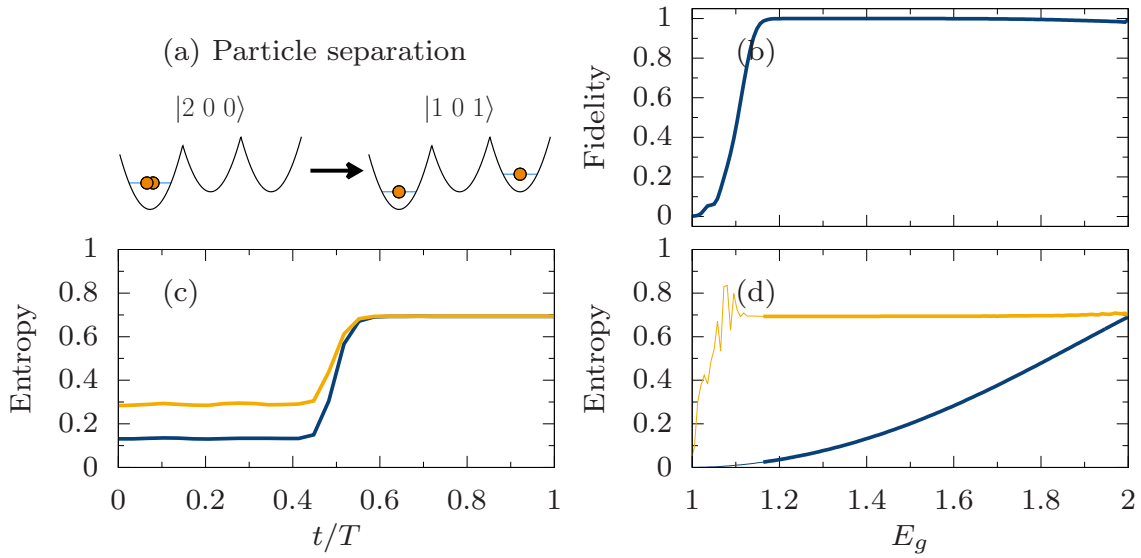

Figure 2.16: (a) Sketch of the particle separation process. (b) Fidelity of the scheme as a function of the interaction energy E_g. (c) Time evolution of the von Neumann entropy during the particle separation process for $E_g = 1.4$ (blue) and $E_g = 1.6$ (orange). (d) von Neumann entropy at the start (blue) and end (orange) of the separation process as a function of E_g. Thicker data points represent those values where the fidelity is above 98%. Small oscillation of the entropy outside of the high-fidelity region are due to the final state being very sensitive to the total time of the process.

$|2\ 0\ 0\rangle$, $|1\ 1\ 0\rangle$ and $|1\ 0\ 1\rangle$ remains isolated for almost the whole range of repulsive interaction, resulting in a high separation fidelity.

The entropy dynamics during this process for $E_g = 1.4$ and $E_g = 1.6$ are shown in Fig. 2.16(c). As the system follows the dark state, the entropy increases from its initial value until it reaches $S(|1\ 0\ 1\rangle) \approx 0.69$, which corresponds to the entanglement purely due to the distribution of two indistinguishable particles between the wells. The contribution of the interaction to the entanglement has vanished as the two particles are now separated into different wells [130]. In Fig. 2.16 (d) one can see that the final entropy of the $|1\ 0\ 1\rangle$ state is indeed independent of the interaction strength. Note that the final value of the entropy is the same as the entropy increase in the case of the NOON state preparation described above. The von Neumann entropy associated with a state where atoms are in different traps can be calculated by writing the state in the atomic basis as $|101\rangle = \frac{1}{\sqrt{2}}(|L\rangle_1|R\rangle_2 + |R\rangle_1|L\rangle_2)$, which results in a reduced density matrix for each atom $\rho_1 = \frac{1}{2}(|L\rangle\langle L| + |R\rangle\langle R|)$. As ρ_1 is a diagonal matrix, the von Neumann entropy is given by $S = -\frac{1}{2}\ln\frac{1}{2} - \frac{1}{2}\ln\frac{1}{2} = \ln 2$.

Analogously, the NOON state $|\text{NOON}\rangle = \frac{1}{\sqrt{2}}(|L\rangle_1|L\rangle_2 - |R\rangle_1|R\rangle_2)$, results in the same reduced density matrix, and thus also has a von Neumann entropy of $\ln 2$.

2.7 Conclusion

In this chapter I have reviewed the concept of spatial adiabatic passage and proposed a protocol that allows to divide a sample of interacting particles in a controlled way. The technique is based on engineering a quasi-three level system by raising or lowering the energies of some of the traps and allowing for an adiabatic transition between initial and target states. I have explicitly examined the cases $|2\ 0\ 0\rangle \rightarrow |1\ 0\ 1\rangle$ for a two-particle system and $|3\ 0\ 0\rangle \rightarrow |2\ 0\ 1\rangle$ and $|3\ 0\ 0\rangle \rightarrow |1\ 0\ 2\rangle$ for a three-particle system and shown that the SAP protocol results in high-fidelities over large ranges of interaction energies. The regions where the protocol fails correspond to level crossings present in the spectrum of the Bose–Hubbard model.

I have also shown that this protocol is realistic and robust against experimental uncertainties by examining a setting where two ^{87}Rb atoms were trapped in a radio-frequency trap setup. Using experimentally realistic parameters, the same high fidelities were obtained as for the idealised system, showing that quantum engineering techniques based on spatial adiabatic passage are also useful for interacting particle systems. The protocol we proposed is independent of the number of initial particles and can therefore be used in systems with large initial particle numbers.

I have also investigated the entropy dynamics of the SAP protocols and shown that the total entropy in the SAP processes can be attributed to contributions from two sources: one due the interaction between the atoms and one due to the distribution of the atoms between the traps. States with both atoms in the same trap, i.e., $|2\ 0\ 0\rangle$, have a von Neumann entropy which increases with the interaction $S_{\mathrm{int}}(E_g)$, ranging from zero in the non-interacting case (where the wavefunction is separable), to $\ln 2$ in the Tonks–Girardeau limit.

On the other hand, states such as $|101\rangle$ are unaffected by the interaction, but have a constant von Neumann entropy of $S_{\mathrm{dist}} = \ln 2$, which comes from the distribution of the particles between the traps. The NOON states have both contributions, as the atoms occupy states where they interact, while they are in a superposition occupying different sites, $S_{\mathrm{NOON}} = S_{\mathrm{int}}(E_g) + S_{\mathrm{dist}}$.

A summary of the entanglement of the SAP processes I have studied is shown in Fig. 2.17. All processes start in state $|2\ 0\ 0\rangle$, and thus with an entropy $S_{\mathrm{int}}(E_g)$.

Even though the fundamental processes identified above can be extended to systems with multiple particles, their study is problematic due to numerical intractability. For a separation process with an initial cloud of N particles in the left trap $|N\ 0\ 0\rangle$ as described in Sec. 2.4.3, a maximum value of the entropy $\ln 2$ is achieved when the cloud is evenly split, $|N/2\ 0\ N/2\rangle$, for N even, or split into $|\frac{N+1}{2}\ 0\ \frac{N-1}{2}\rangle$ for N odd. A NOON state $(|N\ 0\ 0\rangle - |0\ 0\ N\rangle)/\sqrt{2}$, will also have an entropy of $\ln 2$. If processes are designed that lead to a distribution of the atoms over more than two traps, for example, by sequential separation of one particle into each trap, such as $|1\ 1\ 1\ 1\ \ldots\rangle$, or by sequentially following the NOON state preparation protocol, such as $(|N\ 0\ 0\ 0\ \ldots\rangle + |0\ N\ 0\ 0\ \ldots\rangle + |0\ 0\ N\ 0\ \ldots\rangle + \ldots)/\sqrt{N}$, the entropy would be $\ln N$, plus in the second case also the interaction entropy.

These results have been published in Physical Review A [103] and Few-Body Systems [95].

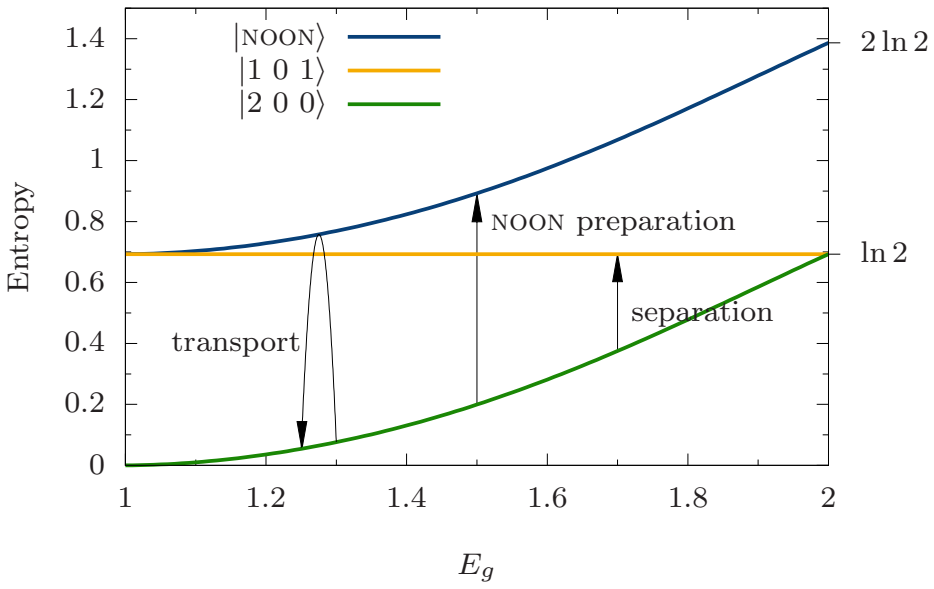

Figure 2.17: Von Neumann entropy of states $|200\rangle$ (green), $|101\rangle$ (orange), and $|\text{NOON}\rangle$ (blue) as a function of the interaction energy E_g. The arrows represent the changes in entropy during the spatial adiabatic passage processes.

Chapter 3

The coordinate Bethe ansatz

In the previous chapter I proposed a theoretical tool for controlling the state of a few-body system for which the knowledge of the energy spectrum and the eigenstates is essential. More complicated systems such as systems with larger number of particles are in general too big for numeric simulations, but important insight in their behaviour can be gained from analytical treatment.

In this chapter I will introduce the coordinate Bethe ansatz as a mathematical tool for exact analysis of some one-dimensional systems. I will discuss its uses and limitations, and apply it to solve an example problem of a 1D Bose gas in a box. This simple yet relevant example is going to form the basis for my analysis of more complicated systems such as a system with point-like barriers of arbitrary heights and positions inside a box (AFKP). I will discuss the breakdown of integrability in the case of multiple interacting particles, and derive a general form of the solution for the single particle case with an arbitrary number of barriers with positions and heights as the parameters of the systems.

I will also consider a modification of the system to include two distinguishable particles with detuned effective barriers.

3.1 Introduction to the coordinate Bethe ansatz

The coordinate Bethe ansatz is one of the essential tools of mathematical physics and has been extensively used in exact studies of one-dimensional systems. It was first introduced by Hans Bethe in 1931 to find exact solution to the one-dimensional antiferromagnetic Heisenberg model[136]. Since then it was used to obtain solutions of various one-dimensional models. Lieb and Liniger found the solution for the many-body system of bosons in a ring[46, 137], with Sutherland[138, 139] and Flicker[140] later extending it to multicomponent systems. The interacting Bose gas in a box was first analyzed by Gaudin[141], and later reexamined by Oelkers *et al.*[142, 143]. More recently, the Bethe ansatz was used to study the behaviour of impurities and thermodynamics in the multicomponent Lieb–Liniger model[144, 145].

The coordinate Bethe ansatz was also successful in tackling more complicated boundary conditions, such as Bose gas on a half-line[146, 147] and in a box with a finite delta barrier in the middle[148]. In more general terms, classes of boundary con-

ditions which preserve integrability for the Bethe ansatz were intensively discussed by the community, see for example [149, 150].

The Bethe ansatz technique relies on the fact that the system has only point-like interactions, and that far away from each other the particles behave as if they were free. One can then represent the total N-body wave function as a superposition of plane waves with momenta which are ordered according to different permutations $P = (p_1, p_2, \ldots, p_N)$ in each region of the wave function with the particles ordered according to $Q = (q_1, q_2, \ldots, q_N)$ as $x_{q_1} \leq x_{q_2} \leq \cdots \leq x_{q_N}$[28, 151]

$$\Psi(x_1, \ldots, x_N) = \sum_{P=(p_1,\ldots,p_N)} \sum_{Q=(q_1,\ldots,q_N)} \mathcal{A}_{P,Q}\, \mathrm{e}^{\,\mathrm{i}\sum_{j=1}^{N} k_{p_j} x_{q_j}} \Theta(\mathcal{T}_Q), \tag{3.1}$$

where $\Theta(\mathcal{T}_Q) = \prod_{j=1}^{N} \theta(x_{q_j} - x_{q_{j-1}})$ with $\theta(x)$ being the Heaviside Theta function.

Another necessary condition for the solution to exist is the non-diffractiveness of the system[28]. This means that all three-body scattering events can be decomposed into a sequence of two-body scattering events, and that their order does not matter. In mathematical terms this condition takes form of the Yang–Baxter relations[152]. The two-body scattering events can then only result in particles completely passing through each other, thus exchanging their coordinates, or bouncing off each other, thus exchanging their momenta. Both these outcomes correspond to particles acquiring a phase. In terms of the ansatz, this reasoning translates into expressions for various ratios between the coefficients $\mathcal{A}_{P,Q}$, for example,

$$\frac{\mathcal{A}_{\tilde{P},Q}}{\mathcal{A}_{P,Q}} = \mathrm{e}^{\mathrm{i}\theta(k_{p_1},\ldots,k_{p_N})} \tag{3.2}$$

with $\tilde{P} = (p_1, \ldots, p_j, p_{j-1}, \ldots, p_N)$ in case of a momentum exchange.

These expressions for the ratios combined with the boundary conditions generate a system of N transcendental equations for the unknown quasi-momenta $k_1, \ldots, k_N$ called *the Bethe equations*. In general, due to their transcendental nature, the Bethe equations have to be solved numerically.

The set of the expressions for the ratios between the coefficients can also be transformed into recursive expressions for all coefficients $\mathcal{A}_{P,Q}$ in terms of one of them, which can be fixed with the normalization condition. This allows for the determination of the full many-body wave function.

In next section I will review the use of the Bethe ansatz to solve the model of a Bose gas confined in a box as a basic model for a finite many-body system.

3.2 The Lieb–Liniger model in a box

Consider N distinguishable particles trapped in a one-dimensional infinite well of length L. If the particles have point-like interactions of strength c, then the Hamiltonian of this system reads

$$\hat{H} = -\frac{\hbar^2}{2m} \sum_{j=1}^{N} \frac{\partial^2}{\partial x_j^2} + c \sum_{j>l}^{N} \delta(x_j - x_l). \tag{3.3}$$

The wavefunction also has to go to zero at the edges of the infinite well, which translates into the boundary conditions

$$\Psi\left(x_j = \pm\frac{L}{2}\right) = 0,\ j = 1, \ldots, N. \tag{3.4}$$

Due to finiteness of the system, we have to take into account reflection events. To do that we will introduce additional summation parameters $\vec{\epsilon} = (\epsilon_1, \epsilon_2, \ldots, \epsilon_N)$ with $\epsilon_j = \{\pm 1\}$ for all $j = 1, \ldots, N$, which allows to explicitly include plane waves with inverted momenta. The modified Bethe ansatz wave function then becomes

$$\Psi(x_1, \ldots, x_N) = \sum_Q \sum_P \sum_{\vec{\epsilon}} \mathcal{A}^Q_{\vec{\epsilon}P} \mathrm{e}^{\,\mathrm{i}\sum\limits_{j=1}^{N} \epsilon_j k_{p_j} x_{q_j}} \Theta(\mathcal{T}_Q). \tag{3.5}$$

Here the sums over $P = (p_1, p_2, \ldots, p_N)$ and $Q = (q_1, q_2, \ldots, q_N)$ are over all permutations of the momenta and coordinates indices, respectively, and $\mathcal{A}^Q_{\vec{\epsilon}P} \in \mathbb{C}$ are the corresponding coefficients.

As the interaction terms in the Hamiltonian (3.3) are point-like, they can be replaced by the boundary condition for the wavefunction of the form

$$\Psi\Big|_{x_{q_j} - x_{q_{j-1}} = 0^+} = \Psi\Big|_{x_{q_j} - x_{q_{j-1}} = 0^-}, \tag{3.6}$$

and similar for the derivative of the wavefunction

$$\left(\frac{\partial}{\partial x_{q_j}} - \frac{\partial}{\partial x_{q_{j-1}}}\right) \Psi\Big|_{x_{q_j} - x_{q_{j-1}} = 0^+} - \left(\frac{\partial}{\partial x_{q_j}} - \frac{\partial}{\partial x_{q_{j-1}}}\right) \Psi\Big|_{x_{q_j} - x_{q_{j-1}} = 0^-} = \frac{2mc}{\hbar^2} \Psi\Big|_{x_{q_j} = x_{q_{j-1}}}, \ \forall Q. \tag{3.7}$$

Below I will consider the two-particle case for clarity. The ansatz wavefunction can then be written as

$$\Psi(x, y) = \sum_P \sum_{\vec{\epsilon}} \left(\mathcal{A}_{\vec{\epsilon}P} \theta(x < y) + \mathcal{B}_{\vec{\epsilon}P} \theta(y \leq x)\right) \mathrm{e}^{\mathrm{i}(\epsilon_x k_{p_1} x + \epsilon_y k_{p_2} y)}, \tag{3.8}$$

where the two particles have coordinates x and y, and $\vec{\epsilon} = (\epsilon_x, \epsilon_y)$. The boundary conditions from the walls of the box become

$$\Psi\left(x = \pm\frac{L}{2}, y\right) = \Psi\left(x, y = \pm\frac{L}{2}\right) = 0, \tag{3.9}$$

and the interaction term can be replaced by the wavefunction continuity condition

$$\Psi|_{x-y=0^+} = \Psi|_{x-y=0^-}, \tag{3.10}$$

and the scattering condition

$$\left(\frac{\partial}{\partial x} - \frac{\partial}{\partial y}\right) \Psi|_{x-y=0^+} - \left(\frac{\partial}{\partial x} - \frac{\partial}{\partial y}\right) \Psi|_{x-y=0^-} = \frac{2mc}{\hbar^2} \Psi|_{x=y}. \tag{3.11}$$

After applying the left hard wall condition to the ansatz wavefunction, we get

$$\sum_P \sum_{\vec{\epsilon}} \left(\mathcal{A}_{\vec{\epsilon}P}\theta(x<y) + \mathcal{B}_{\vec{\epsilon}P}\theta(y\leq x)\right) \mathrm{e}^{\mathrm{i}(\epsilon_x k_{p_1}\left(-\frac{L}{2}\right)+\epsilon_y k_{p_2} y)} = 0, \tag{3.12}$$

$$\sum_P \sum_{\vec{\epsilon}} \left(\mathcal{A}_{\vec{\epsilon}P}\theta(x<y) + \mathcal{B}_{\vec{\epsilon}P}\theta(y\leq x)\right) \mathrm{e}^{\mathrm{i}(\epsilon_x k_{p_1} x+\epsilon_y k_{p_2}\left(-\frac{L}{2}\right))} = 0. \tag{3.13}$$

Considering that the particles at x and y can only reflect from the left barriers if $x<y$ or $y<x$, we can simplify the previous equations to

$$\sum_P \sum_{\vec{\epsilon}} \mathcal{A}_{\vec{\epsilon}P} \mathrm{e}^{\mathrm{i}\epsilon_x k_{p_1}\left(-\frac{L}{2}\right)} = 0, \tag{3.14}$$

$$\sum_P \sum_{\vec{\epsilon}} \mathcal{B}_{\vec{\epsilon}P} \mathrm{e}^{\mathrm{i}\epsilon_y k_{p_2}\left(-\frac{L}{2}\right)} = 0. \tag{3.15}$$

Furthermore, all terms for different values of P have to go to zero independently, giving

$$\mathcal{A}_{\epsilon_x k_{p_1},\epsilon_y k_{p_2}} \mathrm{e}^{-\mathrm{i}\epsilon_x k_{p_1}\frac{L}{2}} + \mathcal{A}_{-\epsilon_x k_{p_1},\epsilon_y k_{p_2}} \mathrm{e}^{\mathrm{i}\epsilon_x k_{p_1}\frac{L}{2}} = 0, \tag{3.16}$$

$$\mathcal{B}_{\epsilon_x k_{p_1},\epsilon_y k_{p_2}} \mathrm{e}^{-\mathrm{i}\epsilon_y k_{p_2}\frac{L}{2}} + \mathcal{B}_{\epsilon_x k_{p_1},-\epsilon_y k_{p_2}} \mathrm{e}^{\mathrm{i}\epsilon_y k_{p_2}\frac{L}{2}} = 0, \tag{3.17}$$

and the conditions on the coefficients for the reflection against the left wall then become

$$\overleftarrow{\mathcal{R}}^{x\mathcal{A}}_{\vec{\epsilon}P} = \frac{\mathcal{A}_{-\epsilon_x k_{p_1},\epsilon_y k_{p_2}}}{\mathcal{A}_{\epsilon_x k_{p_1},\epsilon_y k_{p_2}}} = -\mathrm{e}^{-\mathrm{i}\epsilon_x k_{p_1} L}, \tag{3.18}$$

$$\overleftarrow{\mathcal{R}}^{y\mathcal{B}}_{\vec{\epsilon}P} = \frac{\mathcal{B}_{\epsilon_x k_{p_1},-\epsilon_y k_{p_2}}}{\mathcal{B}_{\epsilon_x k_{p_1},\epsilon_y k_{p_2}}} = -\mathrm{e}^{-\mathrm{i}\epsilon_y k_{p_2} L}, \tag{3.19}$$

and analogously, the reflection against the right wall gives

$$\overrightarrow{\mathcal{R}}^{x\mathcal{B}}_{\vec{\epsilon}P} = \frac{\mathcal{B}_{-\epsilon_x k_{p_1},\epsilon_y k_{p_2}}}{\mathcal{B}_{\epsilon_x k_{p_1},\epsilon_y k_{p_2}}} = -\mathrm{e}^{\mathrm{i}\epsilon_x k_{p_1} L}, \tag{3.20}$$

$$\overrightarrow{\mathcal{R}}^{y\mathcal{A}}_{\vec{\epsilon}P} = \frac{\mathcal{A}_{\epsilon_x k_{p_1},-\epsilon_y k_{p_2}}}{\mathcal{A}_{\epsilon_x k_{p_1},\epsilon_y k_{p_2}}} = -\mathrm{e}^{\mathrm{i}\epsilon_y k_{p_2} L}. \tag{3.21}$$

Let us now substitute the ansatz in Eq. (3.8) into the continuity condition in Eq. (3.10). This gives

$$\sum_{\vec{\epsilon}} \sum_P \mathcal{B}_{\vec{\epsilon}P} \mathrm{e}^{\mathrm{i}x(\epsilon_x k_{p_1}+\epsilon_y k_{p_2})} = \sum_{\vec{\epsilon}} \sum_P \mathcal{A}_{\vec{\epsilon}P} \mathrm{e}^{\mathrm{i}x(\epsilon_x k_{p_1}+\epsilon_y k_{p_2})}. \tag{3.22}$$

The arguments of the exponents are the same if the momenta of the particles are exchanged and are independent in any other arrangement, which gives a relation between the four coefficients of the form

$$\mathcal{B}_{\vec{\epsilon}P} + \mathcal{B}_{\overleftrightarrow{\epsilon P}} = \mathcal{A}_{\vec{\epsilon}P} + \mathcal{A}_{\overleftrightarrow{\epsilon P}}. \tag{3.23}$$

Here $\vec{\epsilon}P = (\epsilon_x k_{p_1}, \epsilon_y k_{p_2})$ and $\overleftrightarrow{\epsilon P} = (\epsilon_y k_{p_2}, \epsilon_x k_{p_1})$. We can derive the scattering conditions on the coefficients after substituting the ansatz (3.8) into the scattering condition (3.11) and taking the terms to be independent

$$\mathrm{i}(\epsilon_x k_{p_1} - \epsilon_y k_{p_2}) \left(\mathcal{B}_{\vec{\epsilon}P} - \mathcal{B}_{\overleftrightarrow{\epsilon P}} - \mathcal{A}_{\vec{\epsilon}P} + \mathcal{A}_{\overleftrightarrow{\epsilon P}}\right) = \frac{2mc}{\hbar^2} \left(\mathcal{A}_{\vec{\epsilon}P} + \mathcal{A}_{\overleftrightarrow{\epsilon P}}\right). \tag{3.24}$$

After substituting the expression for $\mathcal{B}_{\overleftrightarrow{\epsilon P}}$ from Eq. (3.23) into the previous equation, we get

$$\mathrm{i}(\epsilon_x k_{p_1} - \epsilon_y k_{p_2})\left(\mathcal{B}_{\vec{\epsilon}P} - \mathcal{A}_{\vec{\epsilon}P}\right) = \frac{mc}{\hbar^2}\left(\mathcal{A}_{\vec{\epsilon}P} + \mathcal{A}_{\overleftrightarrow{\epsilon P}}\right). \tag{3.25}$$

The scattering relations for the two scattering outcomes, the particles exchanging their positions or momenta, are defined as

$$\mathcal{S}^{xy}_{\vec{\epsilon}P} = \frac{\mathcal{B}_{\vec{\epsilon}P}}{\mathcal{A}_{\vec{\epsilon}P}}, \tag{3.26}$$

$$\mathcal{S}^{\mathcal{A}}_{\vec{\epsilon}P} = \frac{\mathcal{A}_{\overleftrightarrow{\epsilon P}}}{\mathcal{A}_{\vec{\epsilon}P}}, \tag{3.27}$$

and can be used to rewrite Eq. (3.25) as

$$\mathrm{i}(\epsilon_x k_{p_1} - \epsilon_y k_{p_2})\left(\mathcal{S}^{xy}_{\vec{\epsilon}P} - 1\right) = \frac{mc}{\hbar^2}\left(1 + \mathcal{S}^{\mathcal{A}}_{\vec{\epsilon}P}\right). \tag{3.28}$$

Finally, we can derive the relation between the two scattering outcomes as

$$\mathcal{S}^{xy}_{\vec{\epsilon}P} = 1 - \mathrm{i}\frac{mc}{\hbar^2(\epsilon_x k_{p_1} - \epsilon_y k_{p_2})}\left(1 + \mathcal{S}^{\mathcal{A}}_{\vec{\epsilon}P}\right), \ \forall \vec{\epsilon}P. \tag{3.29}$$

This relation has to hold for all $\vec{\epsilon}P$, including

$$\mathcal{S}^{xy}_{-\epsilon_x k_{p_1}, \epsilon_y k_{p_2}} = 1 + \mathrm{i}\frac{mc}{\hbar^2(\epsilon_x k_{p_1} + \epsilon_y k_{p_2})}\left(1 + \mathcal{S}^{\mathcal{A}}_{-\epsilon_x k_{p_1}, \epsilon_y k_{p_2}}\right). \tag{3.30}$$

By remembering that

$$\mathcal{S}^{\mathcal{A}}_{-\epsilon_x k_{p_1}, \epsilon_y k_{p_2}} = \frac{\mathcal{A}_{\epsilon_y k_{p_2}, -\epsilon_x k_{p_1}}}{\mathcal{A}_{-\epsilon_x k_{p_1}, \epsilon_y k_{p_2}}}, \tag{3.31}$$

and taking into account equations (3.21) and (3.18), we get

$$\mathcal{S}^{xy}_{-\epsilon_x k_{p_1}, \epsilon_y k_{p_2}} = 1 + \mathrm{i}\frac{mc}{\hbar^2(\epsilon_x k_{p_1} + \epsilon_y k_{p_2})}\left(1 + \frac{\overrightarrow{\mathcal{R}}^{y\mathcal{A}}_{\overleftrightarrow{\epsilon P}}}{\overleftarrow{\mathcal{R}}^{x\mathcal{A}}_{\vec{\epsilon}P}}\mathcal{S}^{\mathcal{A}}_{\vec{\epsilon}P}\right) \tag{3.32}$$

On the other hand, from Eq. (3.18) and Eq. (3.20) we get

$$\mathcal{S}^{xy}_{-\epsilon_x k_{p_1}, \epsilon_y k_{p_2}} = \frac{\mathcal{B}_{-\epsilon_x k_{p_1}, \epsilon_y k_{p_2}}}{\mathcal{A}_{-\epsilon_x k_{p_1}, \epsilon_y k_{p_2}}} = \frac{\overrightarrow{\mathcal{R}}^{x\mathcal{B}}_{\vec{\epsilon}P}}{\overleftarrow{\mathcal{R}}^{x\mathcal{A}}_{\vec{\epsilon}P}} \times \frac{\mathcal{B}_{\vec{\epsilon}P}}{\mathcal{A}_{\vec{\epsilon}P}} = \frac{\overrightarrow{\mathcal{R}}^{x\mathcal{B}}_{\vec{\epsilon}P}}{\overleftarrow{\mathcal{R}}^{x\mathcal{A}}_{\vec{\epsilon}P}} \times \mathcal{S}^{xy}_{\vec{\epsilon}P}. \tag{3.33}$$

These two forms of $\mathcal{S}^{xy}_{-\epsilon_x k_{p_1}, \epsilon_y k_{p_2}}$ have to be equivalent, giving an expression for $\mathcal{S}^{\mathcal{A}}_{\vec{\epsilon}P}$ of the form

$$\mathcal{S}^{\mathcal{A}}_{\vec{\epsilon}P} = \frac{\overrightarrow{\mathcal{R}}^{x\mathcal{B}}_{\vec{\epsilon}P}\left(-\mathrm{i}\frac{\hbar^2}{mc}(k^2_{p_1} - k^2_{p_2}) - (\epsilon_x k_{p_1} + \epsilon_y k_{p_2})\right) - \overleftarrow{\mathcal{R}}^{x\mathcal{A}}_{\vec{\epsilon}P}\left(-\mathrm{i}\frac{\hbar^2}{mc}(k^2_{p_1} - k^2_{p_2}) + (\epsilon_x k_{p_1} - \epsilon_y k_{p_2})\right)}{\overrightarrow{\mathcal{R}}^{y\mathcal{A}}_{\overleftrightarrow{\epsilon P}}(\epsilon_x k_{p_1} - \epsilon_y k_{p_2}) + \overrightarrow{\mathcal{R}}^{x\mathcal{B}}_{\vec{\epsilon}P}(\epsilon_x k_{p_1} + \epsilon_y k_{p_2})}, \forall \vec{\epsilon}P. \tag{3.34}$$

Now we have all ingredients to construct the Bethe equations for this system. In order to do that, we need to consider all possible ways of inverting a particle's momentum.

Consider a particle being on the right hand side of the other particle. Then its momentum can be inverted by reflecting from the right wall, or by scattering with the other particle and then scattering back after reflecting from the left wall. These two ways of inverting the momentum have to be equivalent, giving the first Bethe equation

$$\overrightarrow{\mathcal{R}}^{y\mathcal{A}}_{\vec{\epsilon}P} = \frac{\mathcal{S}^{xy}_{\vec{\epsilon}P}}{\mathcal{S}^{xy}_{\epsilon_x k_{p_1}, -\epsilon_y k_{p_2}}} \overleftarrow{\mathcal{R}}^{y\mathcal{B}}_{\vec{\epsilon}P}. \tag{3.35}$$

Another Bethe equation can be obtained by considering another outcome of the scattering between two particles: they exchange momentum, then the second particle gets reflected from the right wall, and lastly, it exchanges the inverted momentum again with the first particle. This gives

$$\overrightarrow{\mathcal{R}}^{y\mathcal{A}}_{\vec{\epsilon}P} = \frac{\mathcal{S}^{\mathcal{A}}_{\vec{\epsilon}P}}{\mathcal{S}^{\mathcal{A}}_{\epsilon_x k_{p_1}, -\epsilon_y k_{p_2}}} \overleftarrow{\mathcal{R}}^{x\mathcal{A}}_{\overleftrightarrow{\epsilon P}}. \tag{3.36}$$

The analogous equations for the second particle x are satisfied trivially, so we end up with two Bethe equations for two quasi-momenta of the particles. The energies of the corresponding eigenstates are then given by

$$E(k_1, k_2) = \frac{\hbar^2}{2m}(k_1^2 + k_2^2). \tag{3.37}$$

An example of the solutions of the Bethe equations is shown in Fig. 3.1. The allowed quasi-momenta are given by the intersections of the two curves. The lines $k_1 = 0$, $k_2 = 0$, $k_1 = k_2$ and $k_1 = -k_2$ do not correspond to physical solutions. The $k_1 = 0$ and $k_2 = 0$ cases violate the Heisenberg uncertainty principle, while $k_1 = k_2$ and $k_1 = -k_2$ describe bound pairs which can never scatter and are not captured correctly by the ansatz if $c \neq 0$.

It is easy to see that if k_1 and k_2 are the solutions of the Bethe equations, then $\epsilon_1 k_1$ and $\epsilon_2 k_2$ are also the solutions with the same energy for any signs (ϵ_1, ϵ_2). This fact leads to a four-fold degeneracy of the eigenstates, as shown in Fig. 3.1.

From the continuity equations (3.23) and (3.27) and by defining

$$\mathcal{S}^{\mathcal{B}}_{\vec{\epsilon}P} = \frac{\mathcal{B}_{\overleftrightarrow{\epsilon P}}}{\mathcal{B}_{\vec{\epsilon}P}}, \tag{3.38}$$

we get another relation

$$\mathcal{B}_{\vec{\epsilon}P}\left(1 + \mathcal{S}^{\mathcal{B}}_{\vec{\epsilon}P}\right) = \mathcal{A}_{\vec{\epsilon}P}\left(1 + \mathcal{S}^{\mathcal{A}}_{\vec{\epsilon}P}\right). \tag{3.39}$$

This equation, together with Eq. (3.26), gives the expression for $\mathcal{S}^{\mathcal{B}}_{\vec{\epsilon}P}$

$$\mathcal{S}^{\mathcal{B}}_{\vec{\epsilon}P} = \frac{\mathcal{S}^{\mathcal{A}}_{\vec{\epsilon}P}\left(\epsilon_x k_{p_1} - \epsilon_y k_{p_2} + \mathrm{i}\frac{mc}{\hbar^2}\right) + \mathrm{i}\frac{mc}{\hbar^2}}{\left(\epsilon_x k_{p_1} - \epsilon_y k_{p_2} - \mathrm{i}\frac{mc}{\hbar^2}\right) - \mathrm{i}\frac{mc}{\hbar^2}\mathcal{S}^{\mathcal{A}}_{\vec{\epsilon}P}}, \ \forall \vec{\epsilon}P. \tag{3.40}$$

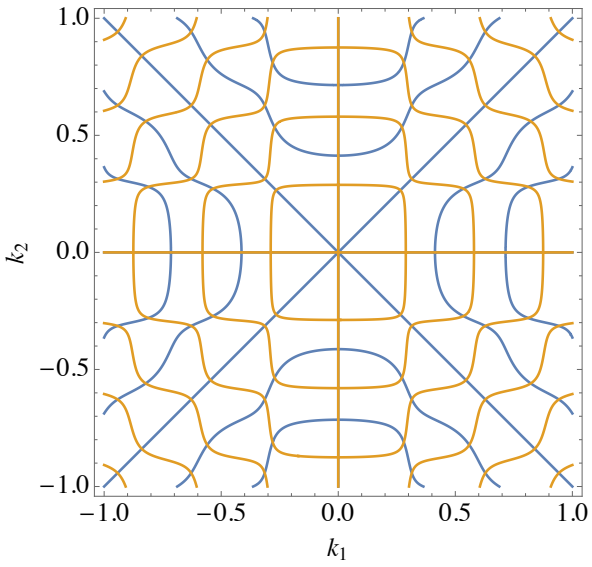

Figure 3.1: Plot of the curves given by the Bethe equations (3.35) and (3.36). The allowed values of quasi-momenta k_1 and k_2 are given by the intersection of the blue and the orange curves. It is easy to see a 4-fold degeneracy of the resulting eigenstates. The lines $k_1 = 0$, $k_2 = 0$, $k_1 = k_2$ and $k_1 = -k_2$ do not represent a physical solution. Here I use natural units $\hbar = m = 1$, the size of the box is $L = 10$ and $c = 1$.

Now we have all relations between the coefficients and we can finally express them as

$$\mathcal{A}_{-k_1,k_2} = \overleftarrow{\mathcal{R}}^{x\mathcal{A}}_{k_1,k_2}\mathcal{A}_0, \tag{3.41}$$
$$\mathcal{A}_{k_1,-k_2} = \overrightarrow{\mathcal{R}}^{y\mathcal{A}}_{k_1,k_2}\mathcal{A}_0, \tag{3.42}$$
$$\mathcal{A}_{-k_1,-k_2} = \overleftarrow{\mathcal{R}}^{x\mathcal{A}}_{k_1,-k_2}\overrightarrow{\mathcal{R}}^{y\mathcal{A}}_{k_1,k_2}\mathcal{A}_0, \tag{3.43}$$
$$\mathcal{A}_{k_2,k_1} = \mathcal{S}^{\mathcal{A}}_{k_1,k_2}\mathcal{A}_0, \tag{3.44}$$
$$\mathcal{A}_{-k_2,k_1} = \mathcal{S}^{\mathcal{A}}_{k_1,-k_2}\overrightarrow{\mathcal{R}}^{y\mathcal{A}}_{k_1,k_2}\mathcal{A}_0, \tag{3.45}$$
$$\mathcal{A}_{k_2,-k_1} = \mathcal{S}^{\mathcal{A}}_{-k_1,k_2}\overleftarrow{\mathcal{R}}^{x\mathcal{A}}_{k_1,k_2}\mathcal{A}_0, \tag{3.46}$$
$$\mathcal{A}_{-k_2,-k_1} = \mathcal{S}^{\mathcal{A}}_{-k_1,-k_2}\overrightarrow{\mathcal{R}}^{y\mathcal{A}}_{-k_1,k_2}\overleftarrow{\mathcal{R}}^{x\mathcal{A}}_{k_1,k_2}\mathcal{A}_0, \tag{3.47}$$

and

$$\mathcal{B}_{k_1,k_2} = \mathcal{S}^{xy}_{k_1,k_2}\mathcal{A}_0, \tag{3.48}$$
$$\mathcal{B}_{-k_1,k_2} = \overrightarrow{\mathcal{R}}^{x\mathcal{B}}_{k_1,k_2}\mathcal{S}^{xy}_{k_1,k_2}\mathcal{A}_0, \tag{3.49}$$
$$\mathcal{B}_{k_1,-k_2} = \overleftarrow{\mathcal{R}}^{y\mathcal{B}}_{k_1,k_2}\mathcal{S}^{xy}_{k_1,k_2}\mathcal{A}_0, \tag{3.50}$$
$$\mathcal{B}_{-k_1,-k_2} = \overrightarrow{\mathcal{R}}^{x\mathcal{B}}_{k_1,-k_2}\overleftarrow{\mathcal{R}}^{y\mathcal{B}}_{k_1,k_2}\mathcal{S}^{xy}_{k_1,k_2}\mathcal{A}_0, \tag{3.51}$$
$$\mathcal{B}_{k_2,k_1} = \mathcal{S}^{\mathcal{B}}_{k_1,k_2}\mathcal{S}^{xy}_{k_1,k_2}\mathcal{A}_0, \tag{3.52}$$
$$\mathcal{B}_{-k_2,k_1} = \mathcal{S}^{\mathcal{B}}_{k_1,-k_2}\overleftarrow{\mathcal{R}}^{y\mathcal{B}}_{k_1,k_2}\mathcal{S}^{xy}_{k_1,k_2}\mathcal{A}_0, \tag{3.53}$$
$$\mathcal{B}_{k_2,-k_1} = \mathcal{S}^{\mathcal{B}}_{-k_1,k_2}\overrightarrow{\mathcal{R}}^{x\mathcal{B}}_{k_1,k_2}\mathcal{S}^{xy}_{k_1,k_2}\mathcal{A}_0, \tag{3.54}$$
$$\mathcal{B}_{-k_2,-k_1} = \mathcal{S}^{\mathcal{B}}_{-k_1,-k_2}\overleftarrow{\mathcal{R}}^{y\mathcal{B}}_{-k_1,k_2}\overrightarrow{\mathcal{R}}^{x\mathcal{B}}_{k_1,k_2}\mathcal{S}^{xy}_{k_1,k_2}\mathcal{A}_0. \tag{3.55}$$

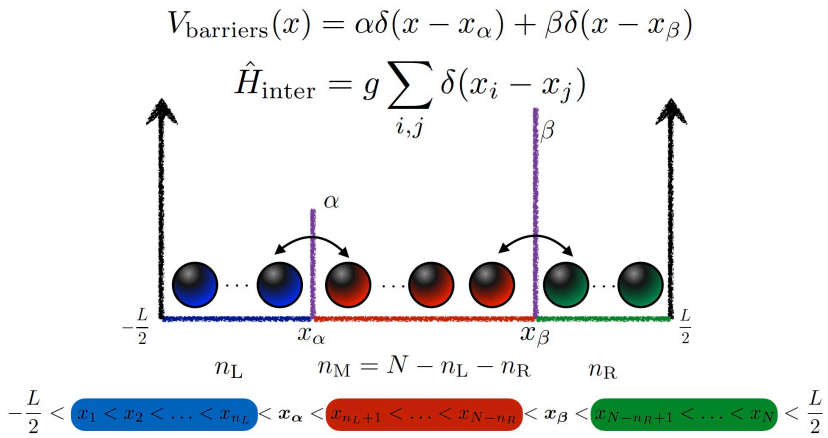

Figure 3.2: Schematic of the Bose gas in a box with three barriers. The two point-like barriers can be arbitrarily positioned and have arbitrary heights.
I only consider the ordering of the N particles where $x_1 < x_2 < \cdots < x_N$. All other permutations of particles can be obtained through the symmetry considerations due to statistics of the particles.

The remaining coefficient $\mathcal{A}_0$ can be fixed using the normalization condition

$$\int_{-\frac{L}{2}}^{\frac{L}{2}}\int \Psi(x,y)\mathrm{d}x\mathrm{d}y = 1. \tag{3.56}$$

With all these coefficients determined, the full wave function can therefore be straightforwardly reconstructed.

In conclusion, in this section I reviewed how the coordinate Bethe ansatz can be used to obtain the equations which define the allowed quasi-momenta as well as the expression for the eigenstates of a model Hamiltonian with two distinguishable particles in a box. In the next section I will discuss the use of the Bethe ansatz in order to obtain the solution of a modified system with one or more point-like barriers of arbitrary heights positioned within the box.

3.3 Multiple indistinguishable particles in a box with two barriers

To establish the underlying ideas and concepts of the AFKP model, I will first discuss the solution of the Bose gas trapped in an infinite square well with two arbitrarily positioned barriers of arbitrary heights (see Fig. 3.2). I will derive the Yang–Baxter relations for this model and prove that it is in general not solvable by the Bethe ansatz. I will also review the partially solvable special case studied by Liu and Zhang in [148].

The total Hamiltonian for the system with N particles is

$$\hat{H} = \sum_{j=1}^{N} \left(-\frac{\hbar^2}{2m}\frac{\partial^2}{\partial x_j^2} + \alpha\delta(x_j - x_\alpha) + \beta\delta(x_j - x_\beta) \right) + c \sum_{i<j=1}^{N} \delta(x_j - x_i). \tag{3.57}$$

Here the left (right) barrier is of height α (β) and has the position x_α (x_β), and the particle interaction has strength c. The two barriers in this system form three traps, and the wavefunction must go to zero at the walls of the box. As discussed in sec. 3.2, due to zero-range nature of the interaction and the potential barriers, the problem can be reduced to the free space Lieb–Liniger model

$$-\frac{\hbar^2}{2m}\sum_{j=1}^{N}\frac{\partial^2\Psi\left(x_1,...,x_N\right)}{\partial x_j^2} = E\Psi\left(x_1,...,x_N\right) \tag{3.58}$$

with boundary conditions which account for the scattering between the particles and between the particles and the barriers.

The scattering condition between particles in the same trap is given by [151]

$$\left(\frac{\partial}{\partial x_{j+1}} - \frac{\partial}{\partial x_j} - \frac{mc}{\hbar^2}\right)\Psi\left(x_1,...,x_N\right) = 0, \tag{3.59}$$

and the scattering of the particles with the α-barriers is captured by

$$\left(\frac{\partial}{\partial x_j}\bigg|_{x_j=x_\alpha+0} - \frac{\partial}{\partial x_j}\bigg|_{x_j=x_\alpha-0} - \frac{2m\alpha}{\hbar^2}\bigg|_{x_j=x_\alpha}\right)\Psi\left(x_1,...,x_N\right) = 0, \tag{3.60}$$

with the α-continuity condition

$$\Psi\left(x_1,...,x_N\right)\big|_{x_j=x_\alpha-0} = \Psi\left(x_1,...,x_N\right)\big|_{x_j=x_\alpha+0}\,. \tag{3.61}$$

Analagous conditions hold for the β-barrier,

$$\left(\frac{\partial}{\partial x_j}\bigg|_{x_j=x_\beta+0} - \frac{\partial}{\partial x_j}\bigg|_{x_j=x_\beta-0} - \frac{2m\beta}{\hbar^2}\bigg|_{x_j=x_\beta}\right)\Psi\left(x_1,...,x_N\right) = 0 \tag{3.62}$$

and

$$\Psi\left(x_1,...,x_N\right)\big|_{x_j=x_\beta-0} = \Psi\left(x_1,...,x_N\right)\big|_{x_j=x_\beta+0}\,. \tag{3.63}$$

The left and right infinite wall conditions are

$$\Psi\left(x_1,...,x_N\right)\Big|_{x_j=-\frac{L}{2}} = 0\,, \tag{3.64}$$

and

$$\Psi\left(x_1,...,x_N\right)\Big|_{x_j=\frac{L}{2}} = 0\,, \tag{3.65}$$

and I will only consider the regions of space where the particles are ordered as

$$\mathcal{T} : x_1 \leq x_2 \leq \ldots \leq x_N. \tag{3.66}$$

All other regions can be obtained using bosonic symmetry.

Let us now denote the number of particles in the left, middle and right traps as n_{L}, n_{M} and n_{R}. Before we construct the ansatz wave function, it is natural to subdivide the space of the problem further into regions with different arrangements of the number of atoms between the traps n_{L}, $n_{\mathrm{M}} = N - n_{\mathrm{L}} - n_{\mathrm{R}}$ and n_{R} (see Fig. 3.2)

$$\mathcal{T}_{n_{\mathrm{L}},n_{\mathrm{R}}} : x_1 \leq x_2 \leq \ldots \leq x_{n_{\mathrm{L}}} \leq \boldsymbol{x_\alpha} \leq x_{n_{\mathrm{L}}+1} \leq \ldots \leq x_{N-n_{\mathrm{R}}} \leq \boldsymbol{x_\beta} \leq x_{N-n_{\mathrm{R}}+1} \leq \ldots \leq x_N. \tag{3.67}$$

The ansatz wave function is then a piecewise function consisting of the pieces defined on these regions

$$X\left(x_1,..,x_N\right) = \sum_{n_{\mathrm{L}}=0}^{N} \sum_{n_{\mathrm{R}}=0}^{N-n_{\mathrm{L}}} X_{n_{\mathrm{L}},n_{\mathrm{R}}}\left(x_1,...,x_N\right) \Theta\left(\mathcal{T}_{n_{\mathrm{L}},n_{\mathrm{R}}}\right), \tag{3.68}$$

where $X_{n_{\mathrm{L}},n_{\mathrm{R}}}\left(x_1,...,x_N\right)$ are defined on $\mathcal{T}_{n_{\mathrm{L}},n_{\mathrm{R}}}$, and the Heaviside theta function $\Theta\left(\mathcal{T}_{n_{\mathrm{L}},n_{\mathrm{R}}}\right)$ is non-zero only in region $\mathcal{T}_{n_{\mathrm{L}},n_{\mathrm{R}}}$. Analogously to section 3.2, the ansatz wavefunction in each region $\mathcal{T}_{n_{\mathrm{L}},n_{\mathrm{R}}}$ is a superposition of plane waves

$$X_{n_{\mathrm{L}},n_{\mathrm{R}}}\left(x_1,...,x_N\right) = \sum_{\vec{\epsilon}} \sum_{\vec{P}} \mathcal{A}_{n_{\mathrm{L}},n_{\mathrm{R}}}\left(\vec{\epsilon}\vec{P}\right) \times \exp\left[\mathrm{i}\sum_{l=1}^{N} \epsilon_{p_l} k_{p_l} x_l\right]. \tag{3.69}$$

All permuation notation is the same as in section 3.2.

The reflection against the walls of the box is only relevant to the leftmost particle in the left well and the rightmost particle in the right well, translating into the expressions for the left and right reflection matrices for the leftmost and the rightmost particle respectively

$$\overleftarrow{\mathcal{R}}^{1}_{n_{\mathrm{L}},n_{\mathrm{R}}}(\vec{\epsilon}\vec{P}) = \frac{\mathcal{A}_{n_{\mathrm{L}},n_{\mathrm{R}}}\left(-\epsilon_{p_1}k_{p_1}, \epsilon_{p_2}k_{p_2}, \ldots\right)}{\mathcal{A}_{n_{\mathrm{L}},n_{\mathrm{R}}}\left(\epsilon_{p_1}k_{p_1}, \epsilon_{p_2}k_{p_2}, \ldots\right)} = -\mathrm{e}^{-\mathrm{i}\epsilon_{p_1}k_{p_1}L}, \quad n_{\mathrm{L}} > 0 \tag{3.70}$$

$$\overrightarrow{\mathcal{R}}^{N}_{n_{\mathrm{L}},n_{\mathrm{R}}}(\vec{\epsilon}\vec{P}) = \frac{\mathcal{A}_{n_{\mathrm{L}},n_{\mathrm{R}}}\left(\ldots, \epsilon_{p_{N-1}}k_{p_{N-1}}, -\epsilon_{p_N}k_{p_N}\right)}{\mathcal{A}_{n_{\mathrm{L}},n_{\mathrm{R}}}\left(\ldots, \epsilon_{p_{N-1}}k_{p_{N-1}}, \epsilon_{p_N}k_{p_N}\right)} = -\mathrm{e}^{\mathrm{i}\epsilon_{p_N}k_{p_N}L}, \quad n_{\mathrm{R}} > 0 \tag{3.71}$$

From Eq. (3.59) we can obtain the relation for the scattering of two adjacent particles in the same well as

$$\mathcal{S}^{j-1,j}_{n_{\mathrm{L}},n_{\mathrm{R}}}\left(\vec{\epsilon}\vec{P}\right) = \frac{\mathcal{A}_{n_{\mathrm{L}},n_{\mathrm{R}}}\left(\epsilon_{p_1}p_1, ..., \epsilon_{p_j}p_j, \epsilon_{p_{j-1}}p_{j-1}, .., \epsilon_{p_N}p_N\right)}{\mathcal{A}_{n_{\mathrm{L}},n_{\mathrm{R}}}\left(\epsilon_{p_1}p_1, ..., \epsilon_{p_{j-1}}p_{j-1}, \epsilon_{p_j}p_j, .., \epsilon_{p_N}p_N\right)} = \frac{k_{p_j} - k_{p_{j-1}} + \frac{\mathrm{i}cm}{\hbar^2}}{k_{p_j} - k_{p_{j-1}} - \frac{\mathrm{i}cm}{\hbar^2}}, \tag{3.72}$$
$$j = 1, .., n_{\mathrm{L}} \cup n_{\mathrm{L}+1}, .., N - n_{\mathrm{R}} \cup N - n_{\mathrm{R}} + 1, .., N,$$

and any particle in the left well can then be scattered all the way towards the left wall

$$\begin{aligned}\mathcal{S}^{1,j}_{n_{\mathrm{L}},n_{\mathrm{R}}}\left(\vec{\epsilon}\vec{P}\right) =& \frac{\mathcal{A}_{n_{\mathrm{L}},n_{\mathrm{R}}}\left(\epsilon_{p_j}k_{p_j}, \epsilon_{p_1}k_{p_1}, .., \epsilon_{p_{n_{\mathrm{L}}}}k_{p_{n_{\mathrm{L}}}}, .., \epsilon_{p_N}k_{p_N}\right)}{\mathcal{A}_{n_{\mathrm{L}},n_{\mathrm{R}}}\left(\epsilon_{p_1}k_{p_1}, .., \epsilon_{p_j}k_{p_j}, .., \epsilon_{p_{n_{\mathrm{L}}}}k_{p_{n_{\mathrm{L}}}}, .., \epsilon_{p_N}k_{p_N}\right)} \\ &= \prod_{k=1}^{j-1} \frac{\epsilon_{p_j}k_{p_j} - \epsilon_{p_k}k_{p_k} + \frac{\mathrm{i}cm}{\hbar^2}}{\epsilon_{p_j}k_{p_j} - \epsilon_{p_k}k_{p_k} - \frac{\mathrm{i}cm}{\hbar^2}} \\ & j = 1, .., n_{\mathrm{L}}.\end{aligned} \tag{3.73}$$

The same reasoning can be applied to the particles in the right trap, so we can scatter the $j \geq N - n_{\mathrm{R}} + 1$-th particles in the right trap all the way to the right wall as

$$\begin{aligned}\mathcal{S}^{j,N}_{n_{\mathrm{L}},n_{\mathrm{R}}}\left(\vec{\epsilon}\vec{P}\right) =& \frac{\mathcal{A}_{n_{\mathrm{L}},n_{\mathrm{R}}}\left(\epsilon_{p_1}k_{p_1},..,\epsilon_{p_{N-n_{\mathrm{R}}+1}}k_{p_{N-n_{\mathrm{R}}+1}},..,\epsilon_{p_N}k_{p_N},\epsilon_{p_j}k_{p_j}\right)}{\mathcal{A}_{n_{\mathrm{L}},n_{\mathrm{R}}}\left(\epsilon_{p_1}k_{p_1},..,\epsilon_{p_N-n_{\mathrm{R}}+1}k_{p_N-n_{\mathrm{R}}+1},..,\epsilon_{p_j}k_{p_j},..,\epsilon_{p_N}k_{p_N}\right)} \\ &= \prod_{l=j+1}^{N}\frac{\epsilon_{p_l}k_{p_l}-\epsilon_{p_j}k_{p_j}+\frac{\mathrm{i}cm}{\hbar^2}}{\epsilon_{p_l}k_{p_l}-\epsilon_{p_j}k_{p_j}-\frac{\mathrm{i}cm}{\hbar^2}}, \\ & j = N-n_{\mathrm{R}}+1,..,N\end{aligned} \tag{3.74}$$

Analogous expression will be valid for particles scattering in the middle well.

In order to find expression for the reflection matrix for any particle in the left trap, we need to first scatter that particle with all the particles on the left, reflect it off the left wall and then scatter back until it returns to its original position. We can account for this by substituting Eq. (3.73) into Eq. (3.70)

$$\begin{aligned}\overleftarrow{\mathcal{R}}^{j}_{n_{\mathrm{L}},n_{\mathrm{R}}}\left(\vec{\epsilon}\vec{P}\right) &= \frac{\mathcal{A}_{n_{\mathrm{L}},n_{\mathrm{R}}}\left(\epsilon_{p_1}k_{p_1},..,-\epsilon_{p_j}k_{p_j},..,\epsilon_{p_{n_{\mathrm{L}}}}k_{p_{n_{\mathrm{L}}}},..,\epsilon_{p_N}k_{p_N}\right)}{\mathcal{A}_{n_{\mathrm{L}},n_{\mathrm{R}}}\left(\epsilon_{p_1}k_{p_1},..,\epsilon_{p_j}k_{p_j},..,\epsilon_{p_{n_{\mathrm{L}}}}k_{p_{n_{\mathrm{L}}}},..,\epsilon_{p_N}k_{p_N}\right)} \\ &\overset{Eq.\ (3.73)}{=} \frac{\prod_{k=1}^{j-1}\frac{-\epsilon_{p_j}k_{p_j}-\epsilon_{p_k}k_{p_k}-\frac{\mathrm{i}cm}{\hbar^2}}{-\epsilon_{p_j}k_{p_j}-\epsilon_{p_k}k_{p_k}+\frac{\mathrm{i}cm}{\hbar^2}}}{\prod_{k=1}^{j-1}\frac{\epsilon_{p_j}k_{p_j}-\epsilon_{p_k}k_{p_k}-\frac{\mathrm{i}cm}{\hbar^2}}{\epsilon_{p_j}k_{p_j}-\epsilon_{p_k}k_{p_k}+\frac{\mathrm{i}cm}{\hbar^2}}} \times \frac{\mathcal{A}_{n_{\mathrm{L}},n_{\mathrm{R}}}\left(-\epsilon_{p_j}k_{p_j},\epsilon_{p_1}k_{p_1},..,\epsilon_{p_{n_{\mathrm{L}}}}k_{p_{n_{\mathrm{L}}}},..,\epsilon_{p_N}k_{p_N}\right)}{\mathcal{A}_{n_{\mathrm{L}},n_{\mathrm{R}}}\left(\epsilon_{p_j}k_{p_j},\epsilon_{p_1}k_{p_1},..,\epsilon_{p_{n_{\mathrm{L}}}}k_{p_{n_{\mathrm{L}}}},..,\epsilon_{p_N}k_{p_N}\right)} \\ &\overset{Eq.\ (3.70)}{=} \prod_{k=1}^{j-1}\frac{\left(\epsilon_{p_j}k_{p_j}-\epsilon_{p_k}k_{p_k}+\frac{\mathrm{i}cm}{\hbar^2}\right)}{\left(\epsilon_{p_j}k_{p_j}-\epsilon_{p_k}k_{p_k}-\frac{\mathrm{i}cm}{\hbar^2}\right)}\frac{\left(\epsilon_{p_j}k_{p_j}+\epsilon_{p_k}k_{p_k}+\frac{\mathrm{i}cm}{\hbar^2}\right)}{\left(\epsilon_{p_j}k_{p_j}+\epsilon_{p_k}k_{p_k}-\frac{\mathrm{i}cm}{\hbar^2}\right)} \times \left(-e^{-\mathrm{i}\epsilon_{p_j}k_{p_j}L}\right) \\ &= \prod_{k=1}^{j-1}\frac{k^2_{p_j}-k^2_{p_k}+\frac{2\mathrm{i}cm}{\hbar^2}\epsilon_{p_j}k_{p_j}-\left(\frac{cm}{\hbar^2}\right)^2}{k^2_{p_j}-k^2_{p_k}-\frac{2\mathrm{i}cm}{\hbar^2}\epsilon_{p_j}k_{p_j}-\left(\frac{cm}{\hbar^2}\right)^2} \times \left(-e^{-\mathrm{i}\epsilon_{p_j}k_{p_j}L}\right), \\ & j = 1,\ldots,n_{\mathrm{L}}, \forall n_{\mathrm{L}} > 0, n_{\mathrm{R}} \leq N - n_{\mathrm{L}}.\end{aligned} \tag{3.75}$$

Note that for $j = n_{\mathrm{L}}$ this expression does not depend on the signs of all other momenta in the left trap or the order of the corresponding particles, but depends on the distribution of the particles between the traps.

Analogously to the left trap case, using Eq. (3.71) and Eq. (3.74) we obtain the right reflection matrix expression for all particles in the right trap, which reads

$$\begin{aligned}\overrightarrow{\mathcal{R}}^{j}_{n_{\mathrm{L}},n_{\mathrm{R}}}\left(\vec{\epsilon}\vec{P}\right) &= \prod_{l=j+1}^{N}\frac{k^2_{p_j}-k^2_{p_k}-\frac{2icm}{\hbar^2}\epsilon_{p_j}k_{p_j}-\left(\frac{cm}{\hbar^2}\right)^2}{k^2_{p_j}-k^2_{p_k}+\frac{2icm}{\hbar^2}\epsilon_{p_j}k_{p_j}-\left(\frac{cm}{\hbar^2}\right)^2} \times \left(-e^{i\epsilon_{p_j}k_{p_j}L}\right), \\ & j = N-n_{\mathrm{R}}+1,..,N, \forall n_{\mathrm{L}} > 0, n_{\mathrm{R}} \leq N - n_{\mathrm{L}}.\end{aligned} \tag{3.76}$$

Eq. (3.60) describes the scattering with the α-barrier. After substituting Eq. (3.68) into Eq. (3.60) and assuming independence of the regions, we obtain the equation for

each region as

$$\begin{aligned}
&\frac{\partial}{\partial x_n}\Big(X_{n-1,n_{\mathrm{R}}}(x_1,...,x_N)\,\Theta(\mathcal{T}_{n-1,n_{\mathrm{R}}})\Big)\Big|_{x_n=x_\alpha+0}\\
&-\frac{\partial}{\partial x_n}\Big(X_{n,n_{\mathrm{R}}}(x_1,...,x_N)\,\Theta(\mathcal{T}_{n,n_{\mathrm{R}}})\Big)\Big|_{x_n=x_\alpha-0}\\
&-\frac{2\alpha m}{\hbar^2}\left[X_{n-1,n_{\mathrm{R}}}(x_1,...,x_N)\,\Theta(\mathcal{T}_{n-1,n_{\mathrm{R}}})+X_{n,n_{\mathrm{R}}}(x_1,...,x_N)\,\Theta(\mathcal{T}_{n,n_{\mathrm{R}}})\right]|_{x_n=x_\alpha}=0,\\
&\forall n>0, n_{\mathrm{R}}\le N-n.
\end{aligned}\tag{3.77}$$

The partial derivative then gives

$$\begin{aligned}
&\Big(\frac{\partial}{\partial x_n}X_{n-1,n_{\mathrm{R}}}(x_1,...,x_N)\,\Theta(\mathcal{T}_{n-1,n_{\mathrm{R}}})\Big)\Big|_{x_n=x_\alpha+0}+(X_{n-1,n_{\mathrm{R}}}(x_1,...,x_N)\,\delta(x_n-x_\alpha))|_{x_n=x_\alpha+0}\\
&-\Big(\frac{\partial}{\partial x_n}X_{n,n_{\mathrm{R}}}(x_1,...,x_N)\,\Theta(\mathcal{T}_{n,n_{\mathrm{R}}})\Big)\Big|_{x_n=x_\alpha-0}-(X_{n,n_{\mathrm{R}}}(x_1,...,x_N)\,\delta(x_n-x_\alpha))|_{x_n=x_\alpha-0}\\
&-\frac{2\alpha m}{\hbar^2}(X_{n-1,n_{\mathrm{R}}}(x_1,...,x_N)\,\Theta(\mathcal{T}_{n-1,n_{\mathrm{R}}}))|_{x_n=x_\alpha}-\frac{2\alpha m}{\hbar^2}(X_{n,n_{\mathrm{R}}}(x_1,...,x_N)\,\Theta(\mathcal{T}_{n,n_{\mathrm{R}}}))|_{x_n=x_\alpha}=0,\\
&\forall n>0, n_{\mathrm{R}}\le N-n.
\end{aligned}\tag{3.78}$$

Since, by definition, we have

$$\Theta(\mathcal{T}_{n-1,n_{\mathrm{R}}})|_{x_n=x_\alpha+0}=\Theta(\mathcal{T}_{n,n_{\mathrm{R}}})|_{x_n=x_\alpha-0}=1,\tag{3.79}$$

$$\delta(x_n-x_\alpha)|_{x_n=x_\alpha+0}=\delta(x_n-x_\alpha)|_{x_n=x_\alpha-0}=0\,,\tag{3.80}$$

we get

$$\begin{aligned}
&\left[\frac{\partial}{\partial x_n}X_{n-1,n_{\mathrm{R}}}(x_1,...,x_N)-\frac{2\alpha m}{\hbar^2}X_{n-1,n_{\mathrm{R}}}(x_1,...,x_N)\right]\Big|_{x_n=x_\alpha}\\
&-\left[\frac{\partial}{\partial x_n}X_{n,n_{\mathrm{R}}}(x_1,...,x_N)+\frac{2\alpha m}{\hbar^2}X_{n,n_{\mathrm{R}}}(x_1,...,x_N)\right]\Big|_{x_n=x_\alpha}=0,\\
&\forall n>0, n_{\mathrm{R}}\le N-n.
\end{aligned}\tag{3.81}$$

After substituting Eq. (3.69) into Eq. (3.81), we get

$$\begin{aligned}
&\sum_{\vec{\epsilon}\,'}\sum_{\vec{P}}\Big[\mathcal{A}_{n-1,n_{\mathrm{R}}}\Big(\vec{\epsilon}\,'\vec{P},\epsilon_{p_n}=+1\Big)\,e^{\mathrm{i}k_{p_n}x_\alpha}\Big(\mathrm{i}k_{p_n}-\frac{2\alpha m}{\hbar^2}\Big)\\
&+\mathcal{A}_{n-1,n_{\mathrm{R}}}\Big(\vec{\epsilon}\,'\vec{P},\epsilon_{p_n}=-1\Big)\,e^{-\mathrm{i}k_{p_n}x_\alpha}\Big(-\mathrm{i}k_{p_n}-\frac{2\alpha m}{\hbar^2}\Big)\Big]\times\exp\left[\mathrm{i}\sum_{l\neq n}^{N}\epsilon_{p_l}k_{p_l}x_l\right]\\
&-\sum_{\vec{\epsilon}\,'}\sum_{\vec{P}}\Big[\mathcal{A}_{n,n_{\mathrm{R}}}\Big(\vec{\epsilon}\,'\vec{P},\epsilon_{p_n}=+1\Big)\,e^{\mathrm{i}k_{p_n}x_\alpha}\Big(\mathrm{i}k_{p_n}+\frac{2\alpha m}{\hbar^2}\Big)\\
&+\mathcal{A}_{n,n_{\mathrm{R}}}\Big(\vec{\epsilon}\,'\vec{P},\epsilon_{p_n}=-1\Big)\,e^{-\mathrm{i}k_{p_n}x_\alpha}\Big(-\mathrm{i}k_{p_n}+\frac{2\alpha m}{\hbar^2}\Big)\Big]\times\exp\left[\mathrm{i}\sum_{l\neq n}^{N}\epsilon_{p_l}k_{p_l}x_l\right]=0,
\end{aligned}\tag{3.82}$$

and taking into account the linear independence of the expressions under the sums, we can simplify this equation to

$$\begin{aligned}
&\mathcal{A}_{n-1,n_\mathrm{R}}\left(\vec{\epsilon}\,'\vec{P},\epsilon_{p_n}=+1\right)\left[\mathrm{i}k_{p_n}-\frac{2\alpha m}{\hbar^2}\right]\\
&+\mathcal{A}_{n-1,n_\mathrm{R}}\left(\vec{\epsilon}\,'\vec{P},\epsilon_{p_n}=-1\right)e^{-2\mathrm{i}k_{p_n}x_\alpha}\left[-\mathrm{i}k_{p_n}-\frac{2\alpha m}{\hbar^2}\right]\\
&-\mathcal{A}_{n,n_\mathrm{R}}\left(\vec{\epsilon}\,'\vec{P},\epsilon_{p_n}=+1\right)\left[\mathrm{i}k_{p_n}+\frac{2\alpha m}{\hbar^2}\right]\\
&-\mathcal{A}_{n,n_\mathrm{R}}\left(\vec{\epsilon}\,'\vec{P},\epsilon_{p_n}=-1\right)e^{-2\mathrm{i}k_{p_n}x_\alpha}\left[-\mathrm{i}k_{p_n}+\frac{2\alpha m}{\hbar^2}\right]=0.
\end{aligned}\tag{3.83}$$

We can use the left reflection matrix in Eq. (3.75) to express $\mathcal{A}_{n,n_\mathrm{R}}\left(\vec{\epsilon}\,'\vec{P},\epsilon_{p_n}=-1\right)$ and obtain

$$\begin{aligned}
&\mathcal{A}_{n-1,n_\mathrm{R}}\left(\vec{\epsilon}\,'\vec{P},\epsilon_{p_n}=+1\right)\left[\mathrm{i}k_{p_n}-\frac{2\alpha m}{\hbar^2}\right]\\
&+\mathcal{A}_{n-1,n_\mathrm{R}}\left(\vec{\epsilon}\,'\vec{P},\epsilon_{p_n}=-1\right)e^{-2\mathrm{i}k_{p_n}x_\alpha}\left[-\mathrm{i}k_{p_n}-\frac{2\alpha m}{\hbar^2}\right]\\
&-\mathcal{A}_{n,n_\mathrm{R}}\left(\vec{\epsilon}\,'\vec{P},\epsilon_{p_n}=+1\right)\left\{\left[\mathrm{i}k_{p_n}+\frac{2\alpha m}{\hbar^2}\right]+e^{-2\mathrm{i}k_{p_n}x_\alpha}\left[-\mathrm{i}k_{p_n}+\frac{2\alpha m}{\hbar^2}\right]\overleftarrow{\mathcal{R}}^{n}_{n,n_\mathrm{R}}\left(\vec{\epsilon}\vec{P}\right)\right\}\\
&=0.
\end{aligned}\tag{3.84}$$

Another condition on the wave function is the continuity condition from Eq. (3.61). By substituting Eq. (3.69) into Eq. (3.61) and assuming independence of the regions and different permutations of momenta, we obtain the relation

$$\begin{aligned}
&\mathcal{A}_{n,n_\mathrm{R}}\left(\vec{\epsilon}\,'\vec{P},\epsilon_{p_n}=+1\right)e^{\mathrm{i}k_{p_n}x_\alpha}+\mathcal{A}_{n,n_\mathrm{R}}\left(\vec{\epsilon}\,'\vec{P},\epsilon_{p_n}=-1\right)e^{-\mathrm{i}k_{p_n}x_\alpha}=\\
&\mathcal{A}_{n-1,n_\mathrm{R}}\left(\vec{\epsilon}\,'\vec{P},\epsilon_{p_n}=+1\right)e^{\mathrm{i}k_{p_n}x_\alpha}+\mathcal{A}_{n-1,n_\mathrm{R}}\left(\vec{\epsilon}\,'\vec{P},\epsilon_{p_n}=-1\right)e^{-\mathrm{i}k_{p_n}x_\alpha}.
\end{aligned}\tag{3.85}$$

By substituting $\mathcal{A}_{n,n_\mathrm{R}}\left(\vec{\epsilon}\,'\vec{P},\epsilon_{p_n}=-1\right)$ with an expression from Eq. (3.75) and multiplying by $e^{-\mathrm{i}k_{Pn}x_\alpha}$, we get

$$\begin{aligned}
&\mathcal{A}_{n,n_\mathrm{R}}\left(\vec{\epsilon}\,'\vec{P},\epsilon_{p_n}=+1\right)\left[1+e^{-\mathrm{i}2k_{Pn}x_\alpha}\mathcal{R}_{n,n_\mathrm{R}}\left(p_n,\tilde{P}'\right)\right]-\\
&-\mathcal{A}_{n-1,n_\mathrm{R}}\left(\vec{\epsilon}\,'\vec{P},\epsilon_{p_n}=+1\right)-\mathcal{A}_{n-1,n_\mathrm{R}}\left(\vec{\epsilon}\,'\vec{P},\epsilon_{p_n}=-1\right)e^{-\mathrm{i}2k_{p_n}x_\alpha}=0.
\end{aligned}\tag{3.86}$$

Now we can write the expressions for $\mathcal{A}_{n,n_\mathrm{R}}\left(\vec{\epsilon}\,'\vec{P},\epsilon_{p_n}=+1\right)$

$$\mathcal{A}_{n,n_\mathrm{R}}\left(\vec{\epsilon}\,'\vec{P},\epsilon_{p_n}=+1\right)=\frac{\mathcal{A}_{n-1,n_\mathrm{R}}\left(\vec{\epsilon}\,'\vec{P},\epsilon_{p_n}=+1\right)+\mathcal{A}_{n-1,n_\mathrm{R}}\left(\vec{\epsilon}\,'\vec{P},\epsilon_{p_n}=-1\right)e^{-\mathrm{i}2k_{p_n}x_\alpha}}{\left[1+e^{-\mathrm{i}2k_{p_n}x_\alpha}\overleftarrow{\mathcal{R}}^{n}_{n,n_\mathrm{R}}\left(\vec{\epsilon}\vec{P}\right)\right]},\tag{3.87}$$

and by substituting it into Eq. (3.84), we obtain

$$\begin{aligned}
\overleftarrow{\mathcal{R}}^{n}_{n-1,n_{\mathrm{R}}}\left(\vec{\epsilon}\vec{P}\right) &= \frac{\mathcal{A}_{n-1,n_{\mathrm{R}}}\left(\vec{\epsilon}\,'\vec{P},\epsilon_{p_n}=-1\right)}{\mathcal{A}_{n-1,n_{\mathrm{R}}}\left(\vec{\epsilon}\,'\vec{P},\epsilon_{p_n}=+1\right)} \\
&= \frac{\left[\mathrm{i}k_{p_n}-\frac{2\alpha m}{\hbar^2}\right]-\frac{\left[\mathrm{i}k_{p_n}+\frac{2\alpha m}{\hbar^2}\right]+e^{-2\mathrm{i}k_{p_n}x_\alpha}\left[-\mathrm{i}k_{p_n}+\frac{2\alpha m}{\hbar^2}\right]\overleftarrow{\mathcal{R}}^{n}_{n,n_{\mathrm{R}}}\left(\vec{\epsilon}\vec{P}\right)}{1+e^{-\mathrm{i}2k_{p_n}x_\alpha}\overleftarrow{\mathcal{R}}^{n}_{n,n_{\mathrm{R}}}\left(\vec{\epsilon}\vec{P}\right)}}{-\left[-\mathrm{i}k_{p_n}-\frac{2\alpha m}{\hbar^2}\right]+\frac{\left[\mathrm{i}k_{p_n}+\frac{2\alpha m}{\hbar^2}\right]+e^{-2\mathrm{i}k_{p_n}x_\alpha}\left[-\mathrm{i}k_{p_n}+\frac{2\alpha m}{\hbar^2}\right]\overleftarrow{\mathcal{R}}^{n}_{n,n_{\mathrm{R}}}\left(\vec{\epsilon}\vec{P}\right)}{1+e^{-\mathrm{i}2k_{p_n}x_\alpha}\overleftarrow{\mathcal{R}}^{n}_{n,n_{\mathrm{R}}}\left(\vec{\epsilon}\vec{P}\right)}} \times e^{2\mathrm{i}k_{p_n}x_\alpha} \\
&= \frac{-\frac{2\alpha m}{\hbar^2}+e^{-2\mathrm{i}k_{p_n}x_\alpha}\left[\mathrm{i}k_{p_n}-\frac{2\alpha m}{\hbar^2}\right]\overleftarrow{\mathcal{R}}^{n}_{n,n_{\mathrm{R}}}\left(\vec{\epsilon}\vec{P}\right)}{\left[\mathrm{i}k_{p_n}+\frac{2\alpha m}{\hbar^2}\right]+\frac{2\alpha m}{\hbar^2}e^{-2\mathrm{i}k_{p_n}x_\alpha}\overleftarrow{\mathcal{R}}^{n}_{n,n_{\mathrm{R}}}\left(\vec{\epsilon}\vec{P}\right)} \times e^{2\mathrm{i}k_{p_n}x_\alpha}.
\end{aligned} \tag{3.88}$$

Note, that if there is no α barrier, then $\overleftarrow{\mathcal{R}}^{n}_{n-1,n_{\mathrm{R}}}\left(\vec{\epsilon}\vec{P}\right)\Big|_{\alpha=0} = \overleftarrow{\mathcal{R}}^{n}_{n,n_{\mathrm{R}}}\left(\vec{\epsilon}\vec{P}\right)$, as expected.

If the reflecting particle is not the leftmost in the middle well, then we first have to scatter it with all the particles on its left (Eq. (3.73)) until it is the leftmost particle, then reflect it as in Eq. (3.88) and then scatter back with its neighbours until the particle is back at its position. The expression for the reflection matrix then reads

$$\begin{aligned}
&\overleftarrow{\mathcal{R}}^{n+j}_{n,n_{\mathrm{R}}}\left(\vec{\epsilon}\vec{P}\right) = \frac{\mathcal{A}_{n,n_{\mathrm{R}}}\left(\vec{\epsilon}\,'\vec{P},\epsilon_{p_{n+j}}=-1\right)}{\mathcal{A}_{n,n_{\mathrm{R}}}\left(\vec{\epsilon}\,'\vec{P},\epsilon_{p_{n+j}}=+1\right)} = \\
&\prod_{l=1}^{j-1}\frac{k^2_{p_{n+j}}-k^2_{p_{n+l}}+\frac{2\mathrm{i}cm}{\hbar^2}\epsilon_{p_{n+j}}k_{p_{n+j}}-\left(\frac{cm}{\hbar^2}\right)^2}{k^2_{p_{n+j}}-k^2_{p_{n+l}}-\frac{2\mathrm{i}cm}{\hbar^2}\epsilon_{p_{n+j}}k_{p_{n+j}}-\left(\frac{cm}{\hbar^2}\right)^2} \times \overleftarrow{\mathcal{R}}^{n}_{n,n_{\mathrm{R}}}\left(\dots,\epsilon_{p_n}p_n,\epsilon_{p_{n+j}}p_{n+j},\epsilon_{p_{n+1}}p_{n+1},\dots\right) \\
&0<j\leq N-n_{\mathrm{R}}-n.
\end{aligned} \tag{3.89}$$

We can also obtain an expression for $\mathcal{A}_{n-1,n_{\mathrm{R}}}\left(\vec{\epsilon}\,'\vec{P},\epsilon_{p_n}=-1\right)$ from Eq. (3.86)

$$\begin{aligned}
&\mathcal{A}_{n-1,n_{\mathrm{R}}}\left(\vec{\epsilon}\,'\vec{P},\epsilon_{p_n}=-1\right) = \\
&e^{2ik_{p_n}x_\alpha}\left(\mathcal{A}_{n,n_{\mathrm{R}}}\left(\vec{\epsilon}\,'\vec{P},\epsilon_{p_n}=+1\right)\left[1+e^{-i2k_{p_n}x_\alpha}\overleftarrow{\mathcal{R}}^{n}_{n,n_{\mathrm{R}}}\left(\vec{\epsilon}\vec{P}\right)\right]-\mathcal{A}_{n-1,n_{\mathrm{R}}}\left(\vec{\epsilon}\,'\vec{P},\epsilon_{p_n}=+1\right)\right).
\end{aligned} \tag{3.90}$$

This allows to reconstruct the scattering matrix for the n-th particle against the α-barrier from the block $(n-1,n_{\mathrm{R}})$ to the block (n,n_{R}) by substituting this expression

into Eq. (3.84)

$$\mathcal{S}^{\alpha,n}_{n,n_{\rm R}}\left(\vec{\epsilon}\vec{P}\right)=\frac{\mathcal{A}_{n,n_{\rm R}}\left(\vec{\epsilon}\vec{P}\right)}{\mathcal{A}_{n-1,n_{\rm R}}\left(\vec{\epsilon}\vec{P}\right)}= \\ \frac{\left[\mathrm{i}k_{p_n}-\frac{2\alpha m}{\hbar^2}\right]+\left[\mathrm{i}k_{p_n}+\frac{2\alpha m}{\hbar^2}\right]}{\left[\mathrm{i}k_{p_n}+\frac{2\alpha m}{\hbar^2}\right]\left(1+e^{-\mathrm{i}2k_{p_n}x_\alpha}\overleftarrow{\mathcal{R}}^{n}_{n,n_{\rm R}}\left(\vec{\epsilon}\vec{P}\right)\right)+\left[\mathrm{i}k_{p_n}+\frac{2\alpha m}{\hbar^2}\right]+e^{-2\mathrm{i}k_{p_n}x_\alpha}\left[-\mathrm{i}k_{p_n}+\frac{2\alpha m}{\hbar^2}\right]\overleftarrow{\mathcal{R}}^{n}_{n,n_{\rm R}}\left(\vec{\epsilon}\vec{P}\right)}= \\ \frac{\mathrm{i}k_{p_n}}{\left[\mathrm{i}k_{p_n}+\frac{2\alpha m}{\hbar^2}\right]+\frac{2\alpha m}{\hbar^2}e^{-\mathrm{i}2k_{p_n}x_\alpha}\overleftarrow{\mathcal{R}}^{n}_{n,n_{\rm R}}\left(\vec{\epsilon}\vec{P}\right)}. \tag{3.91}$$

Note, that in the absence of the α-barrier $\mathcal{S}^{\alpha,n}_{n,n_{\rm R}}\left(\vec{\epsilon}\vec{P}\right)\Big|_{\alpha=0}=1$ as expected.

Analogously to the left barrier, we can obtain the expression for the reflection matrix of an n-th particle in the block $(n_{\rm L},N-n)$ (the rightmost particle in the middle trap)

$$\overrightarrow{\mathcal{R}}^{n}_{n_{\rm L},N-n}\left(\vec{\epsilon}\vec{P}\right)=\frac{\mathcal{A}_{n_{\rm L},N-n}\left(\vec{\epsilon}\,'\vec{P},\epsilon_{p_n}=-1\right)}{\mathcal{A}_{n_{\rm L},N-n}\left(\vec{\epsilon}\,'\vec{P},\epsilon_{p_n}=+1\right)} \\ =\frac{-\frac{2\beta m}{\hbar^2}-e^{-\mathrm{i}2k_{p_n}x_\beta}\left[\mathrm{i}k_{p_n}+\frac{2\beta m}{\hbar^2}\right]\overrightarrow{\mathcal{R}}^{n}_{n_{\rm L},N-n+1}\left(\vec{\epsilon}\vec{P}\right)}{\left[-\mathrm{i}k_{p_n}+\frac{2\beta m}{\hbar^2}\right]+\frac{2\beta m}{\hbar^2}e^{-\mathrm{i}2k_{p_n}x_\beta}\overrightarrow{\mathcal{R}}^{n}_{n_{\rm L},N-n+1}\left(\vec{\epsilon}\vec{P}\right)}\times e^{\mathrm{i}2k_{p_n}x_\beta}. \tag{3.92}$$

Again, if there is no β-barrier, then $\overrightarrow{\mathcal{R}}^{n}_{n_{\rm L},N-n}\left(\vec{\epsilon}\vec{P}\right)\Big|_{\beta=0}=\overrightarrow{\mathcal{R}}^{n}_{n_{\rm L},N-n+1}\left(\vec{\epsilon}\vec{P}\right)$, as expected. We can also obtain the scattering matrix for the n-th particle against β-barrier from the block $(n_{\rm L},N-n)$ to the block $(n_{\rm L},N-n+1)$

$$\mathcal{S}^{\beta,n}_{n_{\rm L},N-n+1}\left(\vec{\epsilon}\vec{P}\right)=\frac{\mathcal{A}_{n_{\rm L},N-n+1}\left(\vec{\epsilon}\vec{P}\right)}{\mathcal{A}_{n_{\rm L},N-n}\left(\vec{\epsilon}\vec{P}\right)} \\ =\frac{\mathrm{i}k_{p_n}}{\left[\mathrm{i}k_{p_n}-\frac{2\beta m}{\hbar^2}\right]-\frac{2\beta m}{\hbar^2}e^{-\mathrm{i}2k_{p_n}x_\beta}\overrightarrow{\mathcal{R}}^{n}_{n_{\rm L},N-n+1}\left(\vec{\epsilon}\vec{P}\right)}. \tag{3.93}$$

If there is no β-barrier, $\mathcal{S}^{\beta,n}_{n_{\rm L},N-n+1}\left(\vec{\epsilon}\vec{P}\right)\Big|_{\beta=0}=1$, as expected.

3.3.1 The Yang–Baxter equations

In order for the Bethe ansatz solution to be correct, the Yang–Baxter (YB) equations, which ensure that all three-body scattering events are equal, have to be satisfied. In the system there are two types of three-body scattering events: the simultaneous scattering of two particles and a barrier and the scattering of three particles in the same well. The latter is trivially satisfied, however I will show below that the particle-barrier scattering does not satisfy the Yang–Baxter relations. Earlier we have denoted the

scattering matrix of a particle against the α-barrier as $\mathcal{S}^{\alpha,j}_{n_\mathrm{L},n_\mathrm{R}}\left(\vec{\epsilon}\vec{P}\right)$ and with the β-barrier as $\mathcal{S}^{\beta,j}_{n_\mathrm{L},n_\mathrm{R}}\left(\vec{\epsilon}\vec{P}\right)$. This notation means that the particle p_j scatters from the α-barrier to the left (β-barrier to the right), connecting the blocks $(n_\mathrm{L}-1,n_\mathrm{R})$ (or $(n_\mathrm{L},n_\mathrm{R}-1)$) with the block $(n_\mathrm{L},n_\mathrm{R})$. The scattering between two particles in the same well is denoted as $\mathcal{S}^{j,j+1}_{n_\mathrm{L},n_\mathrm{R}}(\vec{\epsilon}\vec{P})$, and is the same for all blocks as long as the two scattering particles p_j and p_{j+1} are in the same well.

The Yang–Baxter equations postulate that it should not matter if two particles first scatter with each other and then one-by-one with the barrier, or first scatter with the barrier and then scatter with each other in the new block

$$\begin{aligned}&\mathcal{S}^{\alpha,n}_{n,n_\mathrm{R}}(\vec{\epsilon}\vec{P})\mathcal{S}^{\alpha,n+1}_{n+1,n_\mathrm{R}}(\vec{\epsilon}\vec{P})\mathcal{S}^{n,n+1}_{n+1,n_\mathrm{R}}(\vec{\epsilon}\vec{P}) \overset{YB}{=}\\ &\mathcal{S}^{n,n+1}_{n-1,n_\mathrm{R}}(\vec{\epsilon}\vec{P})\mathcal{S}^{\alpha,n}_{n,n_\mathrm{R}}(\ldots,\epsilon_{p_{n+1}}k_{p_{n+1}},\epsilon_{p_n}k_{p_n})\mathcal{S}^{\alpha,n+1}_{n+1,n_\mathrm{R}}(\ldots,\epsilon_{p_{n+1}}k_{p_{n+1}},\epsilon_{p_n}k_{p_n}).\end{aligned} \tag{3.94}$$

Since the two scattering matrices $\mathcal{S}^{n,n+1}_{n-1,n_\mathrm{R}}(\vec{\epsilon}\vec{P})$ and $\mathcal{S}^{n,n+1}_{n+1,n_\mathrm{R}}(\vec{\epsilon}\vec{P})$ are equal, the relation can be written as

$$\begin{aligned}\mathcal{S}^{\alpha,n}_{n,n_\mathrm{R}}(\vec{\epsilon}\vec{P})\mathcal{S}^{\alpha,n+1}_{n+1,n_\mathrm{R}}(\vec{\epsilon}\vec{P}) = \mathcal{S}^{\alpha,n}_{n,n_\mathrm{R}}(\ldots,\epsilon_{p_{n+1}}k_{p_{n+1}},\epsilon_{p_n}k_{p_n})\mathcal{S}^{\alpha,n+1}_{n+1,n_\mathrm{R}}(\ldots,\epsilon_{p_{n+1}}k_{p_{n+1}},\epsilon_{p_n}k_{p_n}),\\ \forall\vec{P}, 0\geq n_\mathrm{R}\leq N-n-1,\end{aligned} \tag{3.95}$$

and a similar relation can be constructed for the β-barrier

$$\begin{aligned}\mathcal{S}^{\beta,n+1}_{n_\mathrm{L},N-n+2}(\vec{\epsilon}\vec{P})\mathcal{S}^{\beta,n}_{n_\mathrm{L},N-n+1}(\vec{\epsilon}\vec{P}) = \mathcal{S}^{\beta,n+1}_{n_\mathrm{L},N-n+2}(\ldots,\epsilon_{p_{n+1}}k_{p_{n+1}},\epsilon_{p_n}k_{p_n})\mathcal{S}^{\beta,n}_{n_\mathrm{L},N-n+1}(\ldots,\epsilon_{p_{n+1}}k_{p_{n+1}},\epsilon_{p_n}k_{p_n}),\\ \forall\vec{P}, 0\geq n_\mathrm{L}\leq n-2.\end{aligned} \tag{3.96}$$

In the non-interacting case and the Tonks–Girardeau limit of infinitely repulsive interactions the YB equations are trivially satisfied. However, if both barriers have finite height and the interaction between the particles is finite, then the Yang–Baxter equations have consistent solutions only at non-physical values of quasi-momenta $k_{1,2}=0$ and $\pm k_1=\pm k_2$. An example of the curves given by the real and imaginary parts of the Yang–Baxter equations with both barriers having non-zero heights are shown as colored curves in Fig. 3.3. It is easy to see that even the curves which correspond to the real and imaginary parts of the same equation have very few intersection points. The only lines where all four parts coincide are the non-physical $k_{1,2}=0$ and $\pm k_1=\pm k_2$ lines. This pattern continues beyond the quaasi-momentum values shown in Fig. 3.3.

In the special case of one barrier having a zero height and another one positioned in the center of the trap, there is only one non-trivial YB relation. The remaining YB equation together with the Bethe equations form a system of three equation for two variables. Despite the system being overdetermined, there are non-trivial solutions for the quasi-momenta. One of such states is the odd-parity $|b\rangle=(|LL\rangle-|RR\rangle)/\sqrt{2}$ (NOON) state, where particles are in superposition of both being on in the left and in the right wells. Liu and Zhang [148] obtained these solutions using the approach outlined above, and analytically investigated the tunneling dynamics of the odd-parity state $|b\rangle$ with arbitrary interaction strength. They have concluded that the occupation

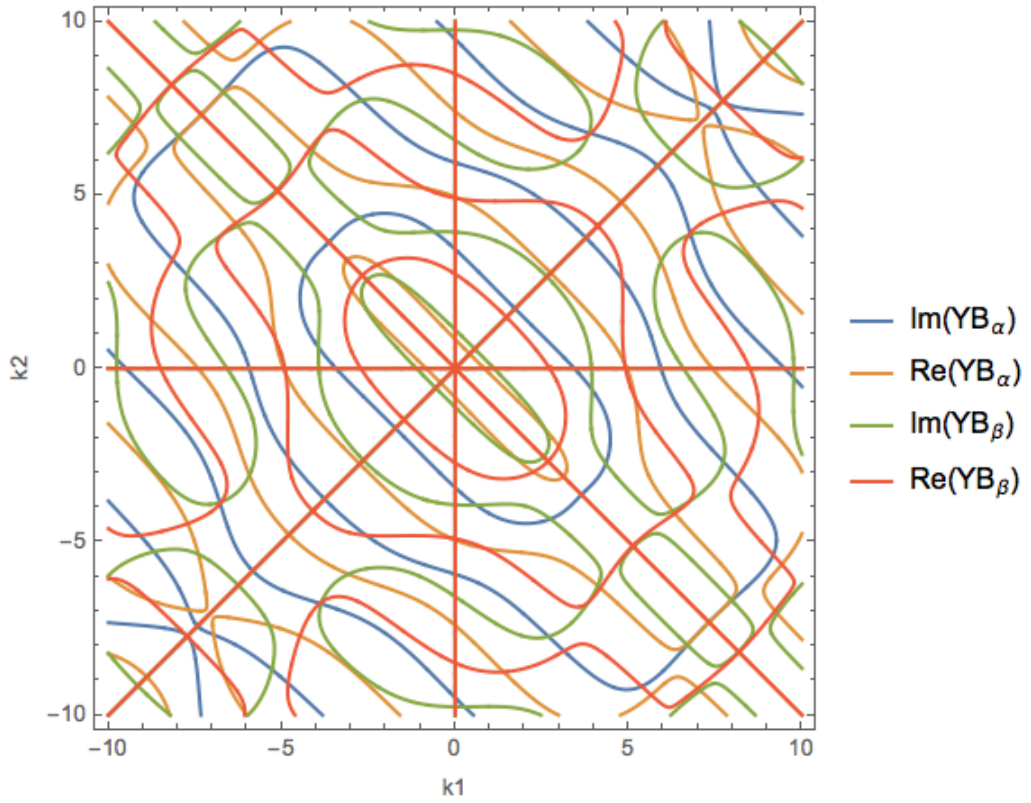

Figure 3.3: An example of the curves given by the Yang–Baxter equations in eqs. (3.95) and (3.96). The four curves correspond to the real and imaginary parts of the eqs. (3.95) and (3.96) with $L = 10, x_\alpha = -2, x_\beta = 1, \alpha = 2, \beta = 1, c = 1$. The allowed values of quasi-momenta k_1 and k_2 are given by the intersection of all four curves. Only the non-physical values $k_{1,2} = 0$ and $\pm k_1 = \pm k_2$ of quasi-momenta satisfy all four equations and all four curves coincide. Here I use natural units $\hbar = m = 1$.

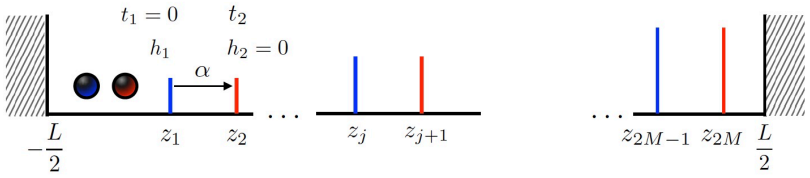

Figure 3.4: Schematic of the finite arbitrary KP model with two distinguishable particles. The two particles *see* the barriers at slightly shifted positions. This is equivalent to saying that the first particle sees the barrier j at the position z_j with the height $h_j \neq 0$, while the second particle sees it having zero height $t_j = 0$. This is reversed for the barrier $j+1$, for which the apparent height is $h_{j+1} = 0$ for the first particle.

probablities had strong dependence on the interaction which could not be explained by the two-mode model used in the experiment by the Heidelberg group [123].

In this section I have shown that the many-body system with two barriers of finite height is not generally solvable if the interactions between the particles are finite due to the breakdown of the YB relations. Below I will consider two modifications of this model - a model with two distinguishable particles with slightly shifted effective external potential, and a single-particle system with arbitrary number of barriers of arbitrary heights positioned arbitrarily in the box (the arbitrary finite Kronig–Penney model).

3.4 Two distinguishable particles in the finite arbitrary Kronig–Penney model

As we have shown in 3.3, the infinite square well model with two barrier (and consequently, the full AFKP model) is not solvable for more than one particle due to violation of the Yang–Baxter relations. In an attempt to rectify this, I proposed a modification of the AFKP model with two particles where true 3-body interactions are not possible. For this let us consider two interacting distinguishable particles in a square well. In addition to the square well the particles experience an external potential which consists of point-like barriers, but the positions of these barriers are relatively shifted for the two particles (see Fig. 3.4). The Hamiltonian is then

$$\hat{H} = -\frac{\hbar^2}{2m}\left(\frac{\partial^2}{\partial x^2} + \frac{\partial^2}{\partial y^2}\right) + V_x(x) + V_y(y) + c\delta(x-y), \tag{3.97}$$

where

$$V_x(x) = \sum_{j=1}^{M} h_j \delta(x - z_j), \tag{3.98}$$

$$V_y(y) = \sum_{j=1}^{M} h_j \delta(y - z_j - \alpha). \tag{3.99}$$

Another way to write the external potentials is to consider $2M$ barriers, where even barriers are shifted by α with respect to odd ones ($z_{2j} - z_{2j-1} = \alpha$), and set the heights of the odd barriers for particle y (t_{2l-1}) and even barriers for particle x (h_{2l}) to be zero. Then the external potential reads

$$V(x,y) = \sum_{j=1}^{2M} \left(h_j \delta(x - z_j) + t_j \delta(y - z_j) \right), \tag{3.100}$$

where

$$\begin{aligned} &h_{2l} = t_{2l-1} = 0, \\ &h_{2l-1} = t_{2l}, \\ &z_{2l} = z_{2l-1} + \alpha,\ l = 1, \ldots, M. \end{aligned} \tag{3.101}$$

Similarly to sections 3.2 and 3.5, the problem can be simplified to the free-particle problem with the boundary conditions on the wavefunction given by

$$\Psi\left(x = \pm\tfrac{L}{2}\right) = 0, \tag{3.102}$$

$$\Psi\left(y = \pm\tfrac{L}{2}\right) = 0, \tag{3.103}$$

$$\left(\tfrac{\partial}{\partial x}\Big|_{x=z_n+0} - \tfrac{\partial}{\partial x}\Big|_{x=z_n-0} - \tfrac{2mh_n}{\hbar^2}\Big|_{x=z_n}\right)\Psi(x,y) = 0 \quad ,\ n = 1, ..., 2M. \tag{3.104}$$

$$\left(\tfrac{\partial}{\partial y}\Big|_{y=z_n+0} - \tfrac{\partial}{\partial y}\Big|_{y=z_n-0} - \tfrac{2mt_n}{\hbar^2}\Big|_{y=z_n}\right)\Psi(x,y) = 0 \quad ,\ n = 1, ..., 2M. \tag{3.105}$$

$$\Psi|_{x=z_n-0} = \Psi|_{x=z_n+0},\ n = 1, ..., 2M.\ , \tag{3.106}$$

$$\Psi|_{y=z_n-0} = \Psi|_{y=z_n+0},\ n = 1, ..., 2M.\ , \tag{3.107}$$

$$\left(\tfrac{\partial}{\partial x} - \tfrac{\partial}{\partial y}\right)\Psi|_{x-y=0^+} - \left(\tfrac{\partial}{\partial x} - \tfrac{\partial}{\partial y}\right)\Psi|_{x-y=0^-} = \tfrac{2mc}{\hbar^2}\,\Psi|_{x=y}\ , \tag{3.108}$$

$$\Psi|_{x-y=0^+} = \Psi|_{x-y=0^-}\ . \tag{3.109}$$

The wavefunction ansatz can then be written as

$$\Psi(x,y) = \phi(x,y)\theta(x < y) + \psi(x,y)\theta(y \leq x), \tag{3.110}$$

where

$$\phi(x,y) = \sum_{l=1}^{2M+1} \sum_{j=1}^{l} \sum_{P} \sum_{\vec{\epsilon}} \mathcal{A}_{j,l}^{\vec{\epsilon}P} \mathrm{e}^{\mathrm{i}(\epsilon_x k_{p_1} x + \epsilon_y k_{p_2} y)} \Theta(\mathcal{D}_j^x)\Theta(\mathcal{D}_l^y), \tag{3.111}$$

$$\psi(x,y) = \sum_{j=1}^{2M+1} \sum_{l=1}^{j} \sum_{P} \sum_{\vec{\epsilon}} \mathcal{B}_{j,l}^{\vec{\epsilon}P} \mathrm{e}^{\mathrm{i}(\epsilon_x k_{p_1} x + \epsilon_y k_{p_2} y)} \Theta(\mathcal{D}_j^x)\Theta(\mathcal{D}_l^y), \tag{3.112}$$

and where $\mathcal{D}_l^x$ and $\mathcal{D}_l^y$ denote particles being in l-th well

$$\begin{aligned} &\mathcal{D}_l^\beta : z_{l-1} \leq \beta < z_l,\ \beta = \{x, y\} \\ &z_0 = -\frac{L}{2}, \\ &z_{2M+1} = \frac{L}{2}. \end{aligned} \tag{3.113}$$

Let us first consider the boundary conditions at the walls given by Eq. (3.102) and (3.103). Similarly to the procedure in Eq. (3.12) in section 3.2, we get the reflection conditions for the first and the last wells for each particle

$$\overleftarrow{\mathcal{R}}^{x\mathcal{A}_{1,l}}_{\vec{\epsilon}P} = \frac{\mathcal{A}_{1,l}^{-\epsilon_x k_{p_1},\epsilon_y k_{p_2}}}{\mathcal{A}_{1,l}^{\epsilon_x k_{p_1},\epsilon_y k_{p_2}}} = -\mathrm{e}^{-\mathrm{i}\epsilon_x k_{p_1} L},\ l = 1,\dots,2M+1, \tag{3.114}$$

$$\overrightarrow{\mathcal{R}}^{x\mathcal{B}_{2M+1,l}}_{\vec{\epsilon}P} = \frac{\mathcal{B}_{2M+1,l}^{-\epsilon_x k_{p_1},\epsilon_y k_{p_2}}}{\mathcal{B}_{2M+1,l}^{\epsilon_x k_{p_1},\epsilon_y k_{p_2}}} = -\mathrm{e}^{\mathrm{i}\epsilon_x k_{p_1} L},\ l = 1,\dots,2M+1, \tag{3.115}$$

$$\overleftarrow{\mathcal{R}}^{y\mathcal{B}_{j,1}}_{\vec{\epsilon}P} = \frac{\mathcal{B}_{j,1}^{\epsilon_x k_{p_1},-\epsilon_y k_{p_2}}}{\mathcal{B}_{j,1}^{\epsilon_x k_{p_1},\epsilon_y k_{p_2}}} = -\mathrm{e}^{-\mathrm{i}\epsilon_y k_{p_2} L},\ j = 1,\dots,2M+1, \tag{3.116}$$

$$\overrightarrow{\mathcal{R}}^{y\mathcal{A}_{j,2M+1}}_{\vec{\epsilon}P} = \frac{\mathcal{A}_{j,2M+1}^{\epsilon_x k_{p_1},-\epsilon_y k_{p_2}}}{\mathcal{A}_{j,2M+1}^{\epsilon_x k_{p_1},\epsilon_y k_{p_2}}} = -\mathrm{e}^{\mathrm{i}\epsilon_y k_{p_2} L},\ j = 1,\dots,2M+1. \tag{3.117}$$

Now let us consider the boundary conditions which connect two adjacent wells for particle x in case where $x < y$, namely Eq. (3.104) and (3.106). From the continuity condition Eq. (3.106) we get

$$\sum_{\vec{\epsilon}P} \left(\mathcal{A}_{n,l}^{\vec{\epsilon}P}\mathrm{e}^{\mathrm{i}\epsilon_x k_{p_1} z_n} - \mathcal{A}_{n+1,l}^{\vec{\epsilon}P}\mathrm{e}^{\mathrm{i}\epsilon_x k_{p_1} z_n}\right) = 0,\ l = n+1,\dots,2M+1, \tag{3.118}$$

which gives

$$\mathcal{A}_{n,l}^{\epsilon_x k_{p_1},\epsilon_y k_{p_2}} - \mathcal{A}_{n+1,l}^{\epsilon_x k_{p_1},\epsilon_y k_{p_2}} + \mathrm{e}^{-2\mathrm{i}\epsilon_x k_{p_1} z_n}\left(\mathcal{A}_{n,l}^{-\epsilon_x k_{p_1},\epsilon_y k_{p_2}} - \mathcal{A}_{n+1,l}^{-\epsilon_x k_{p_1},\epsilon_y k_{p_2}}\right) = 0,\ l = n+1,\dots,2M+1. \tag{3.119}$$

On the other hand, the condition for the derivative in Eq. (3.104) gives

$$\sum_{\vec{\epsilon}P}\left(\mathrm{i}\epsilon_x k_{p_1}(\mathcal{A}_{n+1,l}^{\epsilon_x k_{p_1},\epsilon_y k_{p_2}}\mathrm{e}^{\mathrm{i}\epsilon_x k_{p_1} z_n} - \mathcal{A}_{n,l}^{\epsilon_x k_{p_1},\epsilon_y k_{p_2}}\mathrm{e}^{\mathrm{i}\epsilon_x k_{p_1} z_n}) - \frac{2mh_n}{\hbar^2}\mathcal{A}_{n+1,l}^{\epsilon_x k_{p_1},\epsilon_y k_{p_2}}\mathrm{e}^{\mathrm{i}\epsilon_x k_{p_1} z_n}\right) = 0, \tag{3.120}$$

which simplifies to

$$\begin{aligned}&\mathrm{i}\epsilon_x k_{p_1}\left(-\mathcal{A}_{n,l}^{\epsilon_x k_{p_1},\epsilon_y k_{p_2}} + \mathcal{A}_{n,l}^{-\epsilon_x k_{p_1},\epsilon_y k_{p_2}}\mathrm{e}^{-2\mathrm{i}\epsilon_x k_{p_1} z_n}\right) + \left(\mathrm{i}\epsilon_x k_{p_1} - \frac{2mh_n}{\hbar^2}\right)\mathcal{A}_{n+1,l}^{\epsilon_x k_{p_1},\epsilon_y k_{p_2}} \\ &- \left(\mathrm{i}\epsilon_x k_{p_1} + \frac{2mh_n}{\hbar^2}\right)\mathcal{A}_{n+1,l}^{-\epsilon_x k_{p_1},\epsilon_y k_{p_2}}\mathrm{e}^{-2\mathrm{i}\epsilon_x k_{p_1} z_n} = 0.\end{aligned} \tag{3.121}$$

After substituting the expression for $\mathcal{A}_{n+1,l}^{-\epsilon_x k_{p_1},\epsilon_y k_{p_2}}$ from Eq. (3.119) into Eq. (3.121), we obtain

$$-\left(\mathrm{i}\epsilon_x k_{p_1} + \frac{2mh_n}{\hbar^2}\right)\mathcal{A}_{n,l}^{\epsilon_x k_{p_1},\epsilon_y k_{p_2}} - \frac{mh_n}{\hbar^2}\mathrm{e}^{-2\mathrm{i}\epsilon_x k_{p_1} z_n}\mathcal{A}_{n,l}^{-\epsilon_x k_{p_1},\epsilon_y k_{p_2}} + \mathrm{i}\epsilon_x k_{p_1}\mathcal{A}_{n+1,l}^{\epsilon_x k_{p_1},\epsilon_y k_{p_2}} = 0. \tag{3.122}$$

Let us define the reflection matrix for the particle x in the $x < y$ region as

$$\overleftarrow{\mathcal{R}}^{x\mathcal{A}_{n+1,l}}_{\vec{\epsilon}P} = \frac{\mathcal{A}^{-\epsilon_x k_{p_1},\epsilon_y k_{p_2}}_{n+1,l}}{\mathcal{A}^{\epsilon_x k_{p_1},\epsilon_y k_{p_2}}_{n+1,l}}, \tag{3.123}$$

and use this expression in Eq. (3.119) to obtain

$$\mathcal{A}^{\epsilon_x k_{p_1},\epsilon_y k_{p_2}}_{n+1,l}\left(1+\mathrm{e}^{-2\mathrm{i}\epsilon_x k_{p_1} z_n}\overleftarrow{\mathcal{R}}^{x\mathcal{A}_{n+1,l}}_{\vec{\epsilon}P}\right) = \mathcal{A}^{\epsilon_x k_{p_1},\epsilon_y k_{p_2}}_{n,l} + \mathrm{e}^{-2\mathrm{i}\epsilon_x k_{p_1} z_n}\mathcal{A}^{-\epsilon_x k_{p_1},\epsilon_y k_{p_2}}_{n,l}. \tag{3.124}$$

Eq. (3.122), one the other hand, gives

$$\mathrm{i}\epsilon_x k_{p_1}\mathcal{A}^{\epsilon_x k_{p_1},\epsilon_y k_{p_2}}_{n+1,l} = \left(\mathrm{i}\epsilon_x k_{p_1} + \frac{2mh_n}{\hbar^2}\right)\mathcal{A}^{\epsilon_x k_{p_1},\epsilon_y k_{p_2}}_{n,l} + \frac{mh_n}{\hbar^2}\mathrm{e}^{-2\mathrm{i}\epsilon_x k_{p_1} z_n}\mathcal{A}^{-\epsilon_x k_{p_1},\epsilon_y k_{p_2}}_{n,l}. \tag{3.125}$$

If we devide these two expression, we obtain

$$1+\mathrm{e}^{-2\mathrm{i}\epsilon_x k_{p_1} z_n}\overleftarrow{\mathcal{R}}^{x\mathcal{A}_{n+1,l}}_{\vec{\epsilon}P} = \frac{\mathrm{i}\epsilon_x k_{p_1}\left(\mathcal{A}^{\epsilon_x k_{p_1},\epsilon_y k_{p_2}}_{n,l} + \mathrm{e}^{-2\mathrm{i}\epsilon_x k_{p_1} z_n}\mathcal{A}^{-\epsilon_x k_{p_1},\epsilon_y k_{p_2}}_{n,l}\right)}{\left(\mathrm{i}\epsilon_x k_{p_1} + \frac{2mh_n}{\hbar^2}\right)\mathcal{A}^{\epsilon_x k_{p_1},\epsilon_y k_{p_2}}_{n,l} + \frac{mh_n}{\hbar^2}\mathrm{e}^{-2\mathrm{i}\epsilon_x k_{p_1} z_n}\mathcal{A}^{-\epsilon_x k_{p_1},\epsilon_y k_{p_2}}_{n,l}}. \tag{3.126}$$

By dividing both numerator and denominator of the right hand side by $\mathcal{A}^{\epsilon_x k_{p_1},\epsilon_y k_{p_2}}_{n,l}$ and performing straightforward simplifications, we get the recursive expression for the reflection matrix of particle x in the region $x < y$ as

$$\overleftarrow{\mathcal{R}}^{x\mathcal{A}_{n,l}}_{\vec{\epsilon}P} = \frac{-\frac{mh_{n-1}}{\hbar^2}\mathrm{e}^{\mathrm{i}2z_{n-1}\epsilon_x k_{p_1}} + \left[\mathrm{i}\epsilon_x k_{p_1} - \frac{mh_{n-1}}{\hbar^2}\right]\overleftarrow{\mathcal{R}}^{x\mathcal{A}_{n-1,l}}_{\vec{\epsilon}P}}{\left[\mathrm{i}\epsilon_x k_{p_1} + \frac{mh_{n-1}}{\hbar^2}\right] + \frac{mh_{n-1}}{\hbar^2}\mathrm{e}^{-\mathrm{i}2z_{n-1}\epsilon_x k_{p_1}}\overleftarrow{\mathcal{R}}^{x\mathcal{A}_{n-1,l}}_{\vec{\epsilon}P}}, \tag{3.127}$$
$$n = 2,\ldots,2M+1,\ l = n,\ldots,2M+1.$$

Using similar derivations, we also obtain the remaining reflection matrix elements

$$\overrightarrow{\mathcal{R}}^{x\mathcal{B}_{n,l}}_{\vec{\epsilon}P} = \frac{\mathcal{B}^{-\epsilon_x k_{p_1},\epsilon_y k_{p_2}}_{n,l}}{\mathcal{B}^{\epsilon_x k_{p_1},\epsilon_y k_{p_2}}_{n,l}} = \frac{\frac{mh_n}{\hbar^2}\mathrm{e}^{\mathrm{i}2z_n\epsilon_x k_{p_1}} + \left[\mathrm{i}\epsilon_x k_{p_1} + \frac{mh_n}{\hbar^2}\right]\overrightarrow{\mathcal{R}}^{x\mathcal{B}_{n+1,l}}_{\vec{\epsilon}P}}{\left[\mathrm{i}\epsilon_x k_{p_1} - \frac{mh_n}{\hbar^2}\right] - \frac{mh_n}{\hbar^2}\mathrm{e}^{-\mathrm{i}2z_n\epsilon_x k_{p_1}}\overrightarrow{\mathcal{R}}^{x\mathcal{B}_{n+1,l}}_{\vec{\epsilon}P}}, \tag{3.128}$$
$$n = 1,\ldots,2M,\ l = 1,\ldots,n,$$

$$\overrightarrow{\mathcal{R}}^{y\mathcal{A}_{j,n}}_{\vec{\epsilon}P} = \frac{\mathcal{A}^{\epsilon_x k_{p_1},-\epsilon_y k_{p_2}}_{j,n}}{\mathcal{A}^{\epsilon_x k_{p_1},\epsilon_y k_{p_2}}_{j,n}} = \frac{\frac{mt_n}{\hbar^2}\mathrm{e}^{\mathrm{i}2z_n\epsilon_y k_{p_2}} + \left[\mathrm{i}\epsilon_y k_{p_2} + \frac{mt_n}{\hbar^2}\right]\overrightarrow{\mathcal{R}}^{y\mathcal{A}_{j,n+1}}_{\vec{\epsilon}P}}{\left[\mathrm{i}\epsilon_y k_{p_2} - \frac{mt_n}{\hbar^2}\right] - \frac{mt_n}{\hbar^2}\mathrm{e}^{-\mathrm{i}2z_n\epsilon_y k_{p_2}}\overrightarrow{\mathcal{R}}^{y\mathcal{A}_{j,n+1}}_{\vec{\epsilon}P}}, \tag{3.129}$$
$$n = 1,\ldots,2M,\ j = 1,\ldots,n,$$

$$\overleftarrow{\mathcal{R}}^{y\mathcal{B}_{j,n}}_{\vec{\epsilon}P} = \frac{\mathcal{B}^{\epsilon_x k_{p_1},-\epsilon_y k_{p_2}}_{j,n}}{\mathcal{B}^{\epsilon_x k_{p_1},\epsilon_y k_{p_2}}_{j,n}} = \frac{-\frac{mt_{n-1}}{\hbar^2}\mathrm{e}^{\mathrm{i}2z_{n-1}\epsilon_y k_{p_2}} + \left[\mathrm{i}\epsilon_y k_{p_2} - \frac{mt_{n-1}}{\hbar^2}\right]\overleftarrow{\mathcal{R}}^{y\mathcal{B}_{j,n-1}}_{\vec{\epsilon}P}}{\left[\mathrm{i}\epsilon_y k_{p_2} + \frac{mt_{n-1}}{\hbar^2}\right] + \frac{mt_{n-1}}{\hbar^2}\mathrm{e}^{-\mathrm{i}2z_{n-1}\epsilon_y k_{p_2}}\overleftarrow{\mathcal{R}}^{y\mathcal{B}_{j,n-1}}_{\vec{\epsilon}P}}, \tag{3.130}$$
$$n = 2,\ldots,2M+1,\ j = n,\ldots,2M+1.$$

Now let us consider the scattering between the particles described be the boundary conditions in Eq. (3.108) and Eq. (3.109). Taking into account the ansatz in Eq. (3.110), the boundary conditions become

$$\left(\frac{\partial}{\partial x} - \frac{\partial}{\partial y}\right)\psi|_{x=y} - \left(\frac{\partial}{\partial x} - \frac{\partial}{\partial y}\right)\phi|_{x=y} = \tfrac{2mc}{\hbar^2}\,\psi|_{x=y}\,, \tag{3.131}$$

$$\psi|_{x=y} = \phi|_{x=y}\,. \tag{3.132}$$

Since the two particles can only scatter if they are in the same well, these give

$$\sum_{n=1}^{2M+1}\sum_{\vec{\epsilon}P}\left[\left(\mathrm{i}(\epsilon_x k_{p_1}-\epsilon_y k_{p_2})-\tfrac{2mc}{\hbar^2}\right)\mathcal{B}_{n,n}^{\vec{\epsilon}P}-\mathrm{i}(\epsilon_x k_{p_1}-\epsilon_y k_{p_2})\mathcal{A}_{n,n}^{\vec{\epsilon}P}\right]\mathrm{e}^{\mathrm{i}(\epsilon_x k_{p_1}+\epsilon_y k_{p_2})x}=0, \tag{3.133}$$

$$\sum_{n=1}^{2M+1}\sum_{\vec{\epsilon}P}\left(\mathcal{A}_{n,n}^{\vec{\epsilon}P}-\mathcal{B}_{n,n}^{\vec{\epsilon}P}\right)=0. \tag{3.134}$$

The exponential term $\mathrm{e}^{\mathrm{i}(\epsilon_x k_{p_1}+\epsilon_y k_{p_2})x}$ is equivalent for momenta and sign permutations $\vec{\epsilon}P=(\epsilon_x k_{p_1},\epsilon_y k_{p_2})$ and $\overleftrightarrow{\vec{\epsilon}P}=(\epsilon_y k_{p_2},\epsilon_x k_{p_1})$, which gives

$$\mathrm{i}(\epsilon_x k_{p_1}-\epsilon_y k_{p_2})\left(\mathcal{B}_{n,n}^{\vec{\epsilon}P}-\mathcal{A}_{n,n}^{\vec{\epsilon}P}-\mathcal{B}_{n,n}^{\overleftrightarrow{\vec{\epsilon}P}}+\mathcal{A}_{n,n}^{\overleftrightarrow{\vec{\epsilon}P}}\right)=\frac{2mc}{\hbar^2}\left(\mathcal{B}_{n,n}^{\vec{\epsilon}P}+\mathcal{B}_{n,n}^{\overleftrightarrow{\vec{\epsilon}P}}\right), \tag{3.135}$$

and

$$\mathcal{B}_{n,n}^{\vec{\epsilon}P}+\mathcal{B}_{n,n}^{\overleftrightarrow{\vec{\epsilon}P}}=\mathcal{A}_{n,n}^{\vec{\epsilon}P}+\mathcal{A}_{n,n}^{\overleftrightarrow{\vec{\epsilon}P}}. \tag{3.136}$$

After substitution of the expression for $\mathcal{B}_{n,n}^{\overleftrightarrow{\vec{\epsilon}P}}$ from Eq. (3.136) into Eq. (3.135), we obtain

$$\mathrm{i}(\epsilon_x k_{p_1}-\epsilon_y k_{p_2})\left(\mathcal{B}_{n,n}^{\vec{\epsilon}P}-\mathcal{A}_{n,n}^{\vec{\epsilon}P}\right)=\frac{mc}{\hbar^2}\left(\mathcal{A}_{n,n}^{\vec{\epsilon}P}+\mathcal{A}_{n,n}^{\overleftrightarrow{\vec{\epsilon}P}}\right). \tag{3.137}$$

Let us denote the two different particle scattering matrices

$$\mathcal{S}_{n,\vec{\epsilon}P}^{xy}=\frac{\mathcal{B}_{n,n}^{\vec{\epsilon}P}}{\mathcal{A}_{n,n}^{\vec{\epsilon}P}}, \tag{3.138}$$

which corresponds to the particles exchanging positions upon scattering (going through each other), and

$$\mathcal{S}_{\vec{\epsilon}P}^{\mathcal{A}_n}=\frac{\mathcal{A}_{n,n}^{\overleftrightarrow{\vec{\epsilon}P}}}{\mathcal{A}_{n,n}^{\vec{\epsilon}P}}, \tag{3.139}$$

which corresponds to the particles exchanging momenta (bouncing off each other). Together with Eq. (3.137) these give the relation between the two scattering matrices as

$$\mathcal{S}_{n,\vec{\epsilon}P}^{xy}=-\mathrm{i}\frac{mc}{\hbar^2(\epsilon_x k_{p_1}-\epsilon_y k_{p_2})}\left(1+\mathcal{S}_{\vec{\epsilon}P}^{\mathcal{A}_n}\right)+1,\ \forall\vec{\epsilon}P, n=1,\ldots,2M+1. \tag{3.140}$$

The matrix $\mathcal{S}_{\vec{\epsilon}P}^{\mathcal{A}_n}$ is still unknown, however, and we will derive an expression for it below. For this let us consider

$$\begin{aligned}\mathcal{S}_{n,(-\epsilon_x k_{p_1},\epsilon_y k_{p_2})}^{xy}=\frac{\mathcal{B}_{n,n}^{-\epsilon_x k_{p_1},\epsilon_y k_{p_2}}}{\mathcal{A}_{n,n}^{-\epsilon_x k_{p_1},\epsilon_y k_{p_2}}}&=\mathrm{i}\frac{mc}{\hbar^2(\epsilon_x k_{p_1}+\epsilon_y k_{p_2})}\left(1+\frac{\mathcal{A}_{n,n}^{\epsilon_y k_{p_2},-\epsilon_x k_{p_1}}}{\mathcal{A}_{n,n}^{-\epsilon_x k_{p_1},\epsilon_y k_{p_2}}}\right)+1\\&=\mathrm{i}\frac{mc}{\hbar^2(\epsilon_x k_{p_1}+\epsilon_y k_{p_2})}\left(1+\frac{\overrightarrow{\mathcal{R}}_{\overleftrightarrow{\vec{\epsilon}P}}^{y\mathcal{A}_{n,n}}}{\overleftarrow{\mathcal{R}}_{\vec{\epsilon}P}^{x\mathcal{A}_{n,n}}}\mathcal{S}_{\vec{\epsilon}P}^{\mathcal{A}_n}\right)+1,\end{aligned} \tag{3.141}$$

and note that

$$\mathcal{S}_{n,(-\epsilon_x k_{p_1},\epsilon_y k_{p_2})}^{xy}=\frac{\mathcal{B}_{n,n}^{-\epsilon_x k_{p_1},\epsilon_y k_{p_2}}}{\mathcal{A}_{n,n}^{-\epsilon_x k_{p_1},\epsilon_y k_{p_2}}}=\frac{\overrightarrow{\mathcal{R}}_{\vec{\epsilon}P}^{x\mathcal{B}_{n,n}}}{\overleftarrow{\mathcal{R}}_{\vec{\epsilon}P}^{x\mathcal{A}_{n,n}}}\mathcal{S}_{n,\vec{\epsilon}P}^{xy}=\frac{\overrightarrow{\mathcal{R}}_{\vec{\epsilon}P}^{x\mathcal{B}_{n,n}}}{\overleftarrow{\mathcal{R}}_{\vec{\epsilon}P}^{x\mathcal{A}_{n,n}}}\left(-\mathrm{i}\frac{mc}{\hbar^2(\epsilon_x k_{p_1}-\epsilon_y k_{p_2})}\left(1+\mathcal{S}_{\vec{\epsilon}P}^{\mathcal{A}_n}\right)+1\right). \tag{3.142}$$

From these two equations we can derive the expression for $\mathcal{S}_{\vec{\epsilon}P}^{\mathcal{A}_n}$ as

$$\mathcal{S}_{\vec{\epsilon}P}^{\mathcal{A}_n} = \frac{\left(-\mathrm{i}\frac{\hbar^2}{mc}(k_{p_1}^2 - k_{p_2}^2) - (\epsilon_x k_{p_1} + \epsilon_y k_{p_2})\right)\overrightarrow{\mathcal{R}}_{\vec{\epsilon}P}^{x\mathcal{B}_{n,n}} + \left(\mathrm{i}\frac{\hbar^2}{mc}(k_{p_1}^2 - k_{p_2}^2) - (\epsilon_x k_{p_1} - \epsilon_y k_{p_2})\right)\overleftarrow{\mathcal{R}}_{\vec{\epsilon}P}^{x\mathcal{A}_{n,n}}}{(\epsilon_x k_{p_1} - \epsilon_y k_{p_2})\overrightarrow{\mathcal{R}}_{\overleftrightarrow{\vec{\epsilon}P}}^{y\mathcal{A}_{n,n}} + (\epsilon_x k_{p_1} + \epsilon_y k_{p_2})\overrightarrow{\mathcal{R}}_{\vec{\epsilon}P}^{x\mathcal{B}_{n,n}}},$$
$$\forall \vec{\epsilon}P, n = 1, \ldots, 2M+1. \tag{3.143}$$

Similarly to the reasoning in Section 3.2, the two Bethe equations follow as

$$\overrightarrow{\mathcal{R}}_{\vec{\epsilon}P}^{y\mathcal{A}_{n,n}} = \frac{\mathcal{S}_{n,\vec{\epsilon}P}^{xy}}{\mathcal{S}_{n,(\epsilon_x k_{p_1}, -\epsilon_y k_{p_2})}^{xy}}\overleftarrow{\mathcal{R}}_{\vec{\epsilon}P}^{y\mathcal{B}_{n,n}}, \tag{3.144}$$

$$\overrightarrow{\mathcal{R}}_{\vec{\epsilon}P}^{y\mathcal{A}_{n,n}} = \frac{\mathcal{S}_{\vec{\epsilon}P}^{\mathcal{A}_n}}{\mathcal{S}_{\epsilon_x k_{p_1}, -\epsilon_y k_{p_2}}^{\mathcal{A}_n}}\overleftarrow{\mathcal{R}}_{\overleftrightarrow{\vec{\epsilon}P}}^{x\mathcal{A}_{n,n}}. \tag{3.145}$$

We can also obtain an expression for the barrier scattering matrix by dividing Eq. (3.122) by $\mathcal{A}_{n,l}^{\epsilon_x k_{p_1}, \epsilon_y k_{p_2}}$ to give

$$\overleftarrow{\mathcal{S}}_{\vec{\epsilon}P}^{x\mathcal{A}_{n,l}} = \frac{\mathcal{A}_{n+1,l}^{\vec{\epsilon}P}}{\mathcal{A}_{n,l}^{\vec{\epsilon}P}} = 1 - \mathrm{i}\frac{mh_n}{\epsilon_x k_{p_1}\hbar^2}\left(1 + \mathrm{e}^{-2\mathrm{i}\epsilon_x k_{p_1} z_n}\overleftarrow{\mathcal{R}}_{\vec{\epsilon}P}^{x\mathcal{A}_{n,l}}\right),$$
$$n = 1, \ldots, 2M,\ l = n+1, \ldots, 2M+1. \tag{3.146}$$

Analogously, we obtain all remaining barrier scattering matrices as

$$\overleftarrow{\mathcal{S}}_{\vec{\epsilon}P}^{y\mathcal{B}_{j,n}} = \frac{\mathcal{B}_{j,n+1}^{\vec{\epsilon}P}}{\mathcal{B}_{j,n}^{\vec{\epsilon}P}} = 1 - \mathrm{i}\frac{mt_n}{\epsilon_y k_{p_2}\hbar^2}\left(1 + \mathrm{e}^{-2\mathrm{i}\epsilon_y k_{p_2} z_n}\overleftarrow{\mathcal{R}}_{\vec{\epsilon}P}^{y\mathcal{B}_{j,n}}\right),$$
$$n = 1, \ldots, 2M,\ j = n+1, \ldots, 2M+1, \tag{3.147}$$

$$\overrightarrow{\mathcal{S}}_{\vec{\epsilon}P}^{x\mathcal{B}_{n,l}} = \frac{\mathcal{B}_{n+1,l}^{\vec{\epsilon}P}}{\mathcal{B}_{n,l}^{\vec{\epsilon}P}} = \frac{\epsilon_x k_{p_1}}{\epsilon_x k_{p_1} + \mathrm{i}\frac{mh_n}{\epsilon_x k_{p_1}\hbar^2}\left(1 + \mathrm{e}^{-2\mathrm{i}\epsilon_x k_{p_1} z_n}\overrightarrow{\mathcal{R}}_{\vec{\epsilon}P}^{x\mathcal{B}_{n+1,l}}\right)},$$
$$n = 1, \ldots, 2M,\ l = 1, \ldots, n, \tag{3.148}$$

$$\overrightarrow{\mathcal{S}}_{\vec{\epsilon}P}^{y\mathcal{A}_{j,n}} = \frac{\mathcal{A}_{j,n+1}^{\vec{\epsilon}P}}{\mathcal{A}_{j,n}^{\vec{\epsilon}P}} = \frac{\epsilon_y k_{p_2}}{\epsilon_y k_{p_2} + \mathrm{i}\frac{mt_n}{\epsilon_y k_{p_2}\hbar^2}\left(1 + \mathrm{e}^{-2\mathrm{i}\epsilon_y k_{p_2} z_n}\overrightarrow{\mathcal{R}}_{\vec{\epsilon}P}^{y\mathcal{A}_{j,n+1}}\right)},$$
$$n = 1, \ldots, 2M,\ j = 1, \ldots, n. \tag{3.149}$$

Let us now write out the necessary condition of integrability of this model: the Yang–Baxter relations. There are two ways of decomposing the three-body scattering event of the particles and one barrier as a sequence of two-body scattering events. In the first case, the particles first scatter with each other, and then one by one scatter with their barrier

$$\frac{\mathcal{A}_{n+1,n+1}^{\vec{\epsilon}P}}{\mathcal{B}_{n,n}^{\vec{\epsilon}P}} = \frac{\mathcal{B}_{n+1,n}^{\vec{\epsilon}P}}{\mathcal{B}_{n,n}^{\vec{\epsilon}P}} \times \frac{\mathcal{B}_{n+1,n+1}^{\vec{\epsilon}P}}{\mathcal{B}_{n+1,n}^{\vec{\epsilon}P}} \times \frac{\mathcal{A}_{n+1,n+1}^{\vec{\epsilon}P}}{\mathcal{B}_{n+1,n+1}^{\vec{\epsilon}P}}. \tag{3.150}$$

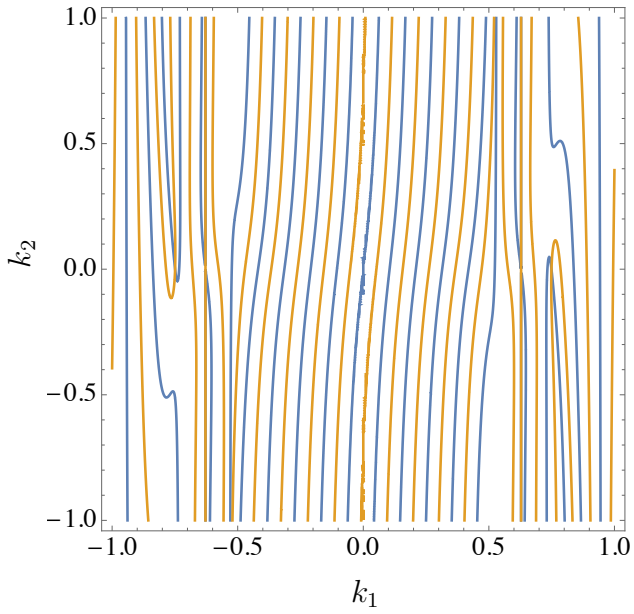

Figure 3.5: Plot of the curves given by the imaginary and real parts of the Yang–Baxter equation for the first barrier in Eq. (3.152). The barrier height is set to $h = 1$. The colored curves intersect only when one of the quasi-momenta is zero. Here I use natural units $\hbar = m = 1$, the size of the box is $L = 10$ and $c = 1$.

In the second case, the particles first scatter with their barrier, and then scatter with each other

$$\frac{\mathcal{A}^{\vec{\epsilon}P}_{n+1,n+1}}{\mathcal{B}^{\vec{\epsilon}P}_{n,n}} = \frac{\mathcal{A}^{\vec{\epsilon}P}_{n,n}}{\mathcal{B}^{\vec{\epsilon}P}_{n,n}} \times \frac{\mathcal{A}^{\vec{\epsilon}P}_{n,n+1}}{\mathcal{A}^{\vec{\epsilon}P}_{n,n}} \times \frac{\mathcal{A}^{\vec{\epsilon}P}_{n+1,n+1}}{\mathcal{A}^{\vec{\epsilon}P}_{n,n+1}}. \tag{3.151}$$

Both this cases have to be equal for the model to be solvable, which gives us the condition

$$\left(\mathcal{S}^{xy}_{n,\vec{\epsilon}P}\right)^{-1} \overrightarrow{\mathcal{S}}^{y\mathcal{A}_{n,n}}_{\vec{\epsilon}P} \overleftarrow{\mathcal{S}}^{x\mathcal{A}_{n,n+1}}_{\vec{\epsilon}P} = \overrightarrow{\mathcal{S}}^{x\mathcal{B}_{n,n}}_{\vec{\epsilon}P} \overleftarrow{\mathcal{S}}^{y\mathcal{B}_{n+1,n}}_{\vec{\epsilon}P} \left(\mathcal{S}^{xy}_{n+1,\vec{\epsilon}P}\right)^{-1}, \ n = 1, \ldots, M. \tag{3.152}$$

Although the system does not have *true* three-body interactions, mathematically when two particles scatter with a barrier at the same time, one of them scatters with the barrier of finite height, and the other with the barrier of zero height. Unfortunately, the Yang–Baxter equations are not generally satisfied in this system if the interaction between the particle is finite (for example, see Fig. 3.5). This means that the system is also not solvable for finite interactions even when the particles see different effective potential due to the fact that three-body scattering events cannot be decomposed into series of two-body scattering events (the system is diffractive).

In the next section I will consider a single-particle system with multiple barriers where three-body scattering events are fully absent.

3.5 Derivations of a single particle AFKP

In previous sections I have shown that many-body systems with two or more barriers are not solvable in the Bethe ansatz sense due to the presence of diffractive three-body

scattering. Instead of considering relatively few barriers and many particles, in this section I will analyse a finite system with single particle but many point-like barriers - the arbitrary finite Kronig–Penney model (AFKP). All barriers in this system can have arbitrary positions and heights, and their number is also specified as a parameter. The finite version of the well-known Kronig–Penney model is a special case of this model with the barriers positioned equidistantly and having equal heights. A more general framework of solving models with fixed point-like scatterers using the Green's functions was presented by Sroczyńska *et al.* [153], and below I will analyze the AFKP model using the Bethe ansatz approach.

Let us consider a single particle in an infinite box potential of size L with M δ-barriers of arbitrary heights $\vec{h} = (h_1, .., h_M)$ and arbitrary positions $\vec{y} : y_1 < ... < y_M$ within the box $x \in [-\frac{L}{2}, \frac{L}{2}]$ (see Fig. 3.6). The Hamiltonian of the problem reads

$$\hat{H} = -\frac{\hbar^2}{2m}\frac{\mathrm{d}^2}{\mathrm{d}x^2} + \sum_{n=1}^{M} h_n \delta(x - y_n), \tag{3.153}$$

and the corresponding Schrödinger equation becomes

$$-\frac{\hbar^2}{2m}\frac{\mathrm{d}^2\Psi(x)}{\mathrm{d}x^2} + \sum_{n=1}^{M} h_n \delta(x - y_n)\Psi(x) = E\Psi(x). \tag{3.154}$$

The procedure below is identical to Sections 3.3 3.4, but is worth going over again due to changes in notation.

Due to point-like nature of the barriers, we can rewrite Eq. (3.154) as a free particle equation

$$-\frac{\hbar^2}{2m}\frac{\mathrm{d}^2\Psi(x)}{\mathrm{d}x^2} = E\Psi(x), \tag{3.155}$$

with the appropriate boundary conditions at the edges of the box and at the positions of the δ-barriers. At the edges of the box the wave function must go to zero

$$\Psi(x = \pm\frac{L}{2}) = 0, \tag{3.156}$$

and at the positions of the δ-potentials the derivative of the wave function must have a discontinuity

$$\left(\frac{\mathrm{d}}{\mathrm{d}x}\bigg|_{x=y_n+0} - \frac{\mathrm{d}}{\mathrm{d}x}\bigg|_{x=y_n-0} - \frac{2mh_n}{\hbar^2}\bigg|_{x=y_n}\right)\Psi(x) = 0,\ n = 1, ..., M, \tag{3.157}$$

while the wave function itself still has to be continuous

$$\Psi(x)|_{x=y_n-0} = \Psi|_{x=y_n+0},\ n = 1, ..., M. \tag{3.158}$$

The solutions of the time-independent Schrödinger equation can be represented as superposition of plane waves in each segment $\mathcal{D}_j : x \in [y_{j-1}, y_j]$

$$\Psi(x) = \sum_{j=1}^{M+1} \chi_j(x)\Theta(\mathcal{D}_j) = \sum_{j=1}^{M+1} \left(\mathcal{A}_j^k e^{ikx} + \mathcal{A}_j^{-k} e^{-ikx}\right)\Theta(\mathcal{D}_j), \tag{3.159}$$

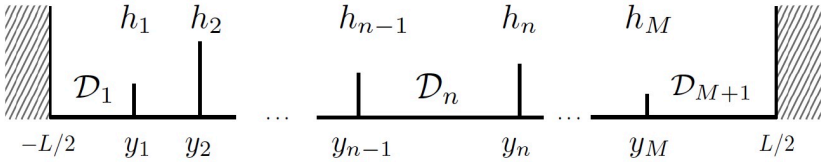

Figure 3.6: Schematic of the finite arbitrary KP model

where $\Theta(\mathcal{D}_j) = \theta(x - y_{j-1})\theta(y_j - x)$, $\theta(x)$ is the Heaviside theta function and $y_0 = -\frac{L}{2}$ and $y_{M+1} = \frac{L}{2}$. Each of the expressions under the sum is the piece of the wave function corresponding to the situation where the particle is in the j-th well ($y_{j-1} \leq x < y_j$).

As shown in section 3.2, the Bethe ansatz approach consists of finding expressions for the coefficients $\mathcal{A}_j^k$ and $\mathcal{A}_j^{-k}$, and constructing the Bethe equation for the quasi-momenta k. The energy is then simply

$$E = \frac{\hbar^2 k^2}{2m}. \tag{3.160}$$

Let us first consider the infinite wall boundary conditions. After substituting the ansatz in Eq. (3.159) into Eq. (3.156), we get an expression for the first and the last elements of the reflection matrix as

$$\overleftarrow{\mathcal{R}}_1 = \frac{\mathcal{A}_1^{-k}}{\mathcal{A}_1^k} = -e^{-ikL}, \tag{3.161}$$

$$\overrightarrow{\mathcal{R}}_{M+1} = \frac{\mathcal{A}_{M+1}^{-k}}{\mathcal{A}_{M+1}^k} = -e^{ikL}. \tag{3.162}$$

The scattering condition in Eq. (3.157) at the n-th barrier gives

$$\left(\frac{\mathrm{d}\chi_n(x)}{\mathrm{d}x}\bigg|_{x=y_n} - \frac{mh_n}{\hbar^2}\chi_n(y_n)\right) - \left(\frac{\mathrm{d}\chi_{n-1}(x)}{\mathrm{d}x}\bigg|_{x=y_n} - \frac{mh_n}{\hbar^2}\chi_{n-1}(y_n)\right) = 0, \tag{3.163}$$

which becomes

$$\begin{aligned} &\mathcal{A}_{n+1}^k\left(ik - \frac{mh_n}{\hbar^2}\right) - \mathcal{A}_{n+1}^{-k}e^{-i2y_nk}\left(ik + \frac{mh_n}{\hbar^2}\right) \\ &-\mathcal{A}_n^k\left(ik + \frac{mh_n}{\hbar^2}\right) - \mathcal{A}_n^{-k}e^{-i2y_nk}\left(-ik + \frac{mh_n}{\hbar^2}\right) = 0. \end{aligned} \tag{3.164}$$

On the other hand, the continuity condition in Eq. (3.158) gives the relation

$$\mathcal{A}_{n+1}^k + \mathcal{A}_{n+1}^{-k}e^{-i2y_nk} - \mathcal{A}_n^k - \mathcal{A}_n^{-k}e^{-i2y_nk} = 0. \tag{3.165}$$

After substituting the expressions for $\mathcal{A}_{n+1}^{-k}$ and $\mathcal{A}_{n+1}^k$ obtained from Eq. (3.165), we arrive at a recursive expression for the $n+1$ element of the reflection matrix

$$\overleftarrow{\mathcal{R}}_{n+1} = \frac{\mathcal{A}_{n+1}^{-k}}{\mathcal{A}_{n+1}^k} = \frac{-\frac{mh_n}{\hbar^2}e^{i2y_nk} + [ik - \frac{mh_n}{\hbar^2}]\overleftarrow{\mathcal{R}}_n}{[ik + \frac{mh_n}{\hbar^2}] + \frac{mh_n}{\hbar^2}e^{-i2y_nk}\overleftarrow{\mathcal{R}}_n}, \tag{3.166}$$

where $\overleftarrow{\mathcal{R}}_n = \frac{\mathcal{A}_n^{-k}}{\mathcal{A}_n^k}$.

On the other hand, the expression for $\frac{\mathcal{A}_{n+1}^{-k}}{\mathcal{A}_{n+1}^k}$ can be written as

$$\overrightarrow{\mathcal{R}}_n = \frac{\frac{mh_n}{\hbar^2}e^{i2y_nk} + [ik + \frac{mh_n}{\hbar^2}]\overrightarrow{\mathcal{R}}_{n+1}}{[ik - \frac{mh_n}{\hbar^2}] - \frac{mh_n}{\hbar^2}e^{-i2y_nk}\overrightarrow{\mathcal{R}}_{n+1}}. \tag{3.167}$$

The two equations (3.166) and (3.167) correspond to the two ways of inverting the sign of quasi-momentum k: by reflecting the particle against the left and the right walls. Thus, the n-th element of the reflection matrix has two forms, which have to be equivalent, leading to

$$\frac{-\frac{mh_{n-1}}{\hbar^2}e^{i2y_{n-1}k} + [ik - \frac{mh_{n-1}}{\hbar^2}]\overleftarrow{\mathcal{R}}_{n-1}}{[ik + \frac{mh_{n-1}}{\hbar^2}] + \frac{mh_{n-1}}{\hbar^2}e^{-i2y_{n-1}k}\overleftarrow{\mathcal{R}}_{n-1}} = \frac{\frac{mh_n}{\hbar^2}e^{i2y_nk} + [ik + \frac{mh_n}{\hbar^2}]\overrightarrow{\mathcal{R}}_{n+1}}{[ik - \frac{mh_n}{\hbar^2}] - \frac{mh_n}{\hbar^2}e^{-i2y_nk}\overrightarrow{\mathcal{R}}_{n+1}},\ n = 2, ..., M \tag{3.168}$$

The $M-1$ equations of the form Eq. (3.168) are the Bethe equations which define the allowed quasi-momenta k and thus, the energy spectrum of the problem. First, let us prove that all these Bethe equations are equivalent.

We can represent the process of reflecting a particle as a sequence of scattering events at the barriers $\mathcal{S}_j[\pm k] = \frac{\mathcal{A}_j^{\pm k}}{\mathcal{A}_{j-1}^{\pm k}}$ and a reflection against the left $\overleftarrow{\mathcal{R}}_1$ or right $\overrightarrow{\mathcal{R}}_{M+1}$ wall. Let us consider the particle being reflected from the rightmost well. Then the Bethe equation can be written as

$$\prod_{j=1}^{M}\mathcal{S}_j[-k]^{-1} \times \overleftarrow{\mathcal{R}}_1 \times \prod_{j=M+1}^{2}\mathcal{S}_j[k] = \overrightarrow{\mathcal{R}}_{M+1}. \tag{3.169}$$

It is easy to see that by multiplying the right hand side of this equation by inverse scattering matrices in an appropriate sequence one can reconstruct similar equations for the situations where the particle is in all other wells.

Consequently, we need only one Bethe equation for a single variable k, for example

$$\frac{-\frac{mh_M}{\hbar^2}e^{i2y_Mk} + [ik - \frac{mh_M}{\hbar^2}]\overleftarrow{\mathcal{R}}_M}{[ik + \frac{mh_M}{\hbar^2}] + \frac{mh_M}{\hbar^2}e^{-i2y_Mk}\overleftarrow{\mathcal{R}}_M} = -e^{ikL}. \tag{3.170}$$

By unwrapping the recursive expression Eq. (3.166), we can therefore construct the Bethe equations for any value of the parameters $m, L, \vec{y}$ and $\vec{h}$.

From eqs. (3.164) and (3.165) we can also obtain recursive expression for the elements of the scattering matrix as

$$\mathcal{S}_{n+1}[k] = \frac{\mathcal{A}_{n+1}^k}{\mathcal{A}_n^k} = 1 + \frac{i}{k}\frac{mh_n}{\hbar^2}\left(1 + e^{-i2y_nk}\overleftarrow{\mathcal{R}}_n\right),\ n = 1, ..., M \tag{3.171}$$

We now have everything to express all coefficients of the ansatz wave function in terms

of normalization constant $\mathcal{A}_1^k$ as

$$\mathcal{A}_n^{-k} = \overleftarrow{\mathcal{R}}_n \times \mathcal{A}_n^k, \tag{3.172}$$

$$\mathcal{A}_n^k = \prod_{j=1}^{n-1} \mathcal{S}_j[k] \times \mathcal{A}_1^k, \tag{3.173}$$

$$n = 1, ..., M+1. \tag{3.174}$$

Eq. (3.168) gives us an expression for the Bethe equation for the quasi-momentum k depending on parameters $m, L, \vec{y}$ and $\vec{h}$. After algebraic simplification this equation takes the very simple form

$$0 = \sum_{n=0}^{N} \xi_n k^{N-n}, \tag{3.175}$$

where

$$\xi_n = \sum_{(p_1,..,p_n),1\leq p_i\leq M} \left(\prod_{j=1}^{n} h_{p_j}\right) \left(\prod_{j=1}^{n+1} \sin\left[k(y_{p_j} - y_{p_{j-1}})\right]\right), \tag{3.176}$$

with $y_{p_0} = -\frac{L}{2}$ and $y_{p_{n+1}} = \frac{L}{2}$. Here $(p_1, .., p_n), 1 \leq p_i \leq M$ is a set of all possible ways to pick n barrier numbers out of M. The coefficients of the ansatz in Eq. (3.159) then become

$$\mathcal{A}_n^k = e^{ik\frac{L}{2}} \left(1 + \sum_{j=1}^{n-1} \left(\frac{2m}{k\hbar^2}\right)^j \Xi_j^n(k)\right) \mathcal{A}_1^k, \tag{3.177}$$

$$\mathcal{A}_n^{-k} = -\left(\mathcal{A}_n^k\right)^*, \tag{3.178}$$

where

$$\Xi_j^n = \left(\frac{2m}{k\hbar^2}\right)^j \times \sum_{(p_1,..,p_j),1\leq p_i\leq n-1} e^{-ik(y_{p_j}+\frac{L}{2})} \prod_{k=1}^{j} h_{p_k} \sin\left[k(y_{p_k} - y_{p_{k-1}})\right], \tag{3.179}$$

with $y_{p_0} = -\frac{L}{2}$. If we fix $\mathcal{A}_1^k = 1$, then the normalization constant becomes

$$\begin{aligned}\mathcal{N} = \Bigg[\sum_{n=1}^{M+1} \Bigg(& 2|\mathcal{A}_n^k|^2 (y_n - y_{n-1}) \\ & - \frac{\sin 2ky_n - \sin 2ky_{n-1}}{2k} (\Re\left(\mathcal{A}_n^k\right)^2 - \Im\left(\mathcal{A}_n^k\right)^2) \\ & - \frac{\cos 2ky_n - \cos 2ky_{n-1}}{k} \Re\mathcal{A}_n^k \Im\mathcal{A}_n^k \Bigg)\Bigg]^{-\frac{1}{2}},\end{aligned}$$

where $\Im\mathcal{A}_n^k$ and $\Re\mathcal{A}_n^k$ are imaginary and real parts of $\mathcal{A}_n^k$.

In this chapter I have shown that a many-body system with multiple point-like barriers in general cannot be solved if the particle interactions are finite. Instead I have derived a Bethe ansatz solution of a single particle in a box with an arbitrary number of barriers which can be placed at arbitrary positions within the box and have

arbitrary heights (AFKP model). I have also presented a compact general form for the Bethe equation and the wavefunction with the heights and positions of the barriers as external parameters. This solution is extremely flexible and ready to be used in analytical studies of various one-dimensional systems. However, the combinatorial nature of the expressions of the solution makes it not practicle for large numbers of barriers. This is especially relevant for the reconstruction of the wavefunctions.

In the next chapter I will apply the obtained solution of the AFKP model in order to study the appearance of topologically non-trivial states.

Chapter 4

Topological properties of low-dimensional systems

In the previous chapter I have obtained an analytical expression for the eigenstates of the arbitrary finite Kronig–Penney model, as well as the transcendental relation which gives the allowed quasi-momenta. In this model an arbitrary number of barriers (M) can be placed at arbitrary positions inside the box and have arbitrary heights. This gives $2M$ external parameters which can be freely tuned, allowing me to consider a wide range of interesting systems. In this chapter I will take advantage of this flexibility in order to study the appearance of topologically non-trivial states in the AFKP.

4.1 Introduction to topological states

In 1980 von Klitzing and his collaborators were conducting an experiment with an ultracold two-dimensional electron gas in the presence of a strong magnetic field. While measuring the Hall condutivity of the system across the sample, they discovered that it had unexplained plateaus at $\sigma_H = n\frac{e^2}{h}$, where e is the charge of the electron, h is the Planck constant and n is an integer number [154]. Additionally, the conductivity was significant only in one direction while being neglible in the other. Later the same quantized Hall conductivity phenomenon was discovered in other two-dimensional systems with various material properties and degrees of impurity [155, 156]. This effect is now widely known as the quantum Hall effect (QHE), and it arises in two-dimensional electron gas systems with an external magnetic field due to the quantization of the energy levels of the electrons, called Landau levels [154, 157–159]. However, the robustness of the QHE originates from the topological properties of the system [157, 159–162], where the gauge invariance of the magnetic vector potential ensures that the quantization of the Hall conductivity does not depend on the details of the underying material. All current in such a system is carried by the highly ordered and topologically protected edge states, while the disorder in the bulk system leads to localization of the electrons, preventing the conduction. Later, the fractional quantum Hall effect was discovered, and the additional fractional plateaus were explained by taking the interactions between the electrons into account [163, 164].

Another remarkable phenomenon arises in a bulk 2D lattice system if the magnetic

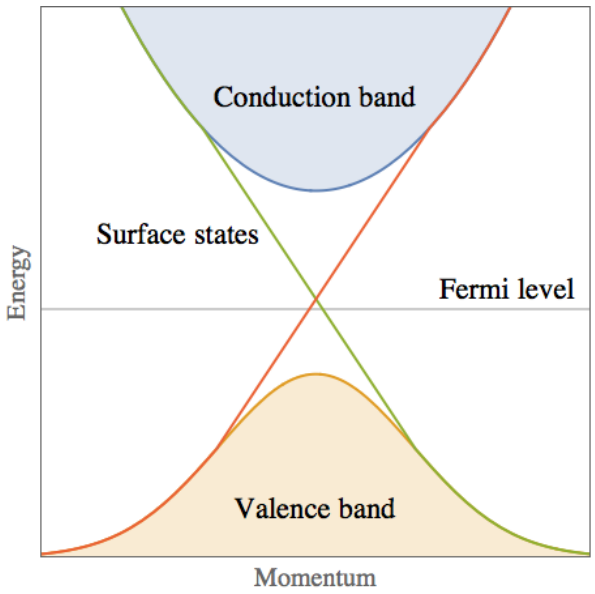

Figure 4.1: The band structure of an ideal finite topological insulator. The insulating gap between the valence and the conducting bands is breached by the conducting surface states.

flux through the unit cell is adiabatically changed. In this case the energy spectrum exhibits a fractal-like splitting for rational values of magnetic flux per unit cell values, forming the famous Hofstadter butterfly [165].

4.2 Edge states

The edge states in a finite system which give rise to the QHE are themselves a manifestation of the topological properties of the bulk system. They are one of the most characteristic features of topological insulators, which are materials with non-trivial topological order that are insulators within the bulk but have stable conducting states on the surface.

A typical band structure of a topological insulator is shown Fig. 4.1. The conduction and the valence bands are separated by an insulating gap, but there are two edge states with opposite velocities which cross the gap and connect the two bands. If the edge states with opposite velocities have a non-zero coupling, the crossing becomes avoided, forming a mobility gap.

In order to characterize and quantify these unusual insulators, the fundamental mathematical concept of topological invariants is used, such as the first Chern number. It is related to the Berry phase and defined as

$$c = \frac{1}{2\pi} \int_k \mathrm{d}k \int_\delta \mathrm{d}\delta \left(\partial_k A_\delta - \partial_\delta A_k \right), \tag{4.1}$$

where k is the quasi-momentum in x direction and δ is the lattice shift. $A_{k_1} = i\langle \phi(k_1, k_2) | \partial_{k_1} \phi(k_1, k_2) \rangle$ and $A_{k_2} = i\langle \phi(k_1, k_2) | \partial_{k_2} \phi(k_1, k_2) \rangle$ are the Berry connections with $\phi(k_1, k_2)$ being the occupied Bloch state [166, 167].

The relation of the first Chern number and the quantization of the Hall conductance was first proven by Thouless *et al.* [160], and Hatsugai has further connected it to the phase obtained by an edge state while crossing the gap [168].

Edge states appear in finite systems, where in the corresponding periodic system the excitation bands in the first Brillouin zone have different topology (and thus different Chern numbers). Even though topological effects are generally observed in higher dimensional systems, it has been shown that in some one-dimensional systems additional parameters of the system can be used as a virtual second dimension - a *superspace* [169]. In two dimensions a nontrivial topology is marked by a nonzero first Chern number [166, 167], and this quantity can also be used to characterize the topology of a 1D system with a superspace [20, 21]. A discrete model with an on-site energy which is periodically modulated [20], or a system with a trigonometric external potential [21] are examples of nontrivial topologies studied in one dimension with a superspace, and they observe the formation of the edge states which arise from a nontrivial topology proven by a non-zero Chern invariant.

4.3 Topological states in the AFKP model

In this section I will demonstrate how the arbitrary finite Kronig–Penney model can support the existence of topologically non-trivial states. As discussed in Sec. 3.5, the AFKP model is a single-particle system consisting of an infinite square well and an arbitrary number of point-like scatterers of arbitrary positions and heights within the box. The Hamiltonian of the system reads

$$\hat{H} = -\frac{\hbar^2}{2m}\frac{\mathrm{d}^2}{\mathrm{d}x^2} + \sum_{n=1}^{M} h_n \delta(x - y_n). \tag{4.2}$$

The allowed quasi-momenta of the particle are then given by the Bethe equation (3.175), and the wavefunction has a form described in equations (3.159) and (3.177). The AFKP model allows for a great flexibility as the external potential has $2M$ free parameters

$$V(x|\vec{y},\vec{h}) = \sum_{n=1}^{M} h_n \delta(x - y_n), \tag{4.3}$$

namely the positions ($\vec{y}$) and the heights ($\vec{h}$) of the barriers. In fact, some of these parameters can be used as extra adiabatic dimensions - the *superspaces* - to allow higher-dimensional physics to manifest itself in the model. A few examples of such superspaces, i.e. the ones we are going to consider in this work, are described below.

- After fixing the barriers at equal distance from each other, one can use the total shift of the lattice with respect to the walls of the box as a second adiabatic dimension. This case is discussed in more detail in 4.3.1.

- It is also possible to arrange all barriers symmetrically around the center of the box and then use the distance between the barriers as a superspace (this case is discussed in 4.3.2).

- One can modulate the heights of equidistant barriers with a periodic function, using the period of this function as a superspace. I discuss this case in 4.3.3.

4.3.1 Edge states in shifted lattice

I first consider M equidistant barriers in a box of size L. Denoting the shift of this lattice with respect to the walls of the box as Δ, the positions of the barriers are

$$y_n = -\frac{L}{2} + \left(n + \frac{\Delta - 1}{2}\right)\frac{L}{M},\ n = 1, \ldots, M. \tag{4.4}$$

The values of the shift $\Delta = -1$ and $\Delta = 1$ correspond to the leftmost and the rightmost barriers coinciding with the left or the right wall. For now we will consider all barriers to be of the same height. If we calculate the quasi-momenta as functions of $\Delta \in [0, 1]$, we observe the appearance of in-gap states within the bandgaps in the spectrum (see Fig. 4.2(a)). The corresponding energy spectrum can be trivially calculated as $k^2/2$ and is not shown here. The probability density of the lowest two edge states is shown in Fig. 4.2 (b) and (c) as a function of Δ. One can see that the wavefunction of the first edge state is localized strongest for the values of the shift where the quasi-momentum lies in the middle of the band gap ($\Delta = \pm\frac{1}{2}$), showing that the in-gap states mostly populate the edges, and becomes delocalized for the shift values where the quasi-momentum of the edge states merge with the bands, e.g. for $\Delta \to 0, \pm 1$. The slope of the quasi-momentum of the edge states as a function of the shift Δ correspond to their velocities: positive slope results in a positive velocity, and negative slope implies negative velocity. From Fig. 4.2 (b) and (c) one can see that the edge states which are traveling in opposite directions appear on the opposite sides of the box, indicating that these boundary states are chiral, which suggests the presence of nontrivial topology. In order to prove that the edge state in the system are indeed nontrivial, I numerically calculate the Chern numbers of the first two energy bands (corresponding to the first two quasi-momentum bands in Fig. 4.2 (a)) in the system with periodic boundary conditions using the method described in [170]. More details on this are given in Section 5.3. The results of my numerical calculation of the Chern numbers are shown in Fig. 4.2 for the first two energy bands. In the first gap we have two edge modes, with positive and negative velocities, located on the opposite sides of the box and corresponding to $c_1 = 1$. The number of edge states in the gap is related to the sum of the Chern numbers of the bands up to the given gap. In the second gap the number of edge modes becomes two for both sides, reflecting a total Chern number $c_2 = 2$, and so on. These results agree with the recent study in a continuous cosine lattice [21].

The existence of the edge states in the single-particle AFKP model also manifests itself in the asymmetry of the probability density of a spin-polarized ideal Fermi gas and, consequently, Tonks–Girardeau gas (see Fig. 4.3). It is easy to see that the single particle probability density for a gas with Fermi energy just below the edge state (8 particles) has lower density at the edges of the box than compared to a gas with Fermi energy which is equal to the edge state energy(9 particles).

As a more complicated case I will now consider a AFKP model with equidistant barriers of two alternating heights (see Fig. 4.4) and shift Δ as in previous case. As

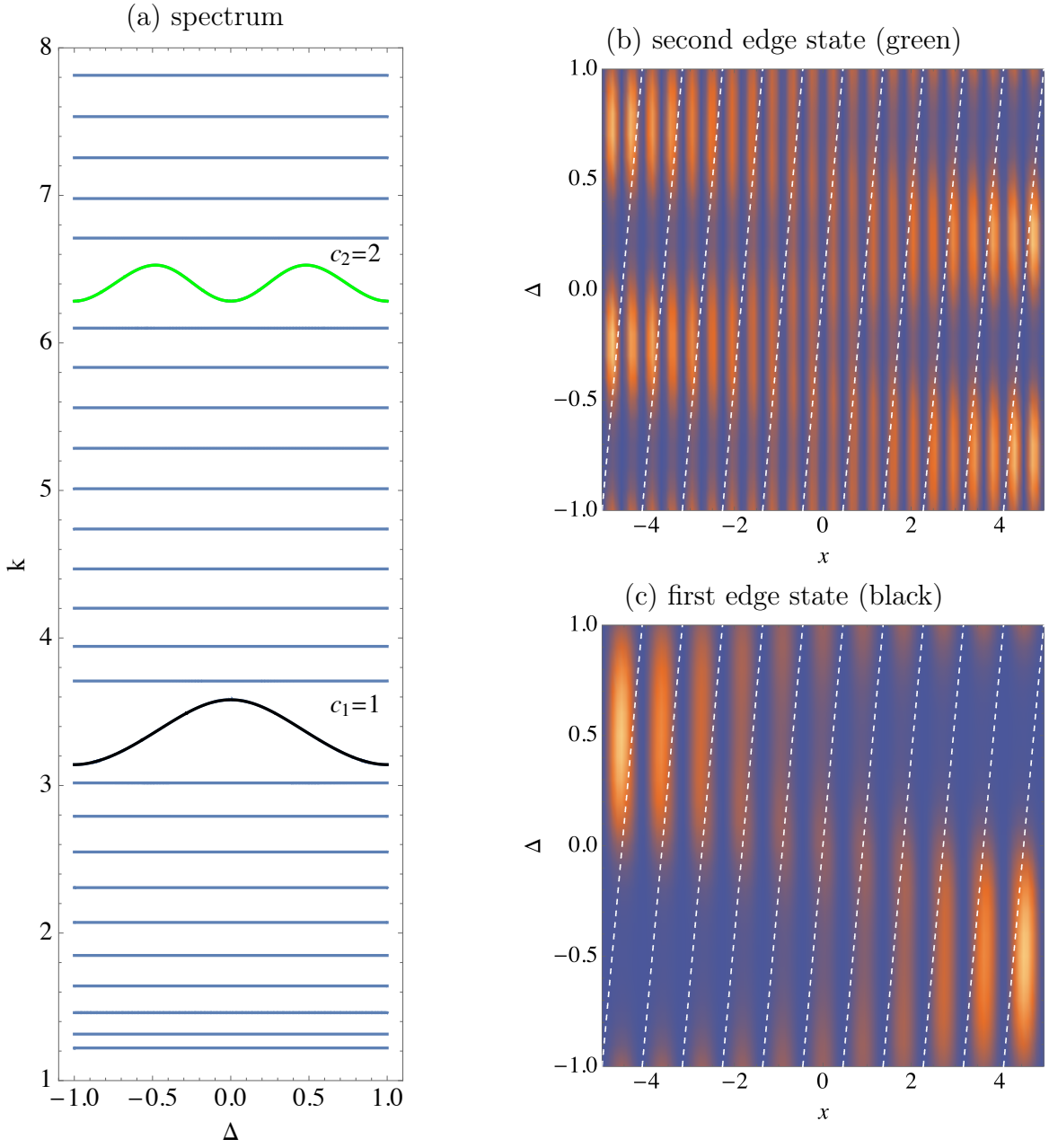

Figure 4.2: (a) Momentum spectrum as a function of the shift Δ for a system of 11 equidistant barriers of height $h = 0.4$ in a box of size $L = 11$. The green and black lines indicate the first two edge states with quantum numbers 22 and 11, whose densities are shown in (b) and (c), respectively. The dashed white lines indicate the positions of the scatterers. Here natural units are used ($\hbar = m = 1$). The numbers $c_1 = 1$ and $c_2 = 2$ in the gaps are the calculated total Chern numbers of the corresponding energy bands below the gap.

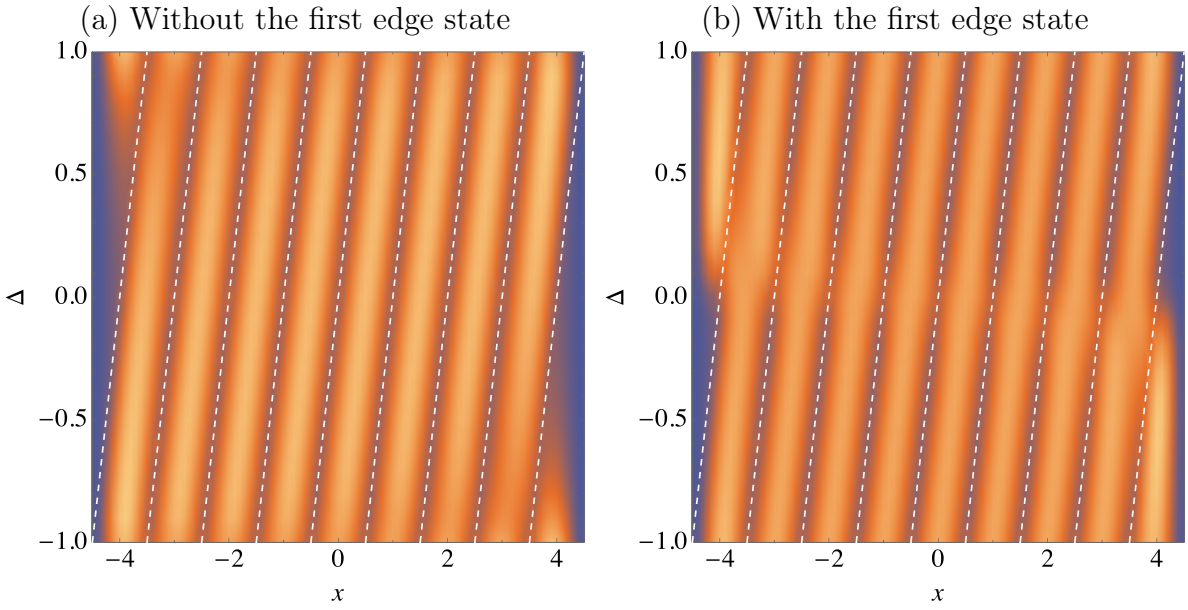

Figure 4.3: The single particle probability density of the ideal TG gas for the energy below (8 particles) (a) and equal to (9 particles) (b) the first edge state energy. The number of barriers is $M = 9$ and the box size $L = 10$.

expected, additional gaps open in the quasimomentum spectrum, but the edge states are still present, hinting that their existence is robust against variations in the barriers' heights. Indeed, even if the barriers are set to be of random heights, the edge states still survive. An example of the quasimomentum spectrum and two lowest-lying edge states in a model with random barrier heights is shown in Fig. 4.5.

4.3.2 Edge states in spreading lattice

Next I will use the AFKP model with the lattice constant as a superspace instead of the shift. After fixing the barriers to be of equal height and centered in the box, I use the distance γ between the barriers as a second dimension (see Fig. 4.6). The positions of the barriers then become

$$y_n = -\frac{L}{2} + \frac{L}{2}(1-\gamma) + \frac{L}{M-1}\gamma(n-1),\ n = 1, \ldots, M. \tag{4.5}$$

By solving the Bethe equation for $\gamma \in [\frac{M-1}{M+1}, 1]$ we obtain an asymmetric quasimomentum spectrum with double gap states appearing in the band gaps (see Fig. 4.7 (a)). After looking closer at these gap states and plotting their density (Fig. 4.7 (b)), it becomes easy to see that these are fully symmetric edge states. The two edge states become almost degenerate in the middle of the gap and separate when approaching the bands. If we break the symmetry of the system by taking random heights of the barriers, the symmetric edge states in the gap split further and are no longer symmetric, bunching either at the left or the right edge of the box (Fig. 4.8).

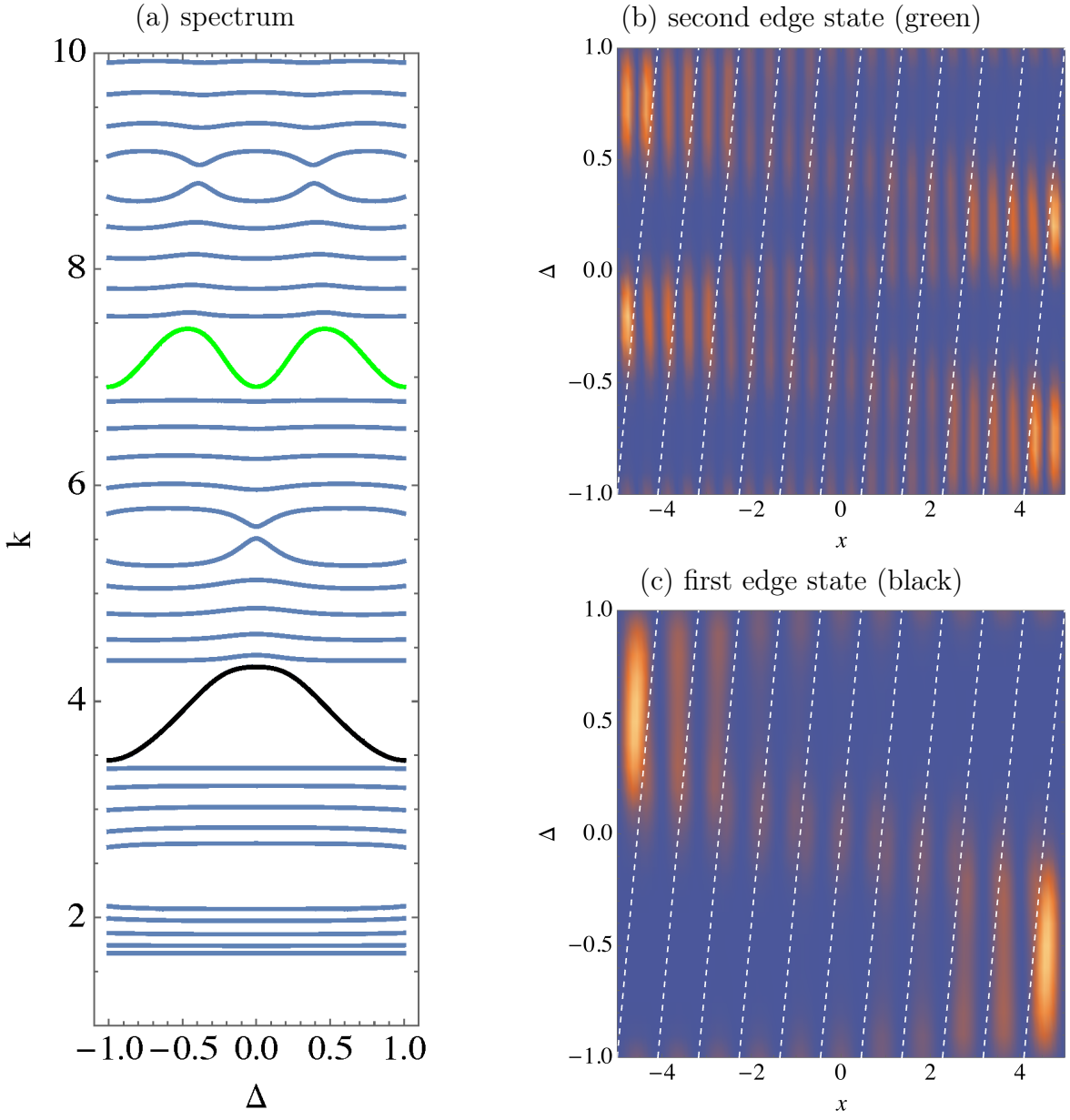

Figure 4.4: Same as Fig. 4.2, but for a system of 11 equidistant barriers of alternating heights $h = \{0.4, 1.4\}$.

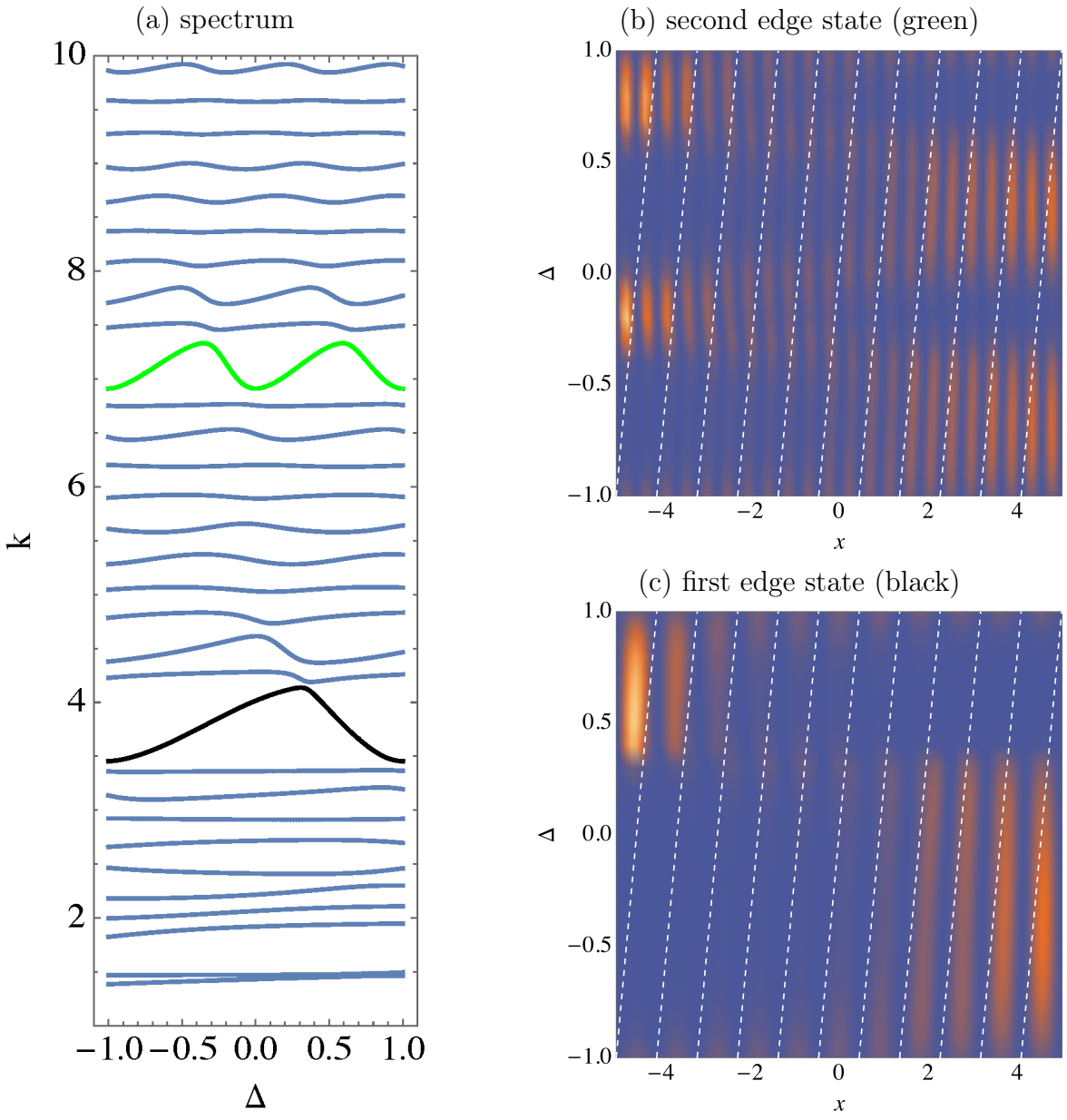

Figure 4.5: Same as Fig. 4.2, but for an example of a system of 11 equidistant barriers of random heights varying from $h_{\min} = 0.1$ to $h_{\max} = 1.4$.

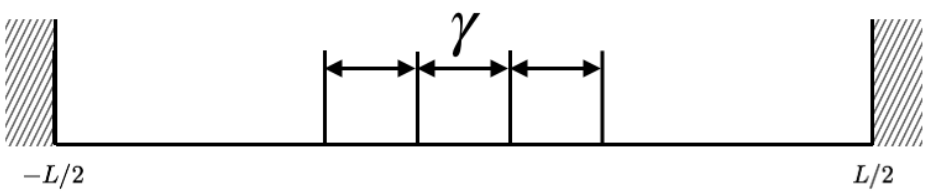

Figure 4.6: Schematic of the AFKP model with the lattice constant as the superspace.

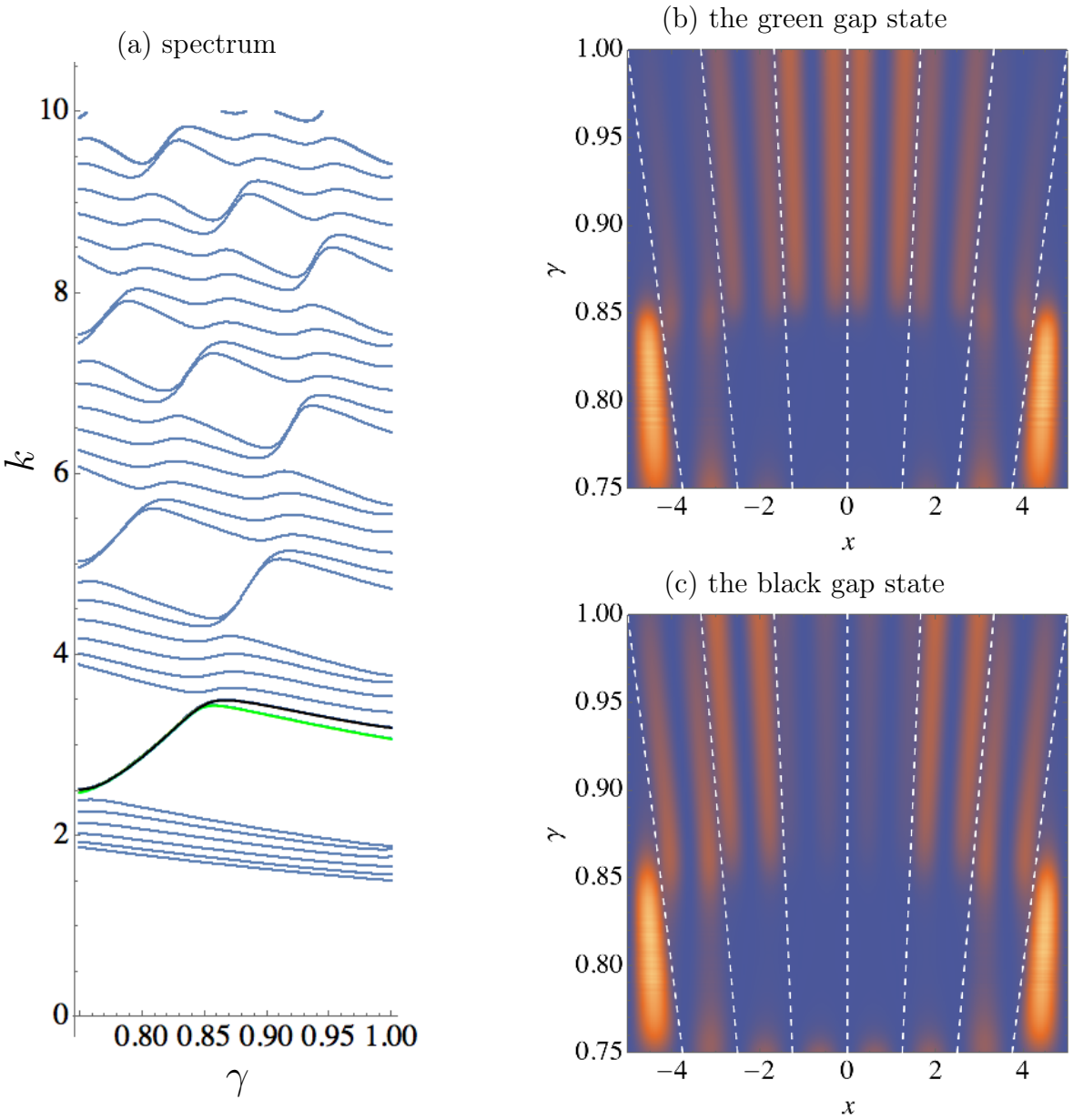

Figure 4.7: Symmetric edge states appear in the AFKP model with $M = 7$ barriers of equal heights and the lattice constant as the superspace. (a) The momentum spectrum as a function of γ. The edge states crossing the gap appear to split into two states when approaching the bands, with densities shown in (b) and (c).

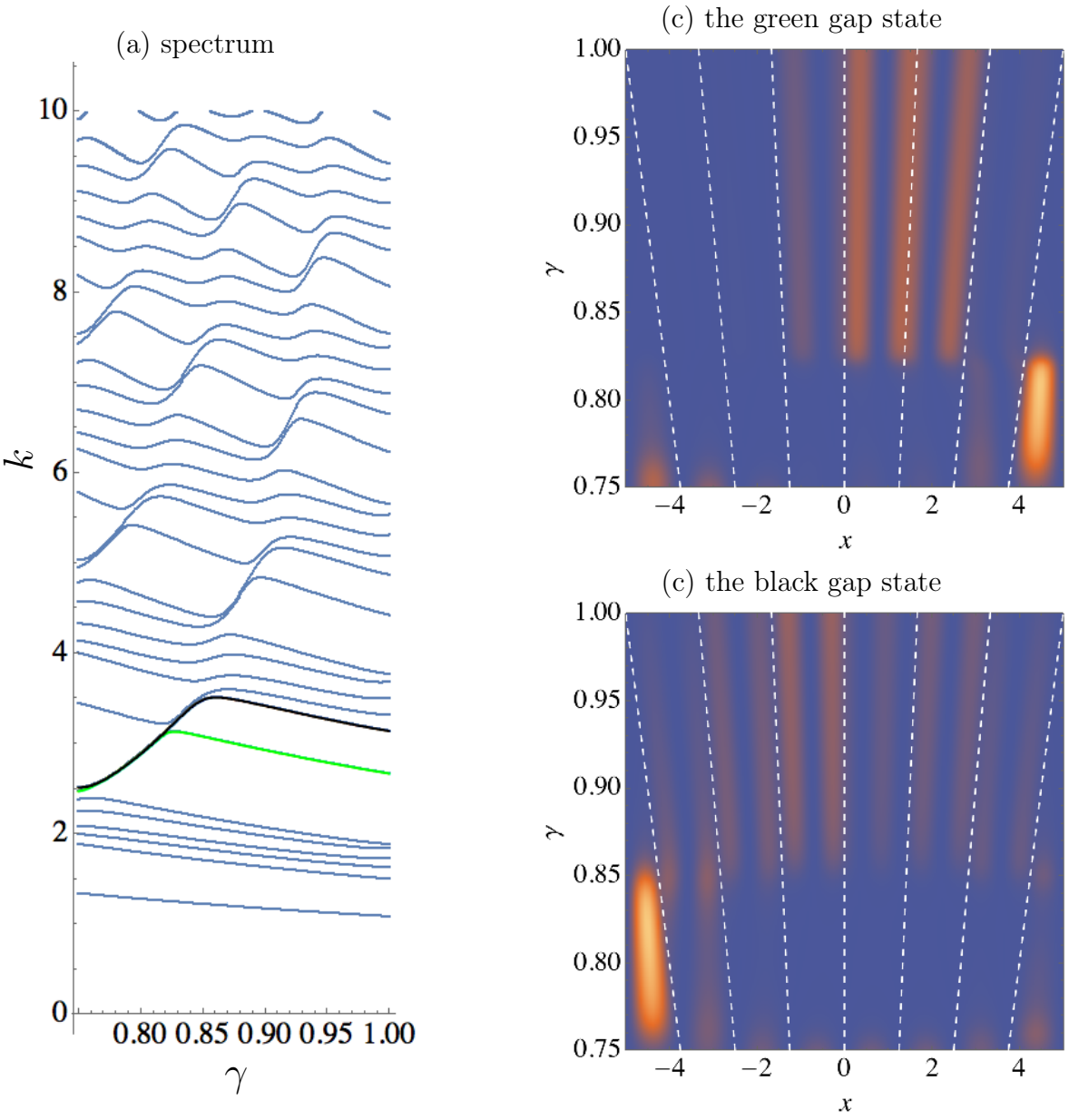

Figure 4.8: Two asymmetric edge states appear in the AFKP model with the lattice constant as the superspace and $M = 7$ barriers of random heights $0 \leq h_i \leq 3$. (a) The momentum spectrum as a function of γ. The edge states crossing the gap split into two asymmetric states whose densities are shown in (b) and (c).

4.3.3 Hofstadter butterfly and cocoon

The Hofstadter butterfly energy spectrum appears in an infinite two-dimensional lattice in the presense of magnetic fields [165]. Its definiting feature is its fractal-like structure of the bands and the gaps which resembles a symmetric butterfly. In a finite system edge modes appear in the band gap, but the overall shape of the spectrum is preserved even for small system sizes [171]. Even though the presence of edge states in the band gaps of finite Hofstadter systems can be explained as the effect of the boundary conditions, the Hofstadter spectrum can also be explained as a limit of the finite system as its size goes to infinity using molecular orbital method [172]. The effects of disorder on the Hofstadter butterfly spectrum in finite systems was investigated in [173], and the differences between system with even and odd number of sites were studied in [174]. The effect of the number of nearest neighbours on the energy spectrum was investigated in [175] on the example of square versus triangular lattice.

Below I will discuss how the Hofstadter butterfly-like quasimomentum spectrum emerges in the AFKP model.

For this I consider equidistant barriers at positions $y_n = -L/2 + anL$, with $a = 1/(M+1)$, with the heights periodically modulated by the function

$$h_n = h_{\min} + (h_{\max} - h_{\min}) \cos^2 \left(2\pi\phi \left(an + \frac{1}{2} \right) \right). \tag{4.6}$$

The external potential is periodic in ϕ (with period $\phi_0 \equiv (M+1)/2$), similar to the flux from the original Hofstadter study. However, unlike the original Hofstadter study, which considered the tight-binding approximation, the AFKP model is continuous.

The first case I will consider is the case of all barriers having positive heights between $h_{\min} = 0.1$ and $h_{\min} = 1.5$. The quasimomentum spectrum for $\phi \in [0, \phi_0]$ is shown in Fig. 4.9(a) for $M = 17$ scatterers. One can see that the spectrum is symmetric around $k = 0$ and splits into bands, whose widths depend on the minimum barrier height $h_{\min}$. The bands have a shape that looks like a Hofstadter butterfly, losing its definition in higher bands due to the finite barrier heights. The butterfly-like shape gradually emerges as the number of barriers increases, which can be seen in Fig. 4.10. The highest state in each band is a flat delocalized state with $k^l_{\text{flat}} = \pi(M+1)l/L$, where $l = \pm 1, \pm 2, ...$ is the band index. The nodes of these states exactly coincide with the barriers, and therefore the states themselves are not affected by them.

Another case worthy of investigation also includes negative values for the barrier strengths. I only use weak negative heights to avoid formation of the bound states.

The quasimomentum spectrum for $M = 17$ barriers with minimum and maximum strengths $h_{\min} = -0.5$ and $h_{\max} = 0.5$ is shown in Fig. 4.9(b). The spectra in Fig. 4.9(a) and (b) are very similar, especially for k values close to the edge of the bands. This fact emphasises that the behaviour of the system depends mostly on the positions of the barriers rather than variations in their heights. This weakly-scattering, finite-sized system does not yet look like a fully developed butterfly, however, a prominent *cocoon*-shaped feature appears around $k = 0$ if the barriers are allowed to have both negative and positive heights.

In this chapter I applied the analytical solution obtained in 3.5 to the AFKP with equidistant barriers of equal, alternating, random and periodically modulated heights.

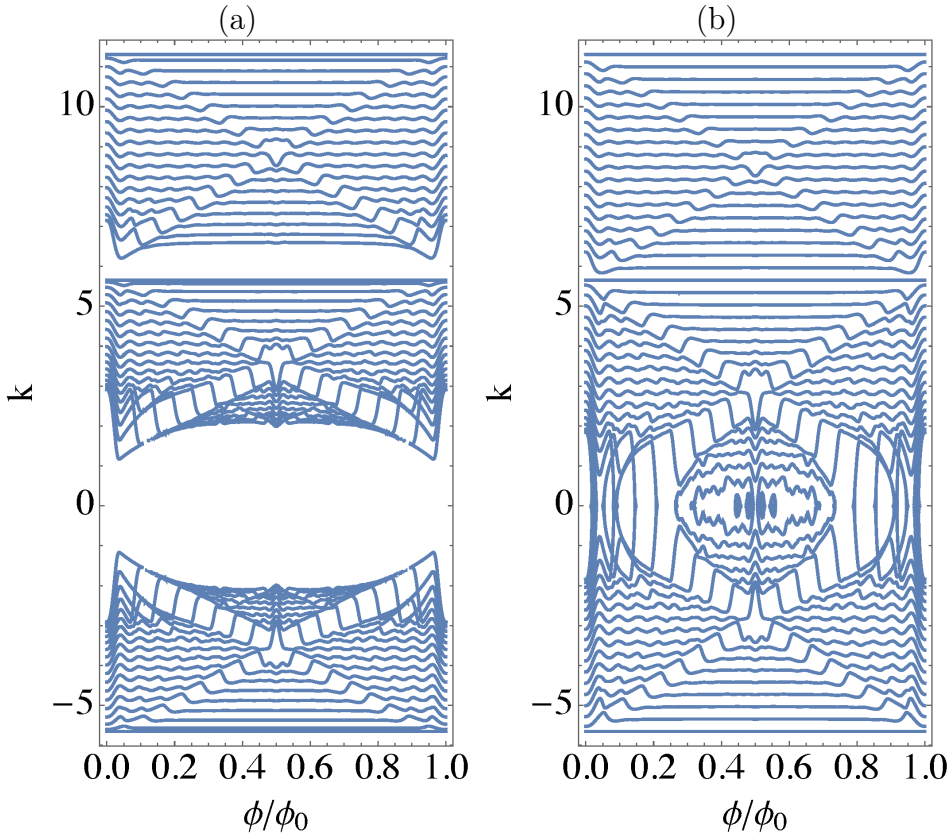

Figure 4.9: (a) Hofstadter butterfly-like momentum spectrum in a system where all barrier heights are positive. The modulation period is given by $\phi_0 = (M+1)/2$, and the seventeen scatterer heights in this example vary between $h_{\min} = 0.1$ and $h_{\max} = 1.5$. (b) Same as above, but for a system with scatterer heights varying between $h_{\min} = -0.5$ and $h_{\max} = 0.5$. The large circular feature in the center (a *cocoon*) is not present in the positive scatterers-only system, while the iconic *wings* are just developing.

I have shown that in the presence of a virtual dimension (lattice shift relative to the box walls or the period of the heights' modulation) the bulk system has non-trivial topology which manifests itself as topologically protected edge states in this finite system. I have proven non-triviality of the edge states by numerically calculating the correponding Chern numbers. I have also demonstrated that these edge states leave their mark in the many-body probability density in case of ideal Fermi or Tonks–Girardeau gas. In the case of periodically modulated barrier heights I have recovered the Hofstadter butterfly-like features of the momenta spectrum, even though unlike original study, the AFKP model is continuous and finite.

Part of these results were accepted to publication in the New Journal of Physics [176].

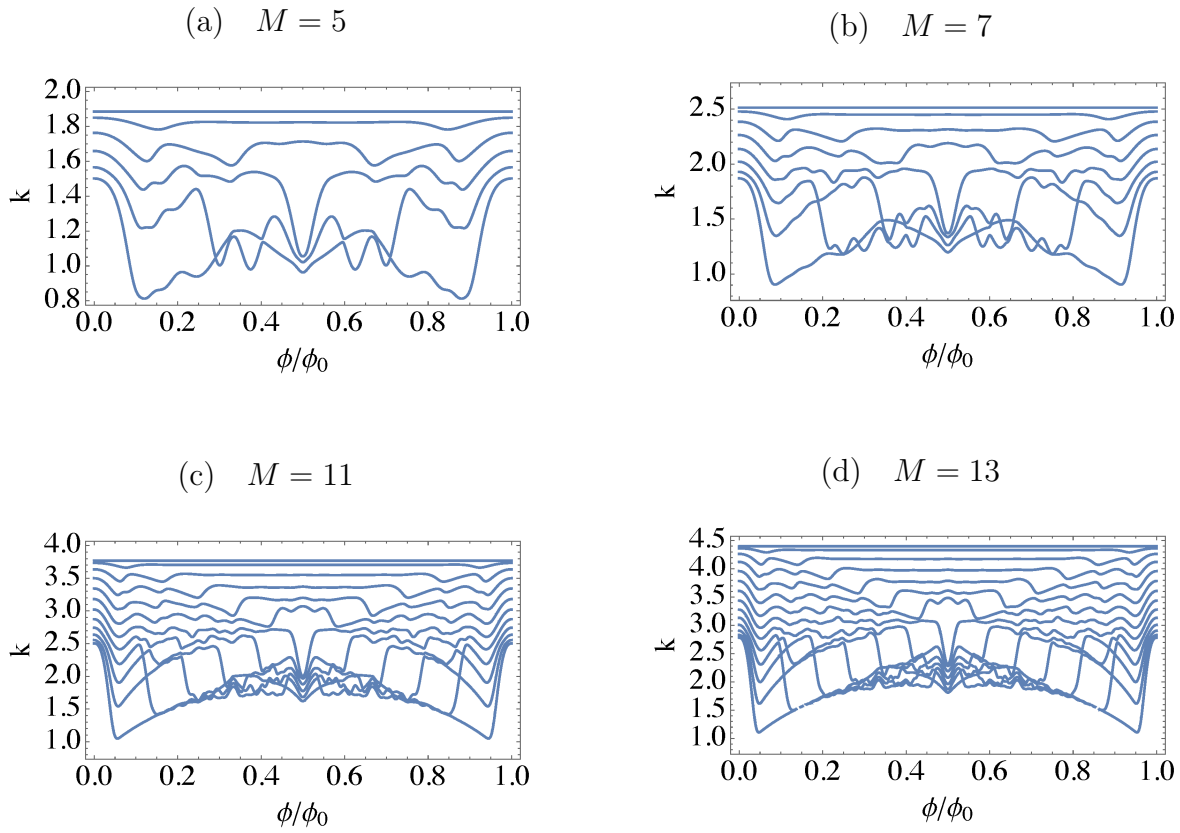

Figure 4.10: Quasimomentum spectra for systems with an increasing number of scatterers, whose heights are modulated according to eq. (4.6). In all cases, $h_{\min} = 0.1$ and $h_{\max} = 2.1$.

Chapter 5

Methods

In this chapter I will describe the numerical and analytical techniques used in my work in more detail.

5.1 Finite differences method

The time-dependent one-dimensional many-body Schrödinger equation can be written

$$i\hbar\frac{\partial\Psi(x_1,...,x_N,t)}{\partial t} = \hat{H}\left(\frac{\partial^2}{\partial x_1^2},\ldots,\frac{\partial^2}{\partial x_N^2},x_1,\ldots,x_N,t\right)\Psi(x_1,...,x_N,t), \tag{5.1}$$

where N is the number of particles. The spatial $x_1,...,x_N$ and temporal t variables in this equation are continuous and, in order to represent them in finite computer memory, one needs to use a discretisation technique. To discretise the time variable t, I specify the time step Δt, and a set of time points $\{t_k = t_0 + k\Delta t\}, k \in \mathbb{N}$. To discretise the spatial variable x, I specify the number of points, M. If L is the length of the interval of interest, then the resolution is $\Delta x = \frac{L}{M}$, and $\{x^{(n)} = x^{(0)} + n\Delta x\}, n = 1,...,M$ is the mesh which represents the variable x.

Let us consider the time-independent Schrödinger equation

$$\hat{H}\left(\frac{\partial^2}{\partial x_1^2},\ldots,\frac{\partial^2}{\partial x_N^2},x_1,\ldots,x_N\right)\Psi(x_1,...,x_N) = E\Psi(x_1,...,x_N). \tag{5.2}$$

In order to diagonalise the Hamiltonian $\hat{H}$ numerically, we need to approximate the partial derivatives using discretised variables $x_1,...,x_N$. The approximation which I use in my work is the finite differences method.

As the space is now discretised, the wave function $\Psi(x_1,...,x_N)$ can only be evaluated on the $N \times M$ points of the mesh $x_i^{(n)}, i = 1,...,N, n = 1,...,M$. Let us denote these values $\Psi(x_1^{(n_1)},...,x_N^{(n_N)}) = \Psi_{\vec{n}}, n_i = 1,...,M$. From now on for simplicity let us assume N to be 1. Then $\Psi(x^{(n)}) = \Psi_n$.

We can approximate the second partial derivative as

$$\left(\frac{\partial^2\Psi(x)}{\partial x^2}\right)_n \approx \frac{\Psi_{n+1} - 2\Psi_n + \Psi_{n-1}}{\Delta x^2}. \tag{5.3}$$

Direct diagonalisation of the approximated Hamiltonian is then used to obtain the eigenstates and the energy spectrum.

5.1.1 Split-step method

The time evolution of a system in the initial state $|\Psi(x,0)\rangle$ with the Hamiltonian $\hat{H}$, which does not contain an explicit dependency on time, can be expressed as

$$|\Psi(x,t)\rangle = e^{-\frac{i\hat{H}t}{\hbar}}|\Psi(x,0)\rangle. \tag{5.4}$$

In the case of a time-dependent Hamiltonian for which $\hat{H}(t_1) = \hat{H}(t_2), \forall t_1, t_2 \geq t_0$, the time evolution of the initial state takes form of

$$|\Psi(x,t)\rangle = e^{-\frac{i}{\hbar}\int_{t_0}^{t}\hat{H}(\tilde{t})d\tilde{t}}|\Psi(x,0)\rangle. \tag{5.5}$$

In case where $\hat{H}(t_1) \neq \hat{H}(t_2)$, the time evolution looks more complicated [177]

$$|\Psi(x,t)\rangle = \hat{U}(t_0,t)|\Psi(x,0)\rangle, \tag{5.6}$$

where

$$\hat{U}(t_0,t) = 1 + \sum_{n=1}^{\infty}\left(\frac{-i}{\hbar}\right)^n \int_{t_0}^{t} dt_1 \int_{t_0}^{t_1} dt_2 ... \int_{t_0}^{t_{n-1}} dt_n \hat{H}(t_1)\hat{H}(t_2)...\hat{H}(t_n). \tag{5.7}$$

The SAP protocol, which I describe in chapter 2, has a time-dependent external potential, so the expression (5.7) has to applied for the time-evolution operator. However, for a small time step Δt this expression can be approximated by the exponent in the equation (5.4), and we can obtain an iterative relation

$$|\Psi(x,t_n)\rangle = e^{-\frac{i\hat{H}(t_n)\Delta t}{\hbar}}|\Psi(x,t_{n-1})\rangle. \tag{5.8}$$

The time-dependent Hamiltonian of the two-particle SAP protocol is

$$\hat{H}(t_n) = \sum_{i=1}^{2}\left(-\frac{\hbar^2}{2m}\frac{\partial^2}{\partial x_i^2} + V_e(x_i,t_n)\right) + g\delta(x_1 - x_2) = \hat{K} + \hat{V}(t_n), \tag{5.9}$$

where $\hat{V}_e(x,t_n)$ is the triple harmonic external potential at time t_n, $g\delta(x_1 - x_2)$ is the interaction term, $\hat{V}(t_n) = \hat{V}(x_1,x_2,t_n) = \hat{V}_e(x_1,t_n) + \hat{V}_e(x_2,t_n) + g\delta(x_1 - x_2)$ and $\hat{K}$ is the kinetic energy. For a small time step Δt the time evolution of the system, which is approximated by the two-particle version of eq. (5.8), can be further approximated by the Strang splitting [178] as

$$|\Psi(x_1,x_2,t_n)\rangle \approx e^{-\frac{i\hat{V}(t_n)\Delta t}{2\hbar}} e^{-\frac{i\hat{K}\Delta t}{\hbar}} e^{-\frac{i\hat{V}(t_n)\Delta t}{2\hbar}}|\Psi(x_1,x_2,t_{n-1})\rangle. \tag{5.10}$$

The kinetic energy operator $\hat{K}$ has a very simple form in momentum space, so in order to make the computations more efficient I apply a sequence of Fourier transforms and inverse Fourier transforms

$$|\Psi(x_1,x_2,t_n)\rangle \approx e^{-\frac{i\hat{V}(t_n)\Delta t}{2\hbar}} \mathcal{F}^{-1}\left(e^{-\frac{i\hat{K}\Delta t}{\hbar}}\mathcal{F}\left(e^{-\frac{i\hat{V}(t_n)\Delta t}{2\hbar}}|\Psi(x_1,x_2,t_{n-1})\rangle\right)\right). \tag{5.11}$$

5.2 Derivation of the tunneling strengths

The tunneling term in the BH Hamiltonian (2.10) is defined as

$$H_{\text{tunnel}} = \sum_{i=1}^{2} \sum_{N_i^{\text{trap}}=1}^{N} \sum_{N_{i+1}^{\text{trap}}=0}^{N-N_i^{\text{trap}}} \sum_{p=1}^{N_i^{\text{trap}}} \sum_{\substack{\vec{M}\in\mathcal{P}(N_i^{\text{trap}}-p)\\ \vec{p}\in\mathcal{P}(p)}} \sum_{\substack{\vec{K}\in\mathcal{P}(N_{i+1}^{\text{trap}})\\ \vec{q}\in\mathcal{P}(p)}} \left(\Omega_i^{\vec{p}\vec{q}}(\vec{M},\vec{K}) \prod_{j=0}^{m_{\text{L}}-1} \hat{a}_{i+1}^{\dagger q_j}{}_j \hat{a}_i^{p_j}{}_j + h.c. \right), \tag{5.12}$$

and it includes all tunnelling events of p particles between the traps i and $i+1$. The set $\mathcal{P}(n)$ contains all possible ways to distribute n particles into m_{L} energy levels of one trap, and

$$\sum_{j=0}^{m_{\text{L}}-1} p_j = \sum_{j=0}^{m_{\text{L}}-1} q_j = p. \tag{5.13}$$

The corresponding coupling coefficients $\Omega_i^{\vec{p}\vec{q}}(\vec{M},\vec{K})$ denote the tunnelling frequencies of p atoms between the level occupation configurations $\vec{p} = (p_0,\ldots,p_{m_{\text{L}}-1})$ and $\vec{q} = (q_0,\ldots,q_{m_{\text{L}}-1})$ of traps i and $i+1$ respectively.

In what follows I derive the tunneling coupling amplitudes between two general Fock states

$$|\psi_{\text{i}}\rangle_i^{\vec{p}\vec{q}} = \left| \begin{matrix} M_{0i}+p_0 & K_{0(i+1)} \\ M_{1i}+p_1 & K_{1(i+1)} \\ \cdots & \cdots \\ M_{(m_{\text{L}}-1)i}+p_{m_{\text{L}}-1} & K_{(m_{\text{L}}-1)(i+1)} \end{matrix} \right\rangle, \tag{5.14}$$

and

$$|\psi_{\text{t}}\rangle_i^{\vec{p}\vec{q}} = \left| \begin{matrix} M_{0i} & K_{0(i+1)}+q_0 \\ M_{1i} & K_{1(i+1)}+q_1 \\ \cdots & \cdots \\ M_{(m_{\text{L}}-1)i} & K_{(m_{\text{L}}-1)(i+1)}+q_{m_{\text{L}}-1} \end{matrix} \right\rangle, \tag{5.15}$$

which contain occupation numbers for traps i and $i+1$. The coupling coefficient between these two states is defined from the general Hamiltonian (2.4) as

$$\Omega_i^{\vec{p}\vec{q}}(\vec{M},\vec{K}) = \langle\psi_{\text{t}}|\, \hat{H}\, |\psi_{\text{i}}\rangle_i^{\vec{p}\vec{q}}. \tag{5.16}$$

If $\Omega_i^{\vec{p}\vec{q}}(\vec{M},\vec{K}) \neq 0$, then the corresponding relevant term that will appear in the BH Hamiltonian is proportional to $\prod_{j=0}^{m_{\text{L}}-1} \hat{a}_{i+1}^{\dagger q_j}{}_j \hat{a}_i^{p_j}{}_j$, thus

$$\begin{aligned} \Omega_i^{\vec{p}\vec{q}}(\vec{M},\vec{K}) &= \tilde{\Omega}_i^{\vec{p}\vec{q}} \langle\psi_{\text{t}}| \prod_{j=0}^{m_{\text{L}}-1} \hat{a}_{i+1}^{\dagger q_j}{}_j \hat{a}_i^{p_j}{}_j |\psi_{\text{i}}\rangle_i^{\vec{p}\vec{q}} \\ &= \prod_{j=0}^{m_{\text{L}}-1} \sqrt{\frac{(M_j+p_j)!}{M_j!}\frac{(K_j+q_j)!}{K_j!}}\tilde{\Omega}_i^{\vec{p}\vec{q}}. \end{aligned} \tag{5.17}$$

If $\vec{M} = \vec{0}$ and $\vec{K} = \vec{0}$, then

$$\Omega_i^{\vec{p}\vec{q}}(\vec{0},\vec{0}) = \prod_{j=0}^{m_{\text{L}}-1} \sqrt{p_j! q_j!}\tilde{\Omega}_i^{\vec{p}\vec{q}}, \tag{5.18}$$

where $\tilde{\Omega}_i^{\vec{p}\vec{q}}$ is the tunnelling frequency of all p atoms between level occupation configurations $\vec{p}$ of the trap i and $\vec{q}$ of the empty trap $i+1$.

Since only the order of magnitude is important to show the shape of the regions of high-fidelity particle separation, we assume $\Omega_i^{\vec{p}\vec{q}}(\vec{0},\vec{0}) \approx \tilde{\Omega}_i^p$. Here $\tilde{\Omega}_i^p$ is the tunnelling frequency of p atoms between the ground states of traps i and $i+1$ in the absence of other atoms. In the three particle calculations we assumed $\tilde{\Omega}_i^3 \propto \tilde{\Omega}_i^2$, while $\tilde{\Omega}_i^2$ and $\tilde{\Omega}_i^1$ were calculated numerically. Eq. (5.16) can thus be written as

$$\Omega_i^{\vec{p}\vec{q}}(\vec{M},\vec{K}) \approx \prod_{j=0}^{m_\mathrm{L}-1} \sqrt{\frac{(M_j+p_j)!}{M_j!}\frac{(K_j+q_j)!}{K_j!}\frac{1}{p_j!q_j!}}\tilde{\Omega}_i^p. \tag{5.19}$$

5.3 Calculation of the Chern numbers

In this section I will describe in more detail the method which was used to calculate the Chern numbers in Section 4.3.1.

The Chern number of a band is a topological constant which characterizes the class of the topological insulator and is defined as the integral over the Brillouin zone of the difference between the derivatives of two Berry connections in different directions of the Brillouin zone. In the periodic arbitrary Kronig–Penney model, the first dimension is the momentum k, while the second dimension is the superspace Δ which is the shift of the whole lattice.

Due to explicit L-periodicity of the potential in x, we can apply the Bloch theorem, and get

$$\psi(x,\Delta) = \mathrm{e}^{-\mathrm{i}kx/L}\phi(x,\Delta). \tag{5.20}$$

The Bloch theorem can be similarly applied in the trivially periodic pseudo-dimension Δ. The Chern number can then be written as

$$c = \frac{1}{2\pi}\int_k \mathrm{d}k \int_\Delta \mathrm{d}\Delta \left(\partial_k A_\Delta - \partial_\Delta A_k\right), \tag{5.21}$$

where k is the quasi-momentum in x direction and Δ is the lattice shift. $A_{k_1} = \mathrm{i}\langle\phi(k_1,k_2)|\partial_{k_1}\phi(k_1,k_2)\rangle$ and $A_{k_2} = \mathrm{i}\langle\phi(k_1,k_2)|\partial_{k_2}\phi(k_1,k_2)\rangle$ are the Berry connections with $\phi(k_1,k_2)$ being the occupied Bloch state in Eq. (5.20) [166, 167].

In order to calculate the Chern number defined in Eq. (5.21) on a discretized Brillouin zone, I use the method derived in [170]. Following [170], the Chern number of a discretized Brillouin zone can be calculated as the sum of the lattice field strengths of each local plaquette

$$c_n = \frac{1}{2\pi\mathrm{i}}\sum_{l,j}\mathcal{F}_{n,lj}. \tag{5.22}$$

The local lattice field strength for each plaquette is defined as

$$\mathcal{F}_{n,lj} = \ln\left(U_{lj}^{l(j+1)}(n)U_{l(j+1)}^{(l+1)(j+1)}(n)U_{(l+1)(j+1)}^{(l+1)j}(n)U_{(l+1)j}^{lj}(n)\right), \tag{5.23}$$

where

$$U_{lj}^{sm}(n) = \frac{\langle\phi_n(k_l,\Delta_j)|\phi_n(k_s,\Delta_m)\rangle}{|\langle\phi_n(k_l,\Delta_j)|\phi_n(k_s,\Delta_m)\rangle|} \tag{5.24}$$

and $\phi_n(k_l, \Delta_j)$ is the n-th Bloch state wavefunction corresponding to the momentum k_l and shift Δ_j taken from the discretized Brillouin zone. Below I will describe each step of the algorithm.

Step 1: Prepare the discretized Brillouin zone

By substituting Eq. (5.20) into the discretized Hamiltonian described in Section 5.1, the Bloch exponent can be absorbed into the Hamiltonian. Then, after discretizing the momenta $k \in [0, 2\pi]$ and $\Delta \in [-1, 1]$, it is possible to diagonalize this Hamiltonian for each (k_i, Δ_j)

$$\hat{H}(k_i, \Delta_j)\phi_n(x, \Delta_j|k_i) = E\phi_n(x, \Delta_j|k_i). \tag{5.25}$$

The eigenfunctions $\phi(x, \Delta_j|k_i)$ form the discretized Brillouin zone which is going to be used for the Chern number calculations.

Step 2: Calculate local lattice field strengths

Let us assume that we are interested in the n-th conduction band. We then will use the appropriate discretized Brillouin zone calculated in the previous step.

The local lattice field strength for the plaquette (l, j) is defined in Eq. (5.23). The local link defined in Eq. (5.24) is a normalized overlap of the two wavefunctions. For each (l, j) we calculate four such overlaps using the wavefunctions calculated in the previous step and going around the plaquette counter-clockwise. One important note is that on the limits of the array it is necessary to periodically stitch the discretized Brillouin zone such that it forms a torus. Another important note is that $\phi(k_0 + 2\pi, \Delta_j) = \phi(k_0, \Delta_j)$, and depending on the discretization of k we may end up including $\phi(k_0, \Delta_j)$ twice. It is therefore necessary to make sure that $\phi(k_0, \Delta_j)$ is only included once, otherwise the obtained Chern numbers will not be correct.

Step 3: Calculate the Chern number

The Chern numbers can now be calculated straightforwardly as a sum of all local lattice field strengths according to Eq. (5.22).

Chapter 6

Conclusion

In this thesis I have presented the results of my work on the topic of quantum state engineering. The main focus of my work lies in one-dimensional and single- and few particle systems confined in an external potential with multiple traps. Using external parameters of such systems, I have investigated the existence of highly entangled or topologically nontrivial single- and many-body states, characterized their properties and developed protocols of their control and generation.

In the first part of the thesis I have proposed a protocol (the deterministic boson dispenser) based on the spatial adiabatic passage (SAP) [89], which allows to separate an arbitrary number of particles from an ultra-cold gas of interacting bosons. The technique is based on engineering a quasi-three level system by raising or lowering the energies of some of the traps and allowing for an adiabatic transition between the initial state $|N\ 0\ 0\rangle$ and the target state $|(N-M)\ 0\ M\rangle$ through an intermediate state $|(N-M)\ M\ 0\rangle$. These three states form a SAP triplet, and by raising or lowering the middle and the right traps one can ensure that these states are degenerate in the absence of tunneling. I have explicitly examined the case $|2\ 0\ 0\rangle \rightarrow |1\ 0\ 1\rangle$ for a two-particle system and the case $|3\ 0\ 0\rangle \rightarrow |2\ 0\ 1\rangle$ for a three-particle system and shown that the SAP protocol results in high-fidelities over large ranges of interaction energies. In the range of interaction energies from $-1/2$ to 1, I have found the regions where the dark-like state connects the initial and the target states without aditional level crossings. In these regions the SAP triplet remains isolated from the rest of the spectrum, and the dark state can be robustly followed, resulting in high fidelity splitting of the cloud. I have further shown that the regions where the protocol fails can be found from the level crossings present in the spectrum of the Bose–Hubbard model.

An interesting question is if it is possible to reverse the particle separation protocol to perform coherent particle addition. Is it possible to start from an arbitrary non-coherent Fock state and, after performing some version of reversed particle separation protocol, end up in a state where all particles are collected in one well? This possiblity is enticing because it would give a robust tool for controlled cold atom collisions.

The particle separation protocol described above along with its NOON state generating version allow one to prepare two spatially separated entangled systems which can be used in quantum computing applications [119]. One possible direction of future reasearch would therefore be to develop robust quantum gates using the robustness of

the SAP protocol.

Throughout my work on I was either assuming a point-like interactions or generic short-range interactions in the Bose–Hubbard treatment. One interesting project would be to generalize the SAP techniques to more realistic types of interactions, such as dipole-dipole, Rydberg or Coulomb interactions. The generality of the SAP theory suggests that it should be possible.

To show that this protocol is realistic and robust against experimental uncertainties I have examined a setting where two ^{87}Rb atoms were trapped in a radio-frequency potential with realistic parameters.

One can also easily generalize this protocol to separate an impurity from the background gas (*a quantum sieve*) provided that the interspecies interaction is significantly different from the intraspecies interaction. This difference in resonance energies can then be used to only allow the impurity to tunnel out into different trap while leaving the rest of the gas in the initial trap.

From experimental point of view, another important improvement is to extend the proposed many-particle protocol to higher dimensions and study if it is possible to isolate a SAP triplet in such highly degenerate setting.

I have also investigated the entropy dynamics of the SAP protocols and shown that the total entropy in the SAP processes can be attributed to contribution from two sources: one due the interaction between the atoms and one due to the distribution of the atoms between the traps. States with both atoms in the same trap, e.g., $|2\ 0\ 0\rangle$, have a von Neumann entropy which increases with the interaction $S_{\text{int}}(E_g)$, with E_g ranging from zero in the non-interacting case (where the wavefunction is separable), to $\ln 2$ in the Tonks–Girardeau limit.

On the other hand, states such as $|101\rangle$ are unaffected by the interaction, but have a constant von Neumann entropy of $S_{\text{dist}} = \ln 2$, which comes from the distribution of the particles between the traps. The NOON states have both contributions, as the atoms occupy states where they interact, while they are in a superposition of occupying different sites, $S_{\text{NOON}} = S_{\text{int}}(E_g) + S_{\text{dist}}$. For a separation process with an initial cloud of N particles in the left trap ($|N\ 0\ 0\rangle$), a maximum value of the entropy $\ln 2$ is achieved when the cloud is evenly split, $|N/2\ 0\ N/2\rangle$, for N even, or split into $|\frac{N+1}{2}\ 0\ \frac{N-1}{2}\rangle$ for N odd. A NOON state $(|N\ 0\ 0\rangle - |0\ 0\ N\rangle)/\sqrt{2}$, will also have an entropy of $\ln 2$. The particle separation protocol can be straightforwardly modified to produce a distribution of the atoms over more than three traps, for example, by sequential separation of one $N-1$ particle into another trap, such as $|1\ 1\ 1\ 1\ \ldots\rangle$. Analogously, by sequential and symmetric execution of the NOON protocol, states such as $(|N\ 0\ 0\ 0\ \ldots\rangle + |0\ N\ 0\ 0\ \ldots\rangle + |0\ 0\ N\ 0\ \ldots\rangle + \ldots)/\sqrt{N}$ can be produced. The entropy in both cases is $\ln N$ (plus the interaction entropy in the NOON case).

This work resulted in two peer-reviewed publications, "Robust boson dispenser: Quantum state preparation in interacting many-particle systems", Phys. Rev. A **96** 023606 (2017) [103] and "Entanglement in Spatial Adiabatic Processes for Interacting Atoms", Few-Body Syst. **59** 48 (2018) [95]

In the second part of this thesis, I have investigated three related models with particles trapped in an infinite square well with point-like barriers inside. I have proven that in the case of multiple interacting particles and two or more barriers such a

model cannot be solved due to the violation of the Yang–Baxter relations, which are the necessary condition of integrability in the Bethe ansatz sense. This failure of integrability can be explained intuitively if we consider the regions between the barriers as traps which have different chemical potentials, depending on the particles which are already inside. In the case of simultaneous scattering of two particles with the barrier the order of the scattering process matters, because the second incoming particle will see different chemical potential, leading to different outcome.

In an attempt to rectify this I have considered a model with two distinguishable particles which *see* the barriers at slightly different positions. This scenario is realistic because the two particles can have a different internal state structure and thus different resonance frequencies which can affect the effective external potential. Unfortunately, the Yang–Baxter equations are not generally satisfied in this system either if the interaction between the particle is finite, even though there are no *true* three-body interactions. Mathematically, the simultaneous scattering of the two particles with each other and one of them with a barrier can be thought of as if one of them scatters with the barrier of finite height, and the other with the barrier of zero height. The integrability fails due to the same reason as in the two indistinguishable particles case.

Since the interacting two-barrier case was proven to be not solvable, I have investigated a model with a single particle trapped in an infinite square well with an arbitrary number of point-like barriers of arbitrary heights positioned arbitrarily within the well (arbitrary finite Kronig–Penney model or AFKP). I have derived an analytical solution of this model using the Bethe ansatz technique, and presented a compact general form for the Bethe equation and the wavefunction with the heights and positions of the barriers as external parameters. This solution is extremely powerful and can be used in analytical studies of various one-dimensional systems. However, the combinatorial nature of the expressions of the solution makes it not practicle for large number of barriers. This is especially true for the reconstruction of the wave functions.

I have then applied this solution to the finite Kronig–Penney model with uniform, random and periodically modulated heights. I used the external parameters of the system, such as the shift of the lattice relative to the walls of the box or the distance between the barriers, as an extra virtual dimension in order to investigate the appearance of topologically protected edge states. Chiral edge states then indeed appear even in these relatively simple integrable systems. If the distance between the barriers is used as an extra dimension, fully symmetric edge states appear in the system. I have characterized the edge states which appear in the shifted Kronig–Penney model by their Chern numbers and shown that they are indeed topologically non-trivial, and their number corresponds to the difference between the Chern numbers of the two bands they connect.

Using a more general solution framework described in [153], it would be interesting to investigate the topological properties of models which are similar to AFKP but have different external potentials, such as the harmonic potential.

Having explicit expressions for the eigenstates also allows for an exact study of dynamics in the AFKP model. One can introduce a time-dependent Hamiltonian with, for example, a slow change of the heights of the barriers or their positions, a sudden quench or other perturbation, and study the evolution of the state through wave function overlaps. The dynamical evolution of the topologically protected edge

states is especially interesting. In a non-interacting many-body case investigating the effect of the edge states on the orthogonality catastrophe and Anderson localization could be very illuminating. Using this easy access to the dynamics of the system, one could consider developing a quantum state engineering application of the AFKP, for example, for particle transport, or using the edge states as topological protected qubits. In this case development of the quantum gates for these edge-state qubits will be very important, as well as error correcting techniques. All such gates will somehow involve changing the barriers in the AFKP, which will eventually require development of gate speed improving shortcuts.

A possible direction of future research is to apply the solution I have obtained to study effects in non-interacting or infinitely repulsive quantum gases. I have already touched upon it by showing how edge states manifest themselves in a Tonks–Girardeau gas, and an interesting extension to it is to study entropy, momentum distribution and non-classical correlations in this setting. Studying equilibriation in the AFKP is also an interesting direction, especially considering that the integrability in this system can be broken gradually, for example, by increasing interactions.

Another potential direction is to study the survival of the 1D physics in the cases when the virtual dimension is replaced with a real dynamic dimension. It is especially interecting to investigate how does the addition of the kinetic energy term in the extra dimension affects the topological properties.

From experimental point of view, the AFKP model is directly applicable to optics, being essentially a model for a 1D cavity with a striated medium inside. If implemented, this will give access to cavity QED with modes other than usual sinusoidal modes. Especially valuable is the existence of the edge states in a system with shifted barriers. These highly localized topologically protected states can be used to construct setups where strong coupling between the light and trapped atoms can potentially be achieved.

Finally, I have also investigated a model with periodically modulated delta barriers. Here the modulation period is an extra dimension that plays a role similar to the flux in the study by Hofstadter [165], which leads to the famous fractal-like shape of the energy spectrum. Unlike the original Hofstadter study, which considered the tight-binding approximation, the AFKP model is continuous. However, due to the finiteness of the model the fractal nature is lost, but I have shown that the overall butterfly-like features of the energy spectrum gradually emerge with increasing number of barriers. I have also considered another conserved quantity of the system, the quasi-momentum, which spectrum has similar shape as the energy spectrum. In the case of weak scattering the butterfly shape does not yet fully develop in the quasi-momentum spectrum, instead having a *cocoon*-shaped feature around $k = 0$ if the barriers can have both negative and positive heights.

This work has been accepted for publication in New Journal of Physics as "Topological states in the Kronig-Penney model with arbitrary scattering potentials" [176].

To summarize the main results of my work, I have first shown that the well known SAP protocol has application beyond the standard transport scenario, and can be used to connect different Fock states through a dark state. High fidelities of the state transfer demostrated that spatial adiabatic passage techniques for interacting particle systems are experimentally realistic and can be used as a deterministic single- and few-particle source. The protocol I proposed is independent of the number of initial particles and

can therefore be used in systems with large initial particle numbers. Secondly, I have found an analytical solution to an important generalisation of the Kronig–Penney model where the barriers can have arbitrary positions and heights (AFKP). I then applied it to the problem of finding topologically protected edge states in 1D quantum systems, and recovered the Hofstadter butterfly-like shape of the energy spectrum for a setting with periodically modulated heights of the barriers. I have also shown that these state mamifest themselves in the Tonks–Girardeau gas.

Bibliography

[1] A. Benseny, J. Gillet, and T. Busch, Phys. Rev. A **93**, 033629 (2016).

[2] H. Stoof, K. Gubbels, and D. Dickerscheid, *Ultracold Quantum Fields*, Springer Netherlands (2009).

[3] W. Ketterle, Rev. Mod. Phys. **74**, 1131 (2002).

[4] T. W. Hänsch and A. L. Schawlow, Opt. Commun. **13**, 68 (1975).

[5] H. Metcalf and P. van der Straten, *Laser Cooling and Trapping*, Springer New York (1999).

[6] R. Blatt and D. Wineland, Nature **453**, 1008 (2008).

[7] E. L. Raab, M. Prentiss, A. Cable, S. Chu, and D. E. Pritchard, Phys. Rev. Lett. **59**, 2631 (1987).

[8] S. Chu, J. E. Bjorkholm, A. Ashkin, and A. Cable, Phys. Rev. Lett. **57**, 314 (1986).

[9] R. J. C. Spreeuw, C. Gerz, L. S. Goldner, W. D. Phillips, S. L. Rolston, C. I. Westbrook, M. W. Reynolds, and I. F. Silvera, Phys. Rev. Lett. **72**, 3162 (1994).

[10] M. H. Anderson, J. R. Ensher, M. R. Matthews, C. E. Wieman, and E. A. Cornell, Science **269**, 198 (1995).

[11] K. B. Davis, M. O. Mewes, M. R. Andrews, N. J. Van Druten, D. S. Durfee, D. M. Kurn, and W. Ketterle, Phys. Rev. Lett. **75**, 3969 (1995).

[12] W. Hänsel, P. Hommelhoff, T. W. Hänsch, and J. Reichel, Nature **413**, 498 (2001).

[13] K. Henderson, C. Ryu, C. MacCormick, and M. G. Boshier, New J. Phys. **11**, 043030 (2009).

[14] F. London, Nature **141**, 643 (1938).

[15] L. Tisza, Nature **141**, 913 (1938).

[16] L. Landau, Phys. Rev. **60**, 356 (1941).

[17] P. Kapitza, Nature **141**, 74 (1938).

[18] J. F. Allen and A. D. Misener, Nature **141**, 75 (1938).

[19] C. Raman, M. Köhl, R. Onofrio, D. S. Durfee, C. E. Kuklewicz, Z. Hadzibabic, and W. Ketterle, Phys. Rev. Lett. **83**, 4 (1999).

[20] L.-J. Lang, X. Cai, and S. Chen, Phys. Rev. Lett. **108**, 220401 (2012).

[21] Y. Zheng and S.-J. Yang, Phys. B: Cond. Matt. **454**, 93 (2014).

[22] M. Rigol, V. Dunjko, V. Yurovsky, and M. Olshanii, Phys. Rev. Lett. **98**, 050405 (2007).

[23] M. Rigol, V. Dunjko, and M. Olshanii, Nature **452**, 854 (2008).

[24] A. C. Cassidy, C. W. Clark, and M. Rigol, Phys. Rev. Lett. **106**, 140405 (2011).

[25] L. D. Landau and E. M. Lifshitz, *Statistical Physics*, Butterworth-Heinemann (1980).

[26] C.-L. Hung, X. Zhang, N. Gemelke, and C. Chin, Nature **470**, 236 (2011).

[27] M. Rigol, Phys. Rev. Lett. **103**, 100403 (2009).

[28] B. Sutherland, *Beautiful Models: 70 Years of Exactly Solved Quantum Many-Body Problems*, World Scientific Publishing (2004).

[29] M. Gring, M. Kuhnert, T. Langen, T. Kitagawa, B. Rauer, M. Schreitl, I. Mazets, D. Smith, E. Demler, and J. Schmiedmayer, Science **337**, 1318 (2012).

[30] C. Eigen, J. A. P. Glidden, R. Lopes, E. A. Cornell, R. P. Smith, and Z. Hadzibabic, Nature **563**, 221 (2018).

[31] E. Kaminishi, T. Mori, T. N. Ikeda, and M. Ueda, Nature Phys. **11**, 1050 (2015).

[32] S. Miyashita and S. Yamamoto, Phys. Rev. B **48**, 913 (1993).

[33] P. P. Mitra, B. I. Halperin, and I. Affleck, Phys. Rev. B **45**, 5299 (1992).

[34] M. Olshanii, Phys. Rev. Lett. **81**, 938 (1998).

[35] B. Paredes, A. Widera, V. Murg, O. Mandel, S. Fölling, I. Cirac, G. V. Shlyapnikov, T. W. Hänsch, and I. Bloch, Nature **429**, 277 (2004).

[36] T. Kinoshita, T. Wenger, and D. S. Weiss, Science **305**, 1125 (2004).

[37] Y. Wang, S. Subhankar, P. Bienias, M. Łącki, T.-C. Tsui, M. Baranov, A. Gorshkov, P. Zoller, J. Porto, and S. Rolston, Phys. Rev. Lett. **120**, 083601 (2018).

[38] H. Moritz, T. Stöferle, M. Köhl, and T. Esslinger, Phys. Rev. Lett. **91**, 250402 (2003).

[39] M. Köhl, T. Stöferle, H. Moritz, C. Schori, and T. Esslinger, Appl. Phys. B **79**, 1009 (2004).

[40] P. Krüger, S. Hofferberth, I. E. Mazets, I. Lesanovsky, and J. Schmiedmayer, Phys. Rev. Lett. **105**, 265302 (2010).

[41] B. Yang, Y.-Y. Chen, Y.-G. Zheng, H. Sun, H.-N. Dai, X. Guan, Z.-S. Yuan, and J.-W. Pan, Phys. Rev. Lett. **119**, 165701 (2017).

[42] E. Haller, M. J. Mark, R. Hart, J. G. Danzl, L. Reichsöllner, V. Melezhik, P. Schmelcher, and H.-C. Nägerl, Phys. Rev. Lett. **104**, 153203 (2010).

[43] T. Jacqmin, J. Armijo, T. Berrada, K. V. Kheruntsyan, and I. Bouchoule, Phys. Rev. Lett. **106**, 230405 (2011).

[44] T. Kinoshita, T. Wenger, and D. S. Weiss, Nature **440**, 900 (2006).

[45] S. Hofferberth, I. Lesanovsky, B. Fischer, T. Schumm, and J. Schmiedmayer, Nature **449**, 324 (2007).

[46] E. H. Lieb, Phys. Rev. **130**, 1616 (1963).

[47] M. A. Cazalilla, R. Citro, T. Giamarchi, E. Orignac, and M. Rigol, Rev. Mod. Phys. **83**, 1405 (2011).

[48] A. Griesmaier, J. Werner, S. Hensler, J. Stuhler, and T. Pfau, Phys. Rev. Lett. **94**, 160401 (2005).

[49] R. Islam, C. Senko, W. C. Campbell, S. Korenblit, J. Smith, A. Lee, E. E. Edwards, C.-C. J. Wang, J. K. Freericks, and C. Monroe, Science **340**, 583 (2013).

[50] E. Haller, R. Hart, M. J. Mark, J. G. Danzl, L. Reichsöllner, M. Gustavsson, M. Dalmonte, G. Pupillo, and H.-C. Nägerl, Nature **466**, 597 (2010).

[51] J. P. Ramírez Valdes and T. Wellens, Phys. Rev. A **93**, 063634 (2016).

[52] M. Piraud, A. Aspect, and L. Sanchez-Palencia, Phys. Rev. A **85**, 063611 (2012).

[53] M. D. Girardeau, J. Math. Phys. **1**, 516 (1960).

[54] M. Lewenstein, A. Sanpera, and V. Ahufinger, *Ultracold Atoms in Optical Lattices: Simulating quantum many-body systems*, Oxford University Press (2012).

[55] N. F. Mott, Proc. Phys. Soc. A **62**, 416 (1949).

[56] I. Danshita and A. Polkovnikov, Phys. Rev. A **84**, 063637 (2011).

[57] M. Greiner, O. Mandel, T. Esslinger, T. W. Hänsch, and I. Bloch, Nature **415**, 39 (2001).

[58] T. Stöferle, H. Moritz, C. Schori, M. Köhl, and T. Esslinger, Phys. Rev. Lett. **92**, 130403 (2004).

[59] C. D. Fertig, K. M. O'Hara, J. H. Huckans, S. L. Rolston, W. D. Phillips, and J. V. Porto, Phys. Rev. Lett. **94**, 120403 (2005).

[60] T. F. Gallagher, *Rydberg Atoms*, Cambridge University Press (1994).

[61] K. Góral, L. Santos, and M. Lewenstein, Phys. Rev. Lett. **88**, 170406 (2002).

[62] S. Yi, T. Li, and C. P. Sun, Phys. Rev. Lett. **98**, 260405 (2007).

[63] Y.-C. Chen and M.-F. Yang, J. Phys. Commun. **1**, 035009 (2017).

[64] J. Léonard, A. Morales, P. Zupancic, T. Esslinger, and T. Donner, Nature **543**, 87 (2017).

[65] J.-R. Li, J. Lee, W. Huang, S. Burchesky, B. Shteynas, F. Top, A. O. Jamison, and W. Ketterle, Nature **543**, 91 (2017).

[66] C. N. Yang and C. P. Yang, Phys. Rev. **150**, 321 (1966).

[67] A. Doikou, S. Evangelisti, G. Feverati, and N. Karaiskos, Int. J. Mod. Phys. A **25**, 3307 (2010).

[68] J. Hietarinta, J. Math. Phys. **25**, 1833 (1984).

[69] J. Goold, M. Krych, Z. Idziaszek, T. Fogarty, and T. Busch, New J. Phys. **12**, 093041 (2010).

[70] M. Ueda, *Fundamentals and New Frontiers of Bose-Einstein Condensation*, World Scientific Pub. Co Inc. (2010).

[71] M. D. Girardeau, E. M. Wright, and J. M. Triscari, Phys. Rev. A **63**, 033601 (2001).

[72] J. Goold and T. Busch, Phys. Rev. A **77**, 063601 (2008).

[73] V. I. Yukalov and M. D. Girardeau, Laser Phys. Lett. **2**, 375 (2005).

[74] A. Minguzzi and D. M. Gangardt, Phys. Rev. Lett. **94**, 240404 (2005).

[75] A. del Campo and J. G. Muga, Europhys. Lett. **74**, 965 (2006).

[76] R. Pezer and H. Buljan, Phys. Rev. Lett. **98**, 240403 (2007).

[77] M. Collura, S. Sotiriadis, and P. Calabrese, Phys. Rev. Lett. **110**, 245301 (2013).

[78] K. K. Das, M. D. Girardeau, and E. M. Wright, Phys. Rev. Lett. **89**, 170404 (2002).

[79] B. E. Granger and D. Blume, Phys. Rev. Lett. **92**, 133202 (2004).

[80] A. Micheli, A. J. Daley, D. Jaksch, and P. Zoller, Phys. Rev. Lett. **93**, 140408 (2004).

[81] A. Ruschhaupt and J. G. Muga, Phys. Rev. A **70**, 061604(R) (2004).

[82] J. J. Thorn, E. A. Schoene, T. Li, and D. A. Steck, Phys. Rev. Lett. **100**, 240407 (2008).

[83] G. N. Price, S. T. Bannerman, K. Viering, E. Narevicius, and M. G. Raizen, Phys. Rev. Lett. **100**, 093004 (2008).

[84] R. A. Pepino, J. Cooper, D. Z. Anderson, and M. J. Holland, Phys. Rev. Lett. **103**, 140405 (2009).

[85] A. Benseny, S. Fernández-Vidal, J. Bagudà, R. Corbalán, A. Picón, L. Roso, G. Birkl, and J. Mompart, Phys. Rev. A **82**, 013604 (2010).

[86] C. Ryu, P. W. Blackburn, A. A. Blinova, and M. G. Boshier, Phys. Rev. Lett. **111**, 205301 (2013).

[87] M. Born and V. Fock, Zeitschrift für Physik **51**, 165 (1928).

[88] J. E. Avron and A. Elgart, Comm. Math. Phys. **203**, 445 (1999).

[89] L. Eckert, M. Lewenstein, R. Corbalán, G. Birkl, W. Ertmer, and J. Mompart, Phys. Rev. A **70**, 023606 (2004).

[90] S. Deng, A. Chenu, P. Diao, F. Li, S. Yu, I. Coulamy, A. del Campo, and H. Wu, Phys. Rev. X **4**, eaar5909 (2018).

[91] S. Deffner, C. Jarzynski, and A. del Campo, Phys. Rev. X **4**, 021013 (2014).

[92] X. Chen, A. Ruschhaupt, S. Schmidt, A. del Campo, D. Guéry-Odelin, and J. G. Muga, Phys. Rev. Lett. **104**, 063002 (2010).

[93] A. Couvert, T. Kawalec, G. Reinaudi, and D. Guéry-Odelin, Europhys. Lett. **83**, 13001 (2008).

[94] S. McEndoo, S. Croke, J. Brophy, and T. Busch, Phys. Rev. A **81**, 043640 (2010).

[95] A. Benseny, I. Reshodko, and T. Busch, Few-Body Syst. **59**, 48 (2018).

[96] R. Menchon-Enrich, A. Benseny, V. Ahufinger, A. D. Greentree, T. Busch, and J. Mompart, Reports on Progress in Physics **79**, 074401 (2016).

[97] A. D. Greentree, J. H. Cole, A. R. Hamilton, and L. C. L. Hollenberg, Phys. Rev. B **70**, 235317 (2004).

[98] K. Eckert, J. Mompart, R. Corbalán, M. Lewenstein, and G. Birkl, Opt. Comm. **264**, 264 (2006).

[99] R. Menchon-Enrich, S. McEndoo, T. Busch, V. Ahufinger, and J. Mompart, Phys. Rev. A **89**, 053611 (2014).

[100] C. J. Bradly, M. Rab, A. D. Greentree, and A. M. Martin, Phys. Rev. A **85**, 053609 (2012).

[101] J. Schloss, A. Benseny, J. Gillet, J. Swain, and T. Busch, New J. Phys **18**, 035012 (2016).

[102] Y. Loiko, V. Ahufinger, R. Corbalán, G. Birkl, and J. Mompart, CLEO EUROPE/EQEC **1**, 1 (2011).

[103] I. Reshodko, A. Benseny, and T. Busch, Phys. Rev. A **96**, 023606 (2017).

[104] S. Longhi, G. Della Valle, M. Ornigotti, and P. Laporta, Phys. Rev. B **76**, 201101 (2007).

[105] T. Busch, B.-G. Englert, K. Rzażewski, and M. Wilkens, Found. Phys. **28**, 549 (1998).

[106] K. Winkler, G. Thalhammer, F. Lang, R. Grimm, J. Hecker Denschlag, A. J. Daley, A. Kantian, H. P. Büchler, and P. Zoller, Nature **441**, 853 (2006).

[107] H. Lee, P. Kok, and J. P. Dowling, J. Mod. Opt. **49**, 2325 (2002).

[108] A. N. Boto, P. Kok, D. S. Abrams, S. L. Braunstein, C. P. Williams, and J. P. Dowling, Phys. Rev. Lett. **85**, 2733 (2000).

[109] I. Stroescu, D. B. Hume, and M. K. Oberthaler, Phys. Rev. Lett. **117**, 243005 (2016).

[110] O. Zobay and B. M. Garraway, Phys. Rev. Lett **86**, 1195 (2001).

[111] T. Morgan, B. O'Sullivan, and T. Busch, Phys. Rev. A **83**, 053620 (2012).

[112] T. Schumm, S. Hofferberth, L. M. Andersson, S. Wildermuth, S. Groth, I. Bar-Joseph, J. Schmiedmayer, and P. Kruger, Nat. Phys. **1**, 57 (2005).

[113] P. W. Courteille, B. Deh, J. Fortágh, A. Günther, S. Kraft, C. Marzok, S. Slama, and C. Zimmermann, J. Phys. B: At. Mol. Opt. Phys. **39**, 1055 (2006).

[114] H. Perrin and B. M. Garraway, *Advances in Atomic, Molecular, and Optical Physics, Chapter 4*, Academic Press (2017).

[115] E. Tiesinga, B. J. Verhaar, and H. T. C. Stoof, Phys. Rev. A **47**, 4114 (1993).

[116] J. Stenger, S. Inouye, M. R. Andrews, H.-J. Miesner, D. M. Stamper-Kurn, and W. Ketterle, Phys. Rev. Lett. **82**, 2422 (1999).

[117] D. M. Bauer, M. Lettner, C. Vo, G. Rempe, and S. Dürr, Nat. Phys. **5**, 339 (2009).

[118] L. Amico, R. Fazio, A. Osterloh, and V. Vedral, Rev. Mod. Phys. **80**, 517 (2008).

[119] M. Nielsen and I. Chuang, *Quantum Computation and Quantum Information*, Cambridge University Press (2000).

[120] X.-C. Yao, T.-X. Wang, P. Xu, H. Lu, G.-S. Pan, X.-H. Bao, C.-Z. Peng, C.-Y. Lu, Y.-A. Chen, and J.-W. Pan, Nat. Photonics **6**, 225 (2012).

[121] T. Monz, P. Schindler, J. T. Barreiro, M. Chwalla, D. Nigg, W. A. Coish, M. Harlander, W. Hänsel, M. Hennrich, and R. Blatt, Phys. Rev. Lett. **106**, 130506 (2011).

[122] A. N. Wenz, G. Zürn, S. Murmann, I. Brouzos, T. Lompe, and S. Jochim, Science **342**, 457 (2013).

[123] S. Murmann, A. Bergschneider, V. M. Klinkhamer, G. Zürn, T. Lompe, and S. Jochim, Phys. Rev. Lett. **114**, 080402 (2015).

[124] R. Desbuquois, M. Messer, F. Görg, K. Sandholzer, G. Jotzu, and T. Esslinger, Phys. Rev. A **96**, 053602 (2017).

[125] B. B. Brandt, C. Yannouleas, and U. Landman, Phys. Rev. A **97**, 053601 (2018).

[126] R. Paškauskas and L. You, Phys. Rev. A **64**, 042310 (2001).

[127] J. Wang, C. K. Law, and M.-C. Chu, Phys. Rev. A **72**, 022346 (2005).

[128] B. Sun, D. L. Zhou, and L. You, Phys. Rev. A **73**, 012336 (2006).

[129] D. S. Murphy, J. F. McCann, J. Goold, and T. Busch, Phys. Rev. A **76**, 053616 (2007).

[130] T. Fogarty, T. Busch, J. Goold, and M. Paternostro, New J. Phys. **13**, 023016 (2011).

[131] Y. S. Li, B. Zeng, X. S. Liu, and G. L. Long, Phys. Rev. A **64**, 054302 (2001).

[132] C. H. Bennett, D. P. DiVincenzo, J. A. Smolin, and W. K. Wootters, Phys. Rev. A **54**, 3824 (1996).

[133] C. H. Bennett, G. Brassard, S. Popescu, B. Schumacher, J. A. Smolin, and W. K. Wootters, Phys. Rev. Lett. **76**, 722 (1996).

[134] G. Vidal and R. F. Werner, Phys. Rev. A **65**, 032314 (2002).

[135] T.-C. Wei, K. Nemoto, P. M. Goldbart, P. G. Kwiat, W. J. Munro, and F. Verstraete, Phys. Rev. A **67**, 022110 (2003).

[136] H. Bethe, Zeitschrift für Physik **72**, 205 (1931).

[137] E. H. Lieb and W. Liniger, Phys. Rev. **130**, 1605 (1963).

[138] B. Sutherland, Phys. Rev. Lett. **20**, 98 (1968).

[139] B. Sutherland, Phys. Rev. B **12**, 3795 (1975).

[140] M. Flicker and E. Lieb, Phys. Rev. **161**, 179 (1967).

[141] M. Gaudin, Phys. Rev. A **4**, 386 (1971).

[142] N. Oelkers, M. T. Batchelor, M. Bortz, and X. W. Guan, J. Phys. A **39**, 1073 (2006).

[143] M. T. Batchelor, X. W. Guan, N. Oelkers, and C. Lee, J. Phys. A **38**, 7787 (2005).

[144] N. J. Robinson, J.-S. Caux, and R. M. Konik, Phys. Rev. Lett. **116**, 145302 (2016).

[145] A. Klauser and J.-S. Caux, Phys. Rev. A **84**, 033604 (2011).

[146] M. Hallnäs and E. Langmann, J. Math. Phys. **46**, 052101 (2005).

[147] V. Caudrelier and N. Crampé, Rev. Math. Phys. **19**, 349 (2007).

[148] Y. Liu and Y. Zhang, Phys. Rev. A **91**, 053610 (2015).

[149] E. K. Sklyanin, J. Phys. A **21**, 2375 (1988).

[150] L. H. Ymai, A. P. Tonel, A. Foerster, and J. Links, J. Phys. A **50**, 264001 (2017).

[151] V. E. Korepin, N. M. Bogoliubov, and A. G. Izergin, *Quantum Inverse Scattering Method and Correlation Functions*, Cambridge University Press (1997).

[152] M. Jimbo, *Yang-Baxter Equation in Integrable Systems*, World Scientific (1990).

[153] M. Sroczyńska, T. Wasak, K. Jachymski, T. Calarco, and Z. Idziaszek, Phys. Rev. A **98**, 012708 (2018).

[154] K. von Klitzing, G. Dorda, and M. Pepper, Phys. Rev. Lett. **45**, 494 (1980).

[155] D. C. Tsui and A. C. Gossard, Appl. Phys. Lett. **38**, 550 (1981).

[156] M. A. Paalanen, D. C. Tsui, and A. C. Gossard, Phys. Rev. B **25**, 5566 (1982).

[157] B. I. Halperin, Phys. Rev. B **25**, 2185 (1982).

[158] T. Ando, Y. Matsumoto, and Y. Uemura, J. Phys. Soc. Jpn. **39**, 279 (1975).

[159] R. B. Laughlin, Phys. Rev. B **23**, 5632 (1981).

[160] D. J. Thouless, M. Kohmoto, M. P. Nightingale, and M. den Nijs, Phys. Rev. Lett. **49**, 405 (1982).

[161] M. Kohmoto, Ann. Phys. **160**, 343 (1985).

[162] Q. Niu, D. J. Thouless, and Y.-S. Wu, Phys. Rev. B **31**, 3372 (1985).

[163] D. C. Tsui, H. L. Stormer, and A. C. Gossard, Phys. Rev. Lett. **48**, 1559 (1982).

[164] R. Willett, J. P. Eisenstein, H. L. Störmer, D. C. Tsui, A. C. Gossard, and J. H. English, Phys. Rev. Lett. **59**, 1776 (1987).

[165] D. R. Hofstadter, Phys. Rev. B **14**, 2239 (1976).

[166] R. Resta, Rev. Mod. Phys. **66**, 899 (1994).

[167] D. Xiao, M.-C. Chang, and Q. Niu, Rev. Mod. Phys. **82**, 1959 (2010).

[168] Y. Hatsugai, Phys. Rev. Lett. **71**, 3697 (1993).

[169] C. De Lange and T. Janssen, Physica A **127**, 125 (1984).

[170] T. Fukui, Y. Hatsugai, and H. Suzuki, J. Phys. Soc. Jpn. **74**, 1674 (2005).

[171] A. Agarwala, Eur. Phys. J. B **90**, 15 (2017).

[172] J. G. Analytis, S. J. Blundell, and A. Ardavan, Amer. J. Phys **72**, 613 (2004).

[173] J. G. Analytis, S. J. Blundell, and A. Ardavan, Synthetic Metals **154**, 265 (2005).

[174] K. Czajka, A. Gorczyca, M. M. Maśka, and M. Mierzejewski, Phys. Rev. B **74**, 125116 (2006).

[175] S. Pradhan, J. Phys.: Condens. Matter **28**, 505502 (2016).

[176] I. Reshodko, A. Benseny, J. Romhànyi, and T. Busch, arXiv:1807.02949 accepted for publication in New J. Phys. (2018).

[177] J. J. Sakurai and J. Napolitano, *Modern Quantum Mechanics (2nd Edition)*, Pearson (2010).

[178] T. Jahnke and C. Lubich, BIT Numerical Math. **40**, 735 (2000).